Generation of intense few-cycle phase-stable electric fields: from the mid-IR to soft X-rays

Francisco José Maia da Silva

PhD Thesis
submitted to the Universitat Politècnica de Catalunya

Thesis Advisor: Prof. Dr. Jens Biegert
Thesis Co-Advisor: Prof. Dr. Helder Crespo

October 2015

Abstract

Devising new tools that expand our capabilities to sense and manipulate the world enables much of the scientific and technological progress around us. For example, light is increasingly more important as a tool for humanity. Not all light is equal, however - the light that we normally interact on a daily basis (e.g. the sun), despite its serene and directional appearance, exists in a state of ever changing disorder. What one would perceive as a smooth beam of white light is actually an ever changing pattern of colours. However, As the scale over which the colour changes is spatially too small and temporarily too rapid to be resolved by the human eye we perceive it as a smooth white beam. This lack of a clear spatio-temporal structure in naturally occurring light - coherence - limits what can be done with it.

If one were to overlap all the frequencies in a temporally coherent beam of light, one could generate an extremely short and powerful pulse. For example, by compressing in time all the colours in sunlight one would generate a light pulse with just a few femtoseconds duration. If such pulse would have a very modest energy (e.g., a Joule), it would have a peak power approaching the PetaWatt - several orders of magnitude more than the total energy production on earth at a given time. When focused on a minuscule spot, the electric field oscillations of this wave would have amplitudes greatly surpassing the electric fields that bind electrons to atoms, or even atoms together in molecules. This implies that by focusing these pulses into matter one can destroy chemical bonds, free the electrons from the influence of the atom's nucleus and even further accelerate these particles away from the interaction region. It follows that with the correct electric field shape, one could control and manipulate matter in new and interesting ways.

In this thesis we have dedicated ourselves to the creation and characterisation of intense, few-cycle pulsed sources of light, using several different approaches.

In this thesis a light source with more than 3 octaves (450-4500 nm) has been developed through filamentation of intense mid-IR pulses in solids. This source has high repetition rate (100 kHz), high spectral density and absolute carrier-envelope phase stability. Additionally, numerical simulations suggest that the nonlinear propagation dynamics induce self-compression, possibly leading to single-cycle pulses.

The scaling of strong field processes such as electron acceleration highly depends on the period or wavelength of the driving electrical field. This has implications for High harmonic generation (HHG) - the longer the wavelength of this field, the higher the energy of the generated photons. In this thesis we have built a high energy pulsed

parametric light source at 2 μm, a wavelength that enables one to generate soft-x-ray photons with energies exceeding 300 eV through phase-matched HHG - and further demonstrated HHG cutoff extension up to 190 eV in Argon, when compared to HHG from 800 nm pulses.

When doing HHG, in order to restrict the soft-X-ray emission to a single isolated attosecond pulse one needs to employ a gating technique. In this thesis we have extended the attosecond lighthouse technique up to the Water window (284-543 eV) which is of fundamental interest to study biological processes with unprecendent spatio-temporal resolution and elemental specificity.

The routine generation and characterisation of pulses in the single-cycle regime has historically been a challenge. As such sources invariably require extreme nonlinear spectral broadening, the optimisation and reproducibility of the output pulse has always been a limitation. In this thesis we extend the dispersion-scan technique to the single-cycle regime and demonstrate its use as a straightforward way to compress, characterise and phase-stabilise 3.2 fs pulses with >50 GW peak power. We illustrate the steps done to optimise this source to reach the single-cycle regime.

Resumen

Concebir nuevas herramientas que expandan nuestras capacidades para medir y manipular el mundo habilita gran parte del progreso científico y tecnológico que nos rodea. Por ejemplo, la luz es cada vez más importante como herramienta para la humanidad. Sin embargo, no toda la luz es igual - la luz con la cual normalmente interactuamos a diario (por ejemplo, la luz del sol), a pesar de su aspecto sereno y direccional, existe en un estado de constante cambio y disorden. Lo que se podría percibir como un rayo homogéneo de luz blanca es en realidad un patrón en constante cambio de color e forma. Sin embargo, como la escala de los cambios de color es espacialmente demasiado pequeña y temporalmente demasiado rápida para ser resuelta por el ojo humano lo percibimos como un rayo blanco homogéneo. Esta falta de una estructura espacio-temporal en la luz natural - coherencia - limita lo que se puede hacer con ella.

Si uno superpone todas las frecuencias en un rayo temporalmente coherente de luz, uno genera un pulso de luz extremadamente corto y potente. Por ejemplo, mediante la superposición en el tiempo de todos los colores en la luz del sol se generaría un pulso de luz con una duración de pocos femtosegundos. Si tal pulso tiene una energía muy modesta (por ejemplo, un Julio), tendría una potencia de pico alrededor del Petawatt - órdenes de magnitud mas grande que la producción total de energía en la Tierra en un determinado momento. Cuando enfocadas en un punto minúsculo, las oscilaciones del campo eléctrico de esta onda tendrán amplitudes superando los campos eléctricos que unen los electrones a los átomos, o incluso los átomos unos a los otros en moléculas. Esto implica que enfocando estos pulsos en la materia uno puede destruir enlaces químicos, liberar los electrones de la influencia del núcleo del átomo y acelerar estas partículas. En consecuencia, con la forma de campo eléctrico correcta, se podría controlar y manipular la materia en formas nuevas e interesantes.

En esta tesis nos hemos dedicado a la creación y caracterización de fuentes de pulsos de luz intensos de pocos ciclos, utilizando diversas técnicas.

En esta tesis una fuente de luz con más de 3 octavas (450-4500 nm) ha sido desarrollada a través de filamentación en sólidos de impulsos mid-IR intensos. Esta fuente tiene una alta tasa de repetición (100 kHz), alta densidad espectral y estabilidad de fase. Además, simulaciones numéricas sugieren que la dinámica de propagación no lineal induce auto-compresión temporal.

El escalamiento de los procesos de campo fuerte, como la aceleración de electrones, depende en gran medida de la longitud de onda del campo eléctrico interveniente. Esto

tiene grandes implicaciones para la generación de harmónicos altos (HHG) - más larga sea la longitud de onda del campo, mayor es la energía de los fotones generados. En esta tesis hemos construido una fuente de luz de alta energía a 2 μm, una longitud de onda que nos permite generar fotones con energías superiores a 300 eV a través de HHG con phase-matching - y además demostrado extensión de corte HHG hasta 190 eV en argón, en comparación con HHG a partir de pulsos a 800 nm.

Al hacer HHG, para limitar la emisión de rayos-X blandos a un solo pulso de attosegundos aislado, uno necesita emplear una técnica de gating. En esta tesis hemos extendido la técnica del faro de attosegundos hasta la ventana de la agua (284-543 eV) lo cual posee interés fundamental para estudiar procesos biológicos con resolución espacio-temporal y especificidad elemental.

La generación y caracterización de pulsos en el régimen de un solo ciclo ha sido históricamente un desafío. Como esas fuentes invariablemente requieren un ensanchamiento espectral no lineal extremo, la optimización del pulso siempre presenta un problema. En esta tesis hemos extendido la técnica de dispersion-scan, hasta el régimen de un solo ciclo optico y demostramos su uso como una forma de comprimir, caracterizar y estabilizar la fase de pulsos de 3.2 fs.

Contents

Chapter 1

Introduction

Light is crucial for humanity, having an essential role on our day-to-day lives - from allowing human sight, providing energy transfer from the Sun or permitting near-instant communication between all across the globe. Even so, there are many properties of light waves that are not naturally occurring in Nature that are of great use, especially for scientific and technical applications. Most of these are related to the ability to create spatially and/or temporally *coherent* waves, i.e. waves having a clear and fixed relationship between their phase at different points. This property manifests itself more notably in the ability to interfere waves between themselves in a repeatable fashion. For example, the production of intense bursts of light comprising of a just a few electric field oscillations is possible by temporal interference between an ensemble of light waves with wildly different periods. This way, a light wave with modest energy can have a tremendous peak power, by constructively interfering only during a brief amount of time, of the order of a couple of femtoseconds for visible light. Notably, these short durations are not only useful for probing natural processes at the scale of chemical, physical or atomic processes, but also to trigger them, allowing detection and control of matter at the shortest timescales. Additionally, the interferometric properties of a continuous train of fully coherent pulses forms a set of absolutely stable reference frequencies in the optical range (a *frequency comb*), which can be used to make measurements with unprecedented precision. All these properties are only present on a pulsed *absolutely coherent* source of light, i.e. a pulsed light source with not only spatio-temporal coherence in each pulse, but also spatio-temporal coherence between the different pulses.

One practical way to generate such pulses is through a laser. Since their invention in the 1960s lasers have allowed great advances in technology, albeit research in laser technology is still ongoing. The creation of new sources of absolutely coherent pulses of light in new regions of the optical spectrum, as well as with record duration, stability and spectral breadth is a very actual topic, given the applications of such sources.

Motivation

In this thesis we will focus on the generation and control of phase-stable intense few-cycle light pulses, i.e. repeatable electric fields with just a few high amplitude oscillations. These require a fully coherent broad-band source of light to generate such electric fields - usually a laser, or some form of laser-related technology.

The period of this electric field oscillation is decisive for many applications. For example the ponderomotive energy of an electron in a electric field varies widely with its oscillation period - for the same amplitude, the longer the field oscillation period the longer the time the electron is accelerated, loading to a higher ponderomotive energy. The generation of light in new regions of the electromagnetic spectrum with the right properties is then interesting, as it allows one to explore new physics and scaling laws. Additionally, one further obstacle to the routine application of such short electric field oscillations is their convenient metrology, as measuring events with femtosecond duration with high precision is not straightforward.

Outline of the thesis

Extending the bandwidth of such sources to cover a significant part of the electromagnetic spectrum while maintaining absolute coherence would simultaneously fulfill the requirement for many applications, such as the generation of sub-cycle pulses, synchronous seeding of amplifiers in different regions of the optical spectrum or time-resolved studies of natural processes at distant energy ranges. In **Chapter 2** we present an approach based on supercontinuum generation that results in a fully coherent source over more than 3 octaves - from 450 nm to 4.5 μm.

Certain applications of phase-stable intense few-cycle pulse benefit from high energy pulses with longer periods, i.e. at longer wavelengths, such as high harmonic generation. In **Chapter 3** we will discuss an approach to generate high intensity few-cycle phase stable pulses at 2 μm using broadband parametric amplification.

Sub-1.5-cycle phase-stable pulses in the NIR (800 nm) have been generated routinely for the last decade at a few selected laboratories using nonlinear optical methods. Despite this, taming such sources, as well as widespread reproduction of such results has proven hard, partially due to the expertise required in the diagnostic of such sources. In **Chapter 4** we develop a convenient technique for diagnostic of sub-1.5 cycle pulses which greatly reduces the complexity of the task, as well as commenting on the optimisation techniques required to reach the sub-1.5 cycle regime.

Isolated attosecond pulses in the soft-X-ray have numerous applications for the study of physical processes with extreme temporal resolution. Specifically the generation of attosecond pulses in the water window (284-543 eV) is of interest to study biological processes. Several techniques have been demonstrated in order to generate isolated attosecond pulses at different photon energies. In **Chapter 5** we extend the attosecond lighthouse technique to higher energies, in order to generate isolated attosecond pulses in the water window (300 eV).

1.1 Phase-stable intense few-cycle pulses

The potential applications of the pulses discussed in this thesis are based on the confluence of four important properties: their absolute electric field stability, short duration, high intensity and broad spectral bandwidth. Each of this properties has its own implications which allow different applications, whereas the combination of all of them offers unique opportunities.

Intensity

A sub-10 femtosecond pulse with the modest energy of a few mJ has a peak power of the level of hundreds of gigawatts. This means that during a brief instant, one is able to transfer energy with enormous power to e.g. an experimental target. By focusing such pulses down to a 0.2 mm beam, the peak intensity of the result electric field approaches 10^{14} W/cm^2, which is comparable to the Coloumb field of the atom experienced by valence electrons, i.e. the electric field is now able to compete with atomic binding and produce free electrons, or rapidly destroy chemical bonds. This has interesting implications, as a great deal about nature can be understood just by perturbing matter with an intense laser and studying what comes out [1, 2].

If this pulse is instead focused to a beam size comparable to the wavelength (1 μm) then the peak intensity is in excess of 10^{18} W/cm^2, in the so called *relativistic* regime, where the ponderomotive energy of the electron in the laser field is comparable to its rest energy mc^2. In this regime a new class of interesting experiments is possible, such as particle acceleration in a table-top setup to the GeV level [3] or efficient single-attosecond pulse generation in the XUV [4].

This ability to control matter with strong fields gives rise to many applications of intense ultrashort pulses. Such are high harmonic generation of XUV and soft-X-rays [5], micro-machining [6], electron acceleration [7], 3D nano fabrication [8], amongst others. Even preliminary studies in cancer treatment have been done [9] using such pulses.

Short duration

In order to study chemical, electronic or atomic processes happening at the femtosecond or even sub-fs time scales one needs a temporal reference with a shorter duration. Ultrashort pulses with durations down to the femtosecond in the optical range [10] or tens of attoseconds in the XUV range [11] are suitable to serve as such references, allowing extreme temporal resolution. These pulses are the shortest flashes of energy ever produced, and open new possibilities for metrology, specifically for the study of time-dependent phenomena.

Such possibilities are the observation of chemical reactions [12], tracking carrier dynamics in semiconductors [13], observing energy transfer in a large molecule [14], and the real-time observation of Auger effects in atoms [15], as well as quantifying the delay between the ionisation of different atomic levels [16]. Interestingly, extending these short pulse durations to the hard-X-rays is expected to allow direct diffractive imaging of or-

bital states of atoms or molecules, i.e. mapping the electron distribution of the atom with temporal and spatial resolution [17].

Absolute stability

A train of pulses with constant repetition rate and phase of the carrier in relation to the intensity envelope (Carrier-to-Envelope Phase - CEP) can only be generated by the coherent sum of a number of sinusoidal waves with different frequencies and absolute stability, i.e. a frequency comb. Such train of pulses is extremely interesting for interferometry experiments - in a sense, it has a very limited coherence length, as the signal only exists for a few femtoseconds. But since every pulse is the same, then one could interfere one pulse with the next, or the one after, or a pulse generated several hours after, ideally, resulting in a very large *potential* coherence length. An interesting thought experiment is to bounce an ultrashort pulse off the retroretlecting mirrors positioned in the surface of the moon [18] and interfere it with another one, generated 2 seconds later on earth - which would allow us to track the moon's position in time with precision comparable to the wavelength, e.g. 1 μm (in practice, the stability of the laser source might not allow such experiment). Spatial interferometry experiments with outstanding precision are routinely done based on this technique [19, 20].

A frequency comb can also be used to measure signals at optical frequencies. By overlapping this signal with a line of the comb a beat note can be produced in a photodetector - if the frequency difference between the signal and comb line is slow enough for the detector, then it can be measured. Hence, frequency combs provide a link from the optical region of the electromagnetic spectrum to the radio-frequency region, where electrical signal and processing is more practical, allowing the measurement of signals with frequencies in the 100s of THz range. One useful application of this is in the field of optical clocks. By measuring an atomic transition frequency in the optical domain with a frequency comb line at the appropriate wavelength, one can achieve better performance than the best atomic cesium clocks, anticipated to be able to reach 1 part in 10^{18}. Such precision in time keeping allows interesting experiments, such as fundamental physics tests. As an example, researchers in Colorado were able to measure a statistically significant difference in the counting rate of an optical clock by raising the optical table the clock was built in by 30 cm, which was explainable by the relativistic effect of the earth gravitational field on time [21].

The frequency comb structure of a train of ultrashort pulses provides allows some of the most precise experiments on earth. In a sense, they are some of the most precise measurement devices currently available.

Broad bandwidth

Despite being directly related to the short duration property of ultrashort pulses, it is worth discussing bandwidth by itself. Ultrashort pulses on different spectral ranges allow exploiting different processes. For example, with incoherent light one can identify molecular fingerprints through absorption spectroscopy. Using the comb nature

of these trains of pulses one can do what is called dual comb spectroscopy: by doing asynchronous sampling between two stabilised frequency combs one can acquire an absorption spectrum over a large bandwidth in just a few microseconds, with extreme spectral resolution [22].This allows high-frequency monitoring of molecular specimens in a sample with extremely high resolution and sensitivity, combining the resolution of typical fourier transform spectroscopy (FTIR) with the speed of CCD-based dispersive polychromators.

Another possibility brought forward by intense, ultrashort pulses with large bandwidths is the production of arbitrary electric field waveforms in the optical domain. For example, with a sub-cycle pulse it is possible to precisely control valence-electron wave packet dynamics [23], or for certain applications the production of a less 'sinusoidal' pulse shape can be of use, e.g. in [24] it has been found that by engineering the wave function to resemble a ramp, the cutoff of high harmonic generation can be extended without penalty in yield. The availability of pulses with several octaves of spectrum will open new possibilities for coherent control, as one can now taylor the electric waveform with freedom.

Chapter 2

Multi-octave phase coherent intense supercontinuum generation from the visible to the mid-IR

As discussed in the introduction, broadband coherent sources have a host of applications, ranging from advanced sensing to micro-fabrication or possibly even cancer treatment [9]. In this chapter we develop and study a coherent source with extreme bandwidth - spanning from the visible/blue all the way to the mid-IR up to the lower CO2 absorption lines. Not only this source is inherently stable in spectral intensity, it is also stable in absolute phase, i.e the electric field emitted is constant from shot to shot. The octave-exceeding bandwidth of the spectrum allow simultaneous and convenient access to many wavelength ranges of interest from the same laser, and the absolute phase stability enable the production of electric field waveforms able to steer and control matter in new and interesting ways. The relevant parameters for such a source are a smooth, stable spectral profile, an extremely stable, compressible spectral phase and the lack of spatio-spectral features in focus. One nonlinear process capable of generating such parameters is supercontinuum generation. In this chapter we will start by reviewing some basic processes leading to supercontinuum generation, as well as discuss important processes that affect the performance of the source. Afterwards, we will present our experimental and numerical work and discuss this work's limitations. We will finalise by discussing future steps and new possibilities that would take advantage of this source.

2.1 Supercontinuum generation

The generation of broad, feature-less broadband spectra from a narrowband laser source has been named 'supercontinuum generation'. Alfano et al observed in 1970 [25, 26, 27] that MW-level pulses from a Nd:Glass laser would generate white-light when focused

on an optical crystal. Due to their high intensity, such pulses excite nonlinear effects during propagation that lead to the generation of new frequencies of light. In the cited case, a 300 nm continuous spectrum was observed after propagation of a 5 mJ 4 ps/532 nm pulse through a 10 mm BK7 plate, hence the name *supercontinuum* (SC). Today, a myriad of ways have been developed to generate a continuous spectrum worthy of this name, most of them based on nonlinear optical effects. To the author's knowledge, no agreement exists on how broad a spectra must be in order to be called a supercontinuum. Surprisingly, there are no requirements regarding shot-to-shot coherence when talking about a supercontinuum - indeed all that needs to be fulfilled is the generation of a large spectral bandwidth, and that coherent light is used to start the process - hence the source is still expected to be spatially coherent to some extent. Hence some SC sources are shot-to-shot reproducible, whereas others are not (e.g. sources where modulational instabilities or chaotic effects have a strong role). Some of the techniques used to generate supercontinua are:

- Kerr-lens mode locking [28] is routinely used to generate nJ-level femtosecond pulses spanning an octave of spectrum around 800 nm (hence 600 nm of bandwidth) [29]. These sources are based on amplification through stimulated emission (which is limited in bandwidth by the breadth of the excited transition) coupled with nonlinear processes in the gain medium. Since there are strong nonlinear effects involved, the generated spectrum can exceed the gain bandwidth of the medium, leading to a broader continuum. Examples of continua generated using this method include (a) over 600 nm of bandwidth around 800 nm are routinely generated in Ti:Sa oscillators [29] (b) 350 nm around 1.3 μm using Cr:Forsterite [30] and (c) 400 nm around 2.4 μm using Cr:ZnS [31].

- Optical parametric oscillation [32], where a cavity containing a medium with a high χ_2 is pumped at the right repetition rate, leading to high gain over a possibly broad bandwidth, only limited by the available birrefringent crystals and their dispersive properties (but also the available pump sources). E.g. in [33] a spectrum from 2.6 to 6.1 μm directly out of an synchronously pumped OPO was generated.

- High-harmonic generation [34]: when exciting matter using an ultrashort pulse at intensities above 10^{13} W/cm^2 the formation of free electrons, coupled with the acceleration of these electrons and further recombination when they recollide with the parent ion leads to the emission of photons in a very broad bandwidth of frequencies. If such emission can be restricted to a single event then the generated spectrum is continuous (e.g. see chapter 5), and can span several octaves [35], usually in the XUV/soft-X-ray region of the spectrum.

- Intrapulse DFG: DFG of even a relatively narrowband pulse can potentially generate a broad spectrum, as it conserves the spectral bandwidth (in the frequency domain) but can greatly increase the central wavelength. E.g. in [36] a spectrum from 1000 to 2400 nm was generated through efficient intrapulse DFG of a 800 nm pulse.

- Single-pass nonlinear propagation: through high intensity nonlinear propagation several effects can work together to significantly broaden the spectrum of the incident laser pulse and generate a continuous spectrum spanning even several octaves. In the following subsections we will discuss the effects leading to this broadening.

2.1.1 Nonlinear effects leading to SC generation

In most noncentrossymetric media, $\chi^{(3)}$ effects are prevalent during high intensity propagation. Specifically, self-phase modulation (SPM) is often the most noticeable effect, as no phase-matching conditions need to be satisfied. The change in refractive index through the Kerr-effect leads to an apparent time-dependent refractive index, which will modulate the phase of the propagating pulse - leading to generation of new frequencies on the leading and trailing edges of the incoming pulse. This leads to progressive spectral broadening[1] during high intensity propagation, which can, in the right conditions, result in a significant increase of the spectral content of the propagating pulse. However, in the short pulse duration regime, due to this time-dependent refractive index the difference in group velocity of the peak of the pulse compared to the edges becomes significant, and self-steepening effects [37][38] become important. This usually leads to a much stronger broadening on the blue than the red side of the spectrum. In extreme cases this effect can lead to pulse breakup, which can lead to the generation of light with a broad range of frequencies in a higher energy range, although with a more featured phase. The spatial dimension must also be taken into account - the induced phase modulation depends on intensity - hence the Kerr effect curves the phase front according to the beam profile and induces a self-focusing effect in a free propagating beam (for positive n_2, which is a common situation in the NIR). This will lead to a gradual intensity increase - which will in turn exacerbate the other nonlinear effects. So far these effects can result in significant spectral broadening without loss of coherence. When one considers a spatiotemporal propagation model including $\chi^{(3)}$, as well as linear spatial diffraction one can find that the self-focusing and diffractive effects can enter an equilibrium and a spatial soliton is formed. This phenomena was first observed in 1964 by Chiao et al and was named self-trapping [39].

When considering broadband pulses propagating in media over long distances chromatic dispersion effects start to be determinant, i.e. the difference in group velocity of different parts of the spectrum eventually results in temporal broadening and the loss of intensity, eventually diminishing any nonlinear effects. Similarly to the spatial case from last paragraph, there can be a situation where the dispersion and the temporal Kerr effect balance each other: if the blue region of the spectrum has a tendency to lag behind the red region (normal dispersion) and self-phase modulation generates blue frequencies in the leading edge of the pulse (negative n_2), the two effects will compensate each other and form a temporal soliton. This effect was first observed during nonlinear propaga-

[1] The spectrum broadens only if the input pulse is chirped with the same sign as the n_2 of the media, which is the case for the common situation of a positively chirped pulse in the NIR propagating through glass, which has a positive n_2. If these quantities have opposite signs then the spectrum narrows, which is mostly undesirable.

tion in liquid media [40]. It can also happen with the opposite medium parameters: anomalous dispersion and positive n_2.

As the intensity of the pulse is increased, either due to self-focusing or due to a tight-focusing geometry, the ionisation rate can become significant and free electrons will be produced. The presence of free electrons effectively decreases the refractive index of the medium, which will affect the center of the beam more, hence creating a defocusing effect, know in the literature as plasma defocusing [41]. During free-space propagation, this effect, counterbalanced with Kerr self-focusing, allows self-confined high intensity propagation over a long distance[2] in different conditions other than the diffraction-balanced self-trapping [39], specifically in higher energy pulses. This regime, where plasma defocusing balances Kerr self-focusing can be named *filamentation*, although other authors prefer the term *light bullet* - see section 1.1 of [44] for a discussion.

For an extense review on the topic of filamentation, see [44]. A more thorough and pedagogical description of these nonlinear effects can be found in [38].

2.1.2 Guiding during high intensity propagation

In order to get efficient spectral broadening, one can exploit strong nonlinear effects that result in spectral broadening, typically of $\chi^{(3)}$ nature. A measure of the impact of χ_3 effects can be estimated by the nonlinear phase shift, defined by:

$$\phi_{NL}(L) = \frac{2\pi}{\lambda} \int_0^L n_2 I(z) dz \tag{2.1}$$

Which is nothing more than the phase shift imposed during propagation of a pulse of intensity I(z) through a medium of nonlinear refractive index n_2 and length L. This quantity, despite modelling nonlinear propagation ignoring many important effects, serves as good upper bound of the estimation of the χ_3 effects. In figure 2.1 is represented a pulse undergoing progressive self-phase modulation in an n_2 medium, and the relation between the induced temporal phase, nonlinear phase shift and consequent spectral broadening.

One can then derive a rule of thumb that nonlinear effects become more pronounced with increasing intensity and propagation length. Hence, spectral broadening and the nonlinear effects leading to supercontinuum generation are favoured when using a confined propagation geometry, which leads to intense propagation over long distance, when compared to e.g. a free-focusing geometry, where the high intensity propagation distance is limited by the Rayleigh length. Several confinement methods, such as optical fibres, hollow fibres or filamentation are routinely used to allow the long-range high intensity propagation that leads to supercontinuum generation.

Optical fibers allow propagation of high intensity pulses but the damage threshold of the fiber core medium presents an upper bound to the amount of energy that can be coupled. Typically, nonlinear effects are already significant when coupling nJ energy pulses with fs duration (e.g. [45]). Further scaling of input intensity would reach the

[2]Filaments exhibiting plasma columns up to several tens or even hundreds of meters have been generated and studied e.g. [42] or [43]

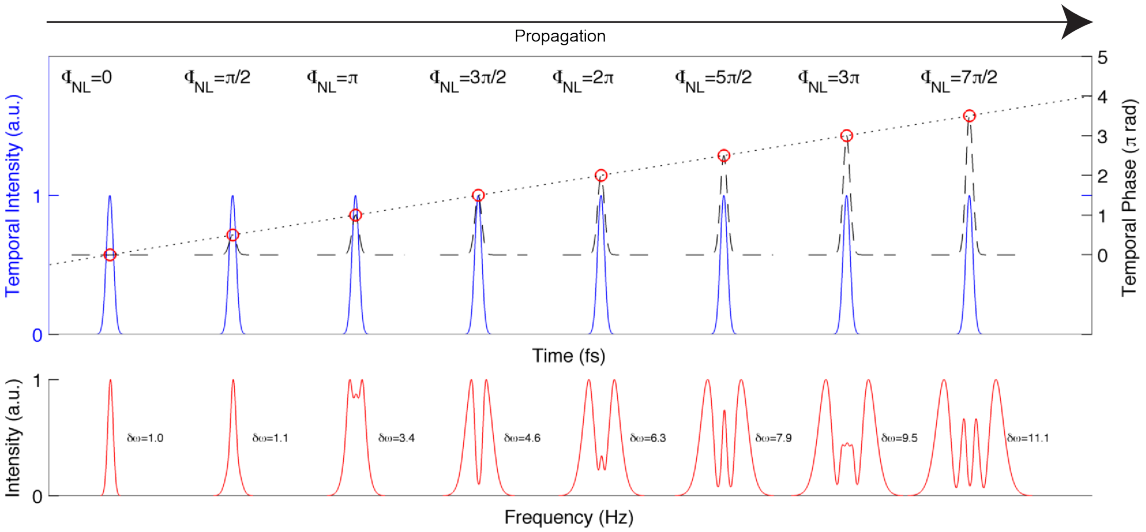

Figure 2.1: Illustration of the relation between self-phase modulation, nonlinear phase shift and spectral broadening for a pulse propagating through a χ_3 medium without dispersion or additional nonlinear effects other than SPM. Top, left to right: Evolution of the temporal intensity and phase of a gaussian pulse undergoing progressive self-phase modulation. The nonlinear phase shift at each propagation distance is equal to the maximum induced phase shift, corresponding to the peak of the pulse. Bottom: corresponding spectrum at each propagation distance.

optical damage threshold. Using hollow guiding geometries such as hollow-core fibers (HCF) greatly increases the damage threshold, albeit at the expense of a lower core nonlinearity. Typically mJ/sub-mJ pulses are coupled into meter long HCF [46], producing octave-spanning continua, with a remarkably high energy density- e.g. in [47] a 400nm continuum around 800 nm containing 6 mJ at 1 kHz was generated. It has been found that it is possible to control the spectral dispersion of the guiding geometry by shaping its cross-section [48, 49]. This way temporal dispersion can be controlled, effectively tailoring the nonlinear interaction. E.g. one can choose a geometry leading to a zero dispersion point at the centre wavelength of our pulse, leading to the possibility of soliton-like propagation. Alternatively it is also possible to taylor the geometry such that the dispersion is anomalous or normal, resulting in supercontinua with different characteristics, appropriate for different applications. This approach however has one limitation regarding power scaling, due to the fact that the larger the guiding geometry the lower the phase introduced during propagation, hence typically these photonics crystal fibers have small cores, hence the energy that can be coupled is limited. Regardless, it is possible to couple a few nJ in solid core PCFs and generate octave-spanning continua, first demonstrated in [50, 51], which is now a common setup for self-referenced frequency-comb generation [52]. With certain hollow core photonic crystal fiber designs it is possible to scale the energy up to tens or even hundreds of microjoules [53] while maintaining octave spanning spectral breadth.

One important feature of geometrical guiding geometries is that the output beam quality, position and propagation direction is imposed by the waveguide. This can be beneficial as it can lead to a high spatial quality of the beam, as well as a constant beam size and direction, which can be determinant for certain applications.

Another phenomena that leads to spatial confinement is filamentation, which is based on an equilibrium between nonlinear effects, leading to a confined beam over a distance typically several times the Rayleigh length. Contrary to the geometrically guided geometries, due to its dynamic spatiotemporal nature filamentation does not always result in a constant waist propagation, more often resulting in focusing-defocusing cycles or just one extended focusing-collapse-defocusing event [44]. Scaling of filamentation to different energies and pulse durations is possible by choosing the host material, which will, amongst other things, change the linear dispersion, ionisation rate and nonlinear refractive index, which are in first approximation the determinant quantities. Filamentation down to the tens of nJ regime has been demonstrated in solids with high n_2 [54], while hundreds of mJ have been confined in filaments in air [55].

Given that there is the possibility to achieve a broad spectrum starting with a narrower one, one can wonder how narrow can the starting spectrum be to reach a certain breadth? It would be of interest to start with a long pulse (>ps) and broaden it to a coherent spectrum capable of supporting a few-cycle pulse. This is, however, technically challenging as such an extreme amount of broadening results in a chaotic situation - for a small change in the input pulse there will be a significant change in the spectrum and phase of the output pulse. For a study of this effect please refer to [56]. We conclude then that to achieve shot-to-shot repeatable and fully coherent SC it can be advanta-

geous that the input pulse has a short duration already, to minimize the amount of nonlinear effects and hence possible chaotic behaviour.

2.1.3 Normal and anomalous dispersion regimes

The choice of different host materials, different driving laser wavelengths or waveguide geometries allows one to change the dispersion regime that our pulse is propagating through. Effectively, by balancing the linear dispersion with the phase introduced by nonlinear effects, the distance over which the pulse can undergo high intensity propagation can be extended, especially for broadband driving pulses which suffer more from chromatic dispersion effects [44]. Another useful phenomena that can occur is chromatic self-compression of the driving pulse, as the newly generated frequencies are conveniently delayed into the main peak of the pulse , as represented in figure 2.2.

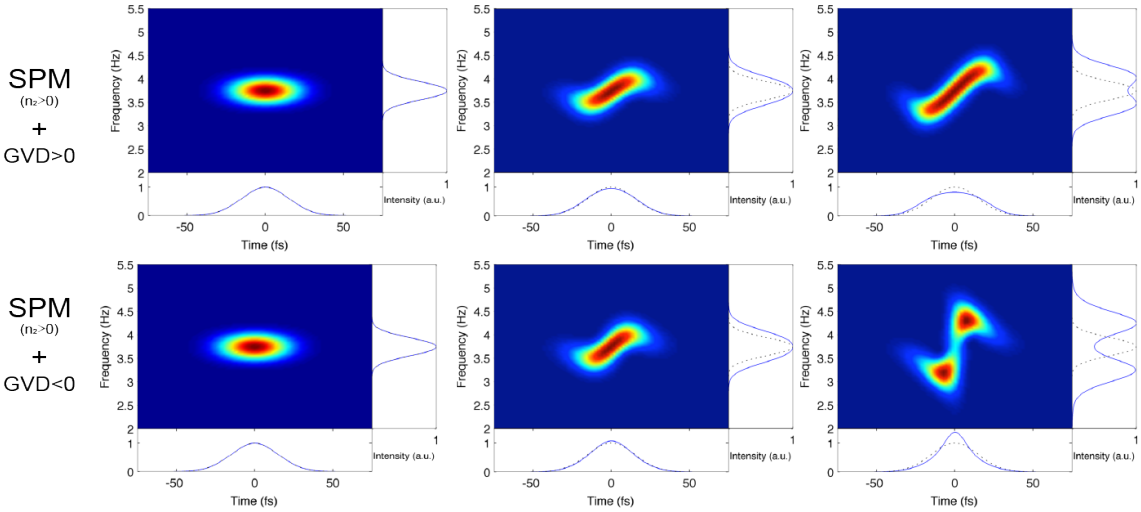

Figure 2.2: Illustration of the interplay between dispersion and SPM, possibly leading to self-compression behaviour. A transform-limited gaussian pulse propagates through a medium with GVD and SPM - its spectrogram is represented at three steps along the propagation through the medium. Top row: For the situation where $n_2 > 0$ and the GVD/mm of the medium is positive both processes are contributing to the increase of blue/red frequencies in the back/front of the pulse, leading the a progressive pulse broadening and decrease in peak intensity. Bottom row: For the situation where $n_2 > 0$ and the GVD/mm of the medium is negative, while SPM generates blue/red frequencies in the back/front of the pulse, the anomalous dispersion is acting to bring them to the peak of the pulse, leading to a progressive pulse self-compression and increase in peak intensity.

2.1.4 Phase-matching and conical waves

Coherent light generation is always subject to phase-matching considerations - despite the fact that many frequencies can be generated by the various nonlinear effects, only the ones that are phase matched, i.e. experience a coherent build-up of radiation, will contribute significantly to the final pulse. When the generated spectra span a broad range of frequencies phase-matching effects become determinant as different spectral ranges can possess wildly different group velocities, making phase-matching more selective. When two regions of the spectrum have similar group velocities (e.g. if the zero dispersion wavelength of the medium is in between them) then phase matching between them is possible and a so called blue-shifted peak can be formed [57]. This allows more efficient energy transfer between distant regions of the spectrum especially when the broadened spectrum crosses the zero dispersion wavelength of the medium. Another phenomena deriving from this is the possibility of the formation of conical waves - by adding a small amount of transverse momentum in wavelengths which were phase-mismatched with the main peak coherent buildup of a conical wave is possible. This phenomena is behind the observation of X-waves, O-waves and fish-waves [58, 59]. One can also wonder what are the limits to the breadth of the spectrum generated by filamentation - it turns out it can be predicted quite accurately given the dispersion of the medium, following the qualitative theory described in [60]. Broadening on the long-wavelength side usually results in a exponentially decaying spectral intensity, while on the short-wavelength region a plateau is formed down to the lowest wavelength which can still travel at the same group velocity as the pump, usually aided by the formation of a conical X-wave, which extends the phase-matching into even lower wavelengths.

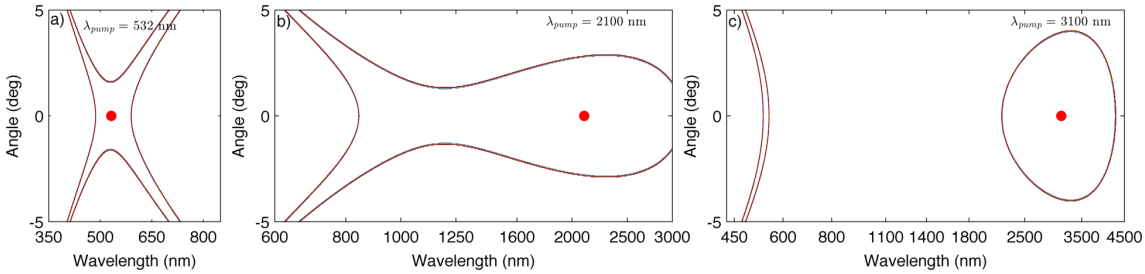

Figure 2.3: Prediction of the extension of supercontinua based on the scattering model in [60] in YAG. Red dots indicate the pump wavelength, whereas the contours are the phase matching boundaries that satisfy equation (4) of [60] with τ_{scl} = 700 fs. a) A pump laser in the normal dispersion regime (532 nm) results in the formation of an X-wave. b) A pump laser near the zero dispersion point of YAG (1600 nm) results in the formation of a fish-wave. c) A pump laser in the anomalous dispersion regime (3100 nm) results in the formation of an O-wave, as well as a dispersive tail below the zero dispersion point, where the group velocity is similar to the one of the pump.

2.1.5 Spatial effects during filamentation

The peak power for which the self-focusing of a laser pulse beats its intrinsic diffraction, also called the critical power, is given by [39]:

$$P_{SF} = \frac{3.77\lambda_0^2}{8\pi \cdot n_0 \cdot n_2} \tag{2.2}$$

Above this power, the effect of self-focusing overcomes diffraction and the intensity will then gradually increase until different nonlinear effects become dominant to determine the spatio-temporal propagation of the laser pulse. For example in the conditions leading to filamentation, free electron formation due to an intense electric field will lead to a defocusing effect which can balance self-focusing, as discussed in section 2.1.1.

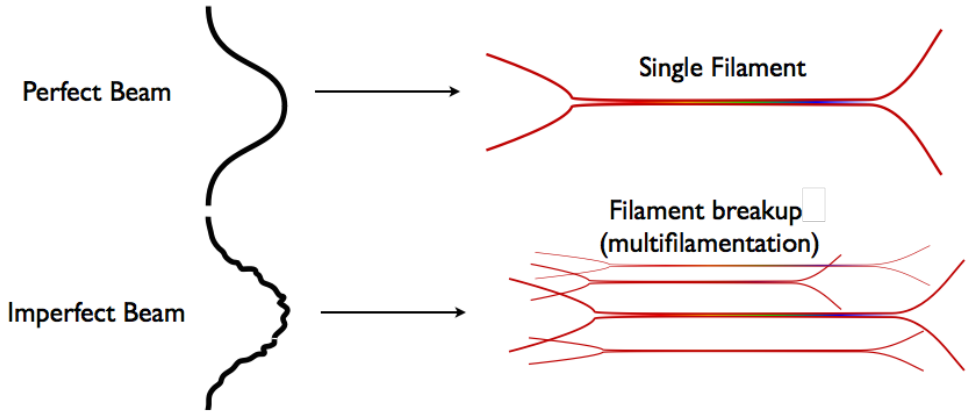

Figure 2.4: Illustration of the principle behind multi-filamentation. For peak powers much higher than the critical power a single filament would be sustainable for a perfectly smooth and convex input beam profile. For realistic experimental beam profiles with imperfections either caused by the generating laser or inevitable particles or features in the optics, the features of the beam will be able to self-focus on themselves, rather than the whole beam, as the power contained in each feature approaches the critical power. In this situation the beam breaks up in multiple filaments, each of them typically with an energy corresponding to a critical power. For a more grounded explanation of this phenomenon, see chapter 7.1.3 of [61]

This relation requires that for a certain medium (i.e. a specific n_0 and n_2) and pulse duration there is a minimum energy required to form a filament, below which the diffraction of the laser pulse is much stronger than the self-focusing, not allowing intense propagation for more than a Rayleigh length. Regarding the maximum energy that can be coupled into a filament, the limit seems to be of practical nature. If the input laser pulse has a perfectly clean (e.g. gaussian) spatial profile then in principle the energy of the pulse can be increased past the critical power, changing the strength and dynamics of the nonlinear propagation of the pulse but leading to the formation of a coherent

single filament. In practice, small imperfections in the beam profiles of the lasers used lead to multifilamentation as one scales up the input energy, as the different features and imperfections of the beam have a tendency of self-focusing on themselves rather than in the full beam (Fig 2.4). This leads to a typical energy limitation of the order of a small multiple of the energy corresponding to one peak power (typically of the order of millijoules in gases and microjoules in solids - see section 4.1.1 of [44] for a discussion on this).

If, however, increasing the energy in a single filament to possibly achieve higher spectral densities is desired, then by analysing equation 2.2 one concludes that either a different medium needs to be used (to have a lower $n_0 \times n_2$ coefficient) or a longer wavelength laser should be used. A lower $n_0 \times n_2$ generally means less nonlinear effects, hence a need for longer propagation distances to achieve the same nonlinear phase shift.

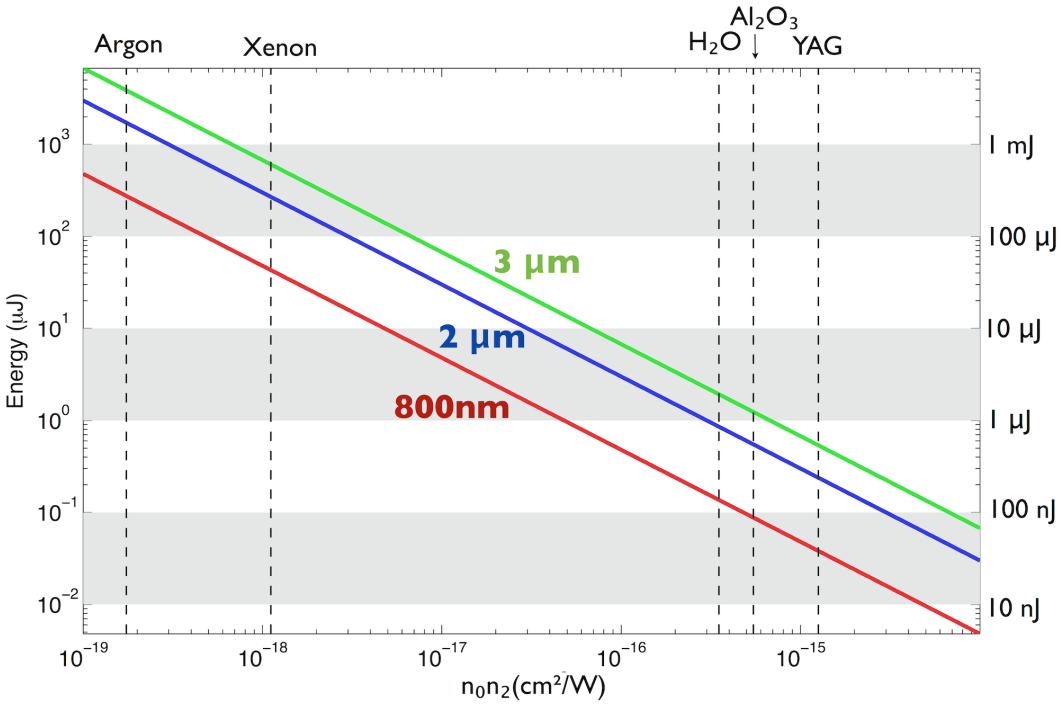

Figure 2.5: Scaling of the energy corresponding to one critical power for a gaussian 50 fs pulse in different materials, for three different wavelengths. Longer wavelengths require more energy to form a filament and consequently allow higher energy filaments with less tendency for multifilamentation.

In order to illustrate these scaling laws, In figure 2.5 is represented a plot of the energy of a 50 fs gaussian pulse whose peak power is the critical power from equation 2.2, in function of $n_0 \times n_2$, for three different wavelengths. Different materials typically used to generate SC of interest are represented. One can see that an increase of 3.75 times in wavelength (from 800 nm to 3 μm) requires an increase of 14 times in energy to

achieve the critical peak power. This can be seen as a limitation, as a laser with higher pulse energy is needed to induce filamentation, but can be of interest since it allows a filament with higher energy content without further scaling to gases.

2.1.6 Self-compression effects

The highly nonlinear nature of filamentary propagation leads to a complex competition between nonlinear effects that will inevitably reshape the temporal profile of the pulse. For the right conditions, these effects can lead to a significant self-compression of the input pulse, even down to the single-cycle domain [62].

A simplistic model to explain this phenomenon is represented in figure 2.6. The instantaneous Kerr effect leads to significant self-focusing of the intense part of the pulse. Due to the high intensities reached, each half-cycle of the pulse induces significant ionisation on the medium, which will have an opposite effect on the refractive index as self focusing, leading to defocusing. Since the ionisation fraction of the medium is much higher after the peak of the pulse, the defocusing effects will be more severe on the trailing edge of the pulse, and will beat the self-focusing effect. Hence the two effects will act as time-dependent lenses, leading to more self-focusing of the leading edge of the pulse and more defocusing on the trailing edge (for $n_2>0$). One can then imagine that the self-focused part/leading edge will continue to propagate with high intensity until it reaches an equilibrium with the defocusing effect, while the trailing edge will be defocused, hence not contribute as much to the pulse on axis. This can explain the reduction of pulse duration of the pulse on axis, i.e. self-compression.

Note that a self-compression mechanism is not necessary to be able to achieve a shorter pulse than the input after nonlinear propagation, e.g. a coherent nonlinear broadening mechanism coupled with appropriate dispersion compensation would always produce a shorter pulse. However, self-compression is attractive as it can in principle provide the possibility of delivering a short pulse directly to an experiment with a simple setup and without any recompression optics.

2.1.7 CEP effects

Nonlinear propagation tends to couple different spatio-temporal properties of the pulse. As such intensity fluctuations of the input pulse can cause fluctuations in not only the intensity of the output pulse, but also the phase. In first approximation one can think of the intensity dependence of the nonlinear phase shift, i.e., if the source has 1% shot-to-shot stability then the final absolute phase will vary by 1% shot-to-shot as well. In reality it is unpractical to estimate the nonlinear phase shift that occurs inside a filament, as very different nonlinear effects all contribute to the propagation. A measurement of the output phase of a filament in sapphire pumped in the femtosecond regime at 800 nm in function of the input energy [63] has revealed the dependency in this particular setup to be around 140 mrad of phase shift per each % of variation. This means that generating

[4]Free-electron population in arbitrary units modelled in this figure with $\rho(t) = \int_0^t |E(t')|^4 dt'$ for simplicity.

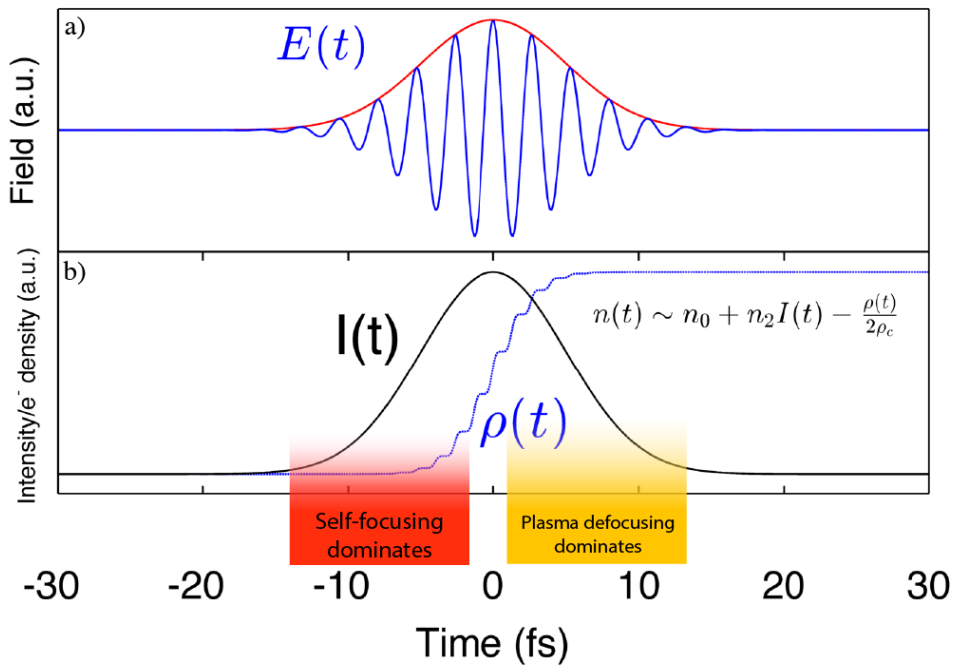

Figure 2.6: Illustration of a simple model of a spatio-temporal self-compression mechanism. The gradual formation of free-electrons across the pulse temporal structure, coupled with the Kerr effect, induces rapidly changing focusing/defocusing conditions. (a) Electric field of the considered pulse. (b) Intensity (black line) and simplistically modelled[4]free electron density (blue). For a medium with positive n_2, the Kerr effect will favor self-focusing in the leading edge of the pulse, while the formation of free-electrons will favour defocusing in the trailing edge of the pulse. This effect can not only lead to a spatial balance favouring constant waist propagation, but also a self-compression effect where the trailing edge of the pulse is attenuated by defocusing.

a supercontinuum with an unstable source will diminish shot-to-shot phase coherence, and must be taken into account when choosing where to apply the supercontinuum.

2.2 Experimental Results

In this work supercontinuum sources based on filamentation of femtosecond SWIR (2.1μm) and MIR (3.1μm) pulses in bulk material were investigated. Multi-octave spectral breadth was attained, specifically 450-2.5μm and 450-4.5μm for the two different pump pulses (2.1μm and 3.1μm, respectively). Carrier-envelope phase stability and shot-to-shot repeatability was verified. The far-field spectral distributions (λ, ω) were measured and the present conical waves identified.

2.2.1 Laser systems

Supercontinuum generation is an all-optical process that results in the transformation of a pulse in a medium. As such the only parameters that determine the outcome are the input pulse and the properties of the medium. In this system we will briefly outline the two sources used for this study.

2.1μm pump laser

The 2.1μm femtosecond pump laser employed in this work was developed during the work described in chapter 3 and [64]. It consisted of a one stage, white-light seeded OPA/DFG, which generated up to 1 μJ pulses at 2.1 μm, with a spectrum from 1.6 to 2.5μm (18fs transform limit) at 3 kHz. THG Interferometric autocorrelations indicated pulse durations close to transform limit. The system was pumped from a Ti:Sapphire amplifier delivering pulses with 23fs at 800nm and operating at 3 kHz. Only around 80 μJ of 800 nm pump energy was needed to pump the OPA and white light generation stage. Energy stability of the OPA output was better than 1.5% over 1 hour. Variable compression of the output was not available. CEP stability of the pump pulse was verified to be better than 86 mrad over 7 seconds or 500 mrad over 12 min. The peak power of a 1 μJ pulse with 20 fs is of the order of 50 MW.

3.1μm pump laser

The 3.1μm femtosecond pump laser employed in this work is an OPCPA system developed at ICFO, Barcelona. Details can be found in [65]. The system outputs 85 fs pulses at 3.1μm with up to 16 μJ at 160 kHz. The energy stability of the output was less than 0.7% over 30 minutes, while CEP stability was better than 250 mrad over 11 minutes. The OPCPA system includes a compressor, which can be used to optimise pulse compression on target. The peak power of a 5-10 μJ pulse with 85 fs is of the order of 75-150 MW.

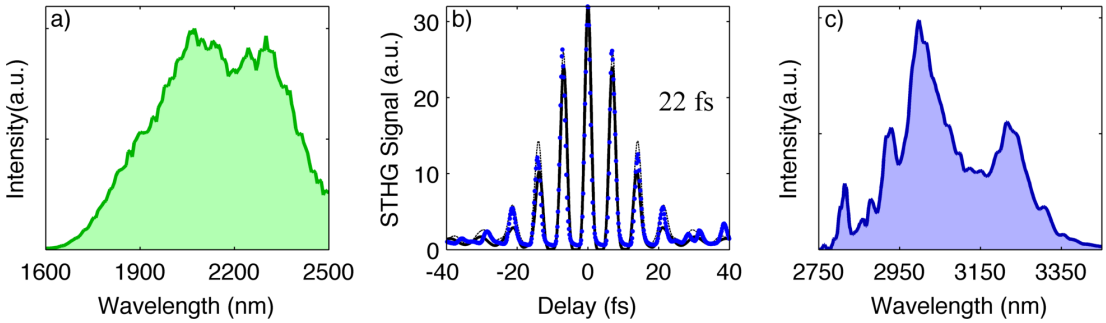

Figure 2.7: a) Spectrum for the 2.1 μm laser, supporting an 18 fs transform limited pulse. b) THG interferometric autocorrelation of the 2.1 μm laser. Blue: measured signal. Black: Autocorrelation corresponding to the spectrum in a) and a flat phase. Dashed line: Simulated autocorrelation with a phase of +55 fs^2, corresponding to a 22 fs pulse. c) Spectrum for the 3.1 μm laser, supporting a 60 fs transform limited pulse.

2.2.2 Experimental setup

The experimental setup for filamentation in solids is quite straightforward compared to other supercontinuum generation methods based on geometrical confinement - as long as the pump laser is adequately focused on the solid medium with sufficient peak power, filamentation will occur and nonlinear effects will take place. No precise coupling or positioning is needed, although an optimisation of the position of the medium across the waist of the beam proved essential to get the best signal. As studied in [54], low NA focusing generally improves the supercontinuum breadth and spectral density in the plateau and long wavelength tail. In this work we found focal lengths of 5 cm/7.5 cm yielded the best results in the 2μm/3μm case, respectively. The pulses were focused on a 2mm YAG plate, positioned close to the focus of the lens, adjusted to maximize the spectral breadth of the output spectrum. A small filament was visible inside the YAG plate. The broadband beam propagated through the YAG plate was then collimated using a 5 cm CaF2 lens. The power contained before and after the YAG plate was measured with a thermal power meter.

Spectral Measurements

Two different spectral measurements were done: the integrated spectrum to determine the breadth and spectral energy density of the supercontinuum with optimal signal to noise ratio, and a measurement of the far field profile (λ, ω). Due to the multiple spectral regions our sources span (Visible, NIR, SWIR, MIR) several spectrometers and detectors were needed, as no current photodetector technology is sensitive across the whole range. Measurements from the visible up to 1.0 μm were done with a Silicon CCD array spectrometer (Ocean Optics HR4000), while from 1.0 μm to 2.5μm an extended InGaAs CCD array spectrometer was used (Ocean Optics NIR256). For the measure-

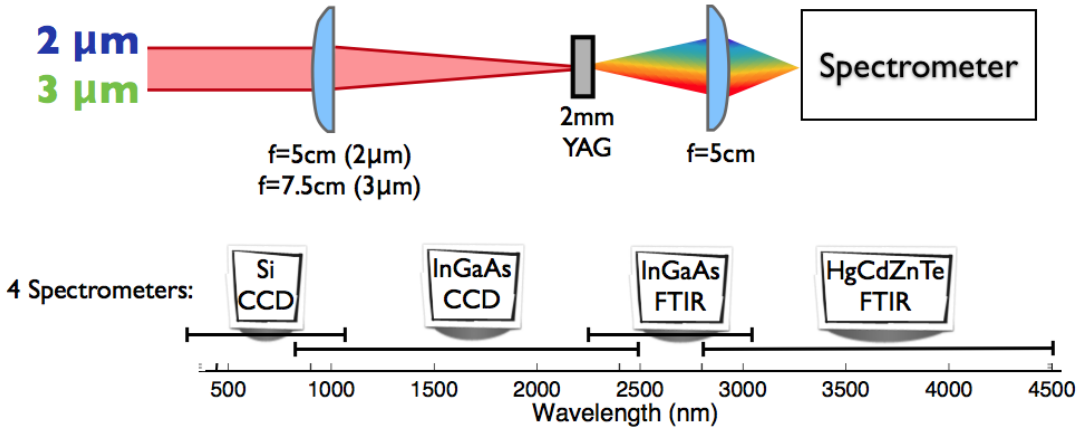

Figure 2.8: Top: Schematic of the experimental setup for the spectral measurements. Bottom: Schematic of the spectrometers used for each wavelength range.

ments above 2.5 μm an FTIR spectrometer was used (Newport 8035), where by changing the detector one could access different wavelength ranges. An extended InGaAs detector allowed measurement from 2 to 2.7μm (Newport 80014) and a thermoelectrically cooled HgCdZnTe detector (Newport 80016) measured the spectrum from 2.7 to 4.5μm. Although in theory the HgCdZnTe detector could measure from 1 to 6μm, the usable region of the spectrum in terms of signal to noise was restricted to 2.7-4.5μm. For the far-field measurements a nitrogen cooled HgCdTe detector was now available, covering the range of both detectors used in the FTIR spectrometer (2-4.5μm). All spectrometers were intensity calibrated with a 2850K black-body source. Measurements of the 2μm source with the FTIR spectrometer were not possible as the repetition rate (3 kHz) is too low and the FTIR detectors are not triggerable. Hence measurements of the 2μm-pumped supercontinuum were limited to 2.5μm and the long wavelength tail was not investigated. For the integrated spectrum measurements the beam was coupled into an optical fiber - a silica fiber for the Si and InGaAs spectrometers and a chalcogenide glass fiber for the >2.5μm measurements. The spectra were then joined at the overlapping regions and calibrated to the spectral density in pJ/nm using the measured average power of the source and repetition rate. The thermal power meter used to measure the average power is based on has a flat response over the measured wavelength range. In the far field profile measurements, three optical fibers closely mounted parallel to each other and displaced horizontally were scanned as a single unit across the beam, 54mm after the exit of the YAG plate. Two silica fibers were coupled into the Si and InGaAs CCD spectrometers, while a chalcogenide fiber was coupled into the FTIR spectrometer using the HgCdTe sensor. The spectra were joined at the overlapping regions and then scaled to the spectral density in pJ/nm.

Absolute phase coherence measurement

In order to ascertain that this source has indeed a shot-to-shot reproducible electric field we have measured its phase stability through f-2f interferometry [52]. The beam was focused on a 1 mm thick BBO crystal for Type I SHG generation at 1600 nm. The supercontinuum and the generated SHG were then collimated and projected on the same axis through a polarising beam splitter at 45 degrees with both beam polarisations. By coupling this beam into a CCD spectrometer (Ocean Optics HR4000), the spectral interference between these two beams could be measured, where the phase of the fringes in the measured interference pattern depends on the absolute phase of the electric field. By monitoring the phase of the interference fringes over time one can calculate the stability of the absolute phase using Fourier transform spectral interferometry [66, 67].

The f-2f nature of the fringes was confirmed by modulating the CEP sinusoidally by changing the pump-seed delay in the DFG stage of the OPA/OPCPA, and consequently observing the same measured CEP behaviour.

2.2.3 Integrated spectra

The spectral energy density of the generated supercontinuum when pumping at 2 μm is represented in figure 2.9(a), for different positions of the YAG plate along the propagation direction. The high spectral density at 2 μm is inherited from the pump, reaching $>$ 1nJ/nm around 2 μm and almost 100 nJ/nm in visible/NIR. Notably, a dispersive wave is generated between 500 nm and 1 μm, more than one octave away from the center wavelength of the pump. A low intensity plateau is observed between the pump and dispersive wave, similarly to [57]. No significant THG signal is measured, as the generated THG is orders of magnitude less energetic than the dispersive wave and can only be discerned when there is no significant supercontinuum generation.

The integrated spectrum measurement of the 3μm-pumped supercontinuum is exhibited in figure 2.9(b). This spectrum spans 3.3 octaves (450 nm-4.5μm) and has spectral densities from 10 nJ/nm around the pump wavelength to a few pJ/nm in the NIR. The measurement of the extent of the long wavelength tail was limited to 4.5μm due to the noise level of the detector above these wavelengths being too high - still at 4.5μm we have 10 pJ/nm of spectral density, and the long wavelength tail is usually exponentially decaying with increasing wavelength, according to the literature [54].

The spectrum is smooth and is free from major spectral structures typical from pulse splitting events during filamentation [68] such as spectral fringes, hinting that the temporal structure of the pulse is clean and there are no significant pre/post-pulses generated during nonlinear propagation. This will be studied numerically in section 2.3.

2.2.4 Far-field profiles

In order to better understand the physics underlying the generation of these broad supercontinua we have investigated the presence of conical waves by measuring the far field profile of the pulses (λ,θ), represented in figure 2.10 (2 μm pump) and figure 2.11 (3

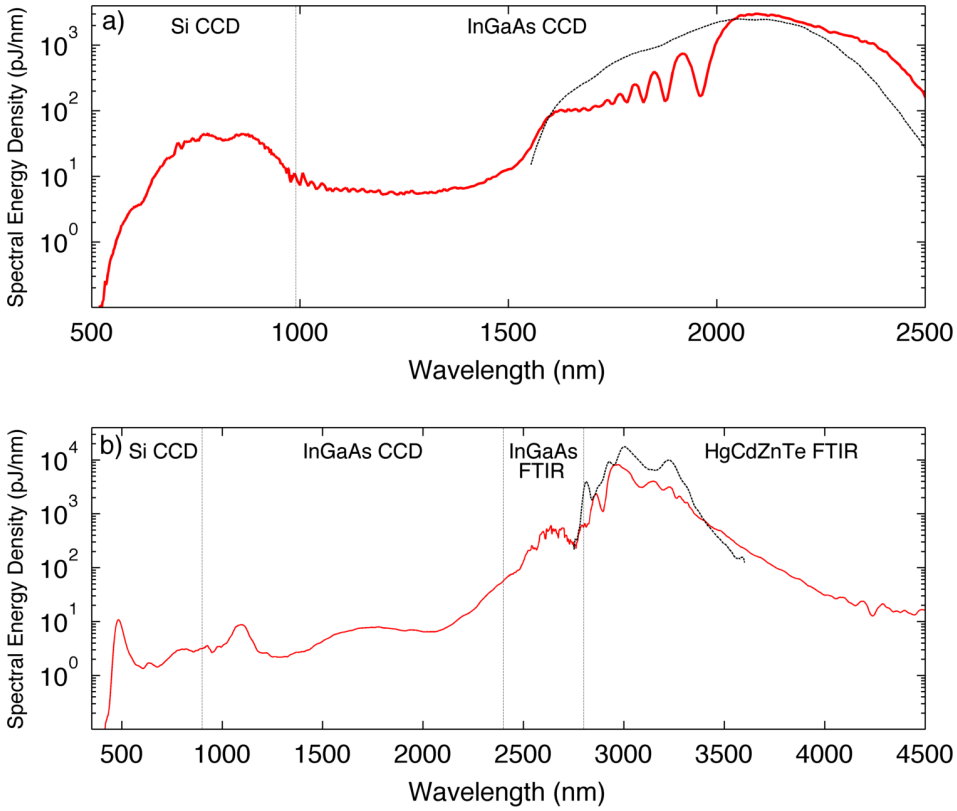

Figure 2.9: Spectral measurements. (a) Spectral energy density measurement for the 2 μm supercontinuum. Dashed black: Pump laser. Red: Measured supercontinuum. (b) Spectral energy density measurement for the 3 μm supercontinuum. Dashed black: Pump laser. Red: Measured supercontinuum.

μm pump laser). Due to the scanning nature of the measurement not as many averages were done for each spectral acquisition, hence the signal to noise ratio was not nearly as good as in figure 2.9.

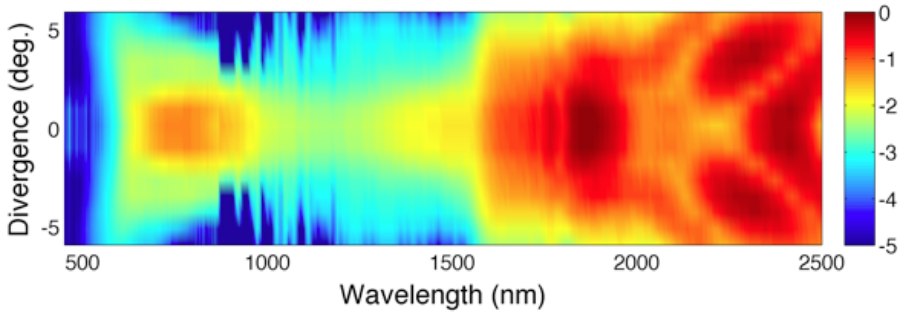

Figure 2.10: Measured far field profile of the 2 μm supercontinuum, exhibiting an X-wave between 500 and 1000 nm.

In both cases there is the generation of X-waves in the regions of the spectrum corresponding to normal dispersion and seemingly O-waves in the region of anomalous, as expected [59]. The plateau regions between conical waves seem to be free of any particular spatiospectral structure, and seem to have a smaller divergence than the pump beam. In the 2μm case peculiar spatio-spectral patterns have been formed above 2000nm. Further work is needed to ascertain the nature of these. In the 3μm case we observe an X-wave in the visible.

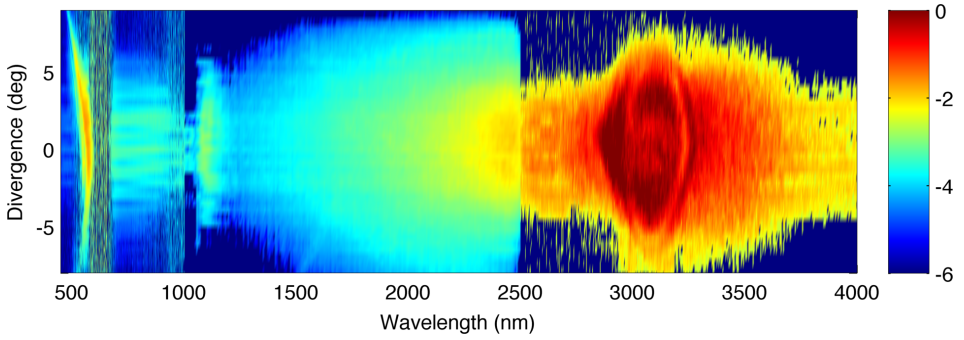

Figure 2.11: Measured far field profile of the 3μm supercontinuum, exhibiting an X-wave between 500 and 1000 nm. The dynamic range of the measurement varied between spectrometers. The lower signal to noise ratio when compared to the integrated spectral measurements is due to a much shorter averaging time per spectrum, as many spectral measurements need to be made in succession.

2.2.5 CEP stability

To quantify the shot-to-shot reproducibility of both supercontinua we performed f-2f measurements of the carrier envelope phase stability. The results are summarised on figure 2.12. The RMS stability noise of the phase jitter of the 2μm SC was 87 mrad measured over 7s, or 641 mrad measured over 6 minutes. This demonstrates that the source is coherent and there are no chaotic nonlinear processes leading to significant waveform variations from shot to shot. Notice that this noise is inherited from the OPA, and most of this noise is low frequency noise, as can be seen from the good stability with a low observation time. The presence of low frequency noise is not surprising, given the high power pump laser used to pump the 2 μm OPA, which is especially sensitive to slow environmental noise. As will be demonstrated in section 3.4.2, this slow noise can be successfully eliminated by implementing a feedback loop in the OPA. In the 3μm SC (fig 2.12) the measured jitter was 250 mrad over 11 minutes.

Additionally, one can argue that this measurement only confirms the delay stability between the frequencies at 700-800nm and 1400-1600nm. This is indeed true, albeit from the current understanding of the physics of supercontinuum generation this value is equal or worse than the global phase stability, as this section of the spectrum is further away from the main peak, hence more susceptible to intensity to GDD coupling. Given this, an f-2f measurement from 450 to 2250nm would be needed to give such assurance, which is in principle possible but quite a technical challenge.

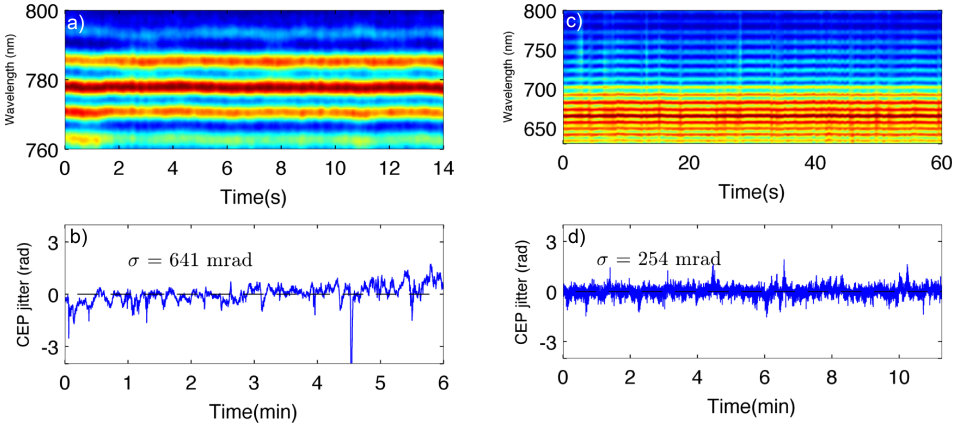

Figure 2.12: Phase stability measurements of the supercontinua. (a) Observed f-2f spectral finges from the 2 μm SC, revealing a CEP stability of 87 mrad over 7 s. (b) Longer measurement revealing the low frequency nature of the CEP drift. (c) Observed f-2f spectral finges from the 3 μm SC, demonstrating CEP stability. (b) Long term measurement, revealing a stability of 254 mrad over 11 minutes.

2.3 Simulations

In order to gain a better physical understanding of the nature of the observed supercontinua and its spatiospectral features we performed numerical simulations of nonlinear pulse propagation and analysed the resulting data. This not only allows one to test whether current theory correctly explains the processes behind filamentation but also to get insight into unmeasurable or difficult to measure quantities such as the spectral evolution throughout propagation, or the pulse temporal structure.

2.3.1 Approach

3D numerical simulations of nonlinear pulse propagation through YAG were performed by Prof. Arnaud Couairon, with initial conditions modelling the experimental ones. A radially-symmetric pulse was propagated in the forward direction using the forward Maxwell equation, where the medium polarisation includes dispersion, χ_3 nonlinear effects and plasma-related effects. A detailed description of the numerical methods used to solve the problem is given in [69], while an extensive overview of how the different effects that play a role in filamentation are modelled is given in [44]. A medium modelling YAG was modelled considering a ionisation potential of 6.5 eV, a linear refractive index given by the Sellmeier equation in [70] and a nonlinear refractive index $n_2 = 7 \times 10^{16}$ cm^2 W^{-1} [71, 72]. No dispersion on n_2 was considered in this model. Note that the parameters and models used can have a considerable uncertainty over such a wide spectral range, which undoubtedly will make precise agreement between theory and experiment hard. Nonetheless we have found that the main features of the measurements are satisfactorily reproduced.

2.3.2 2μm and 3μm simulations

Represented in figures 2.13 and 2.16 are the simulated far field profiles of the generated supercontinua, for the two different pump lasers. Comparing the simulated spatiospectral profiles with the measured ones we find agreement on the breadth of the supercontinuum, as well as in the structure of the conical waves. Around the driving laser wavelength we observe the formation of O-waves, as expected from filamentation in the anomalous regime [59], while at the lower wavelengths region an X-wave/fish-tail is generated, as this region is in the normal dispersion regime hence subject to a different conical phase matching condition [57]. The X-wave structures also appear with different Kerr coefficients and ionization rates. Increasing n_2 up to a factor of 4 leads to a broader extent of the main spectral peak and a change in the balance between third-harmonic generation and the supercontinuum. Higher Kerr coefficients lead to a prevailing fishtail with respect to the third harmonic. Fig. 2.16b) shows the beam size during propagation in the 2 mm YAG plate for the 3 μm simulation of Fig. 2.16. The beam undergoes several self-focussing events and does not diffract over a distance greater than the Rayleigh range. Regarding the measured feature at 1μm in Fig. 2.16, it is not reproduced in the simulations. A similar feature is present after 0.7mm of nonlinear interaction, but further

copropagation up to 2mm with the intense pump causes significant reshaping which leads to the simulated result. Uncertainties in the medium and pump parameters could cause such disagreement. Additionally, note that the absence of fringes in the measurement indicates that the nature of this feature is related to non-THG effects, as efficient THG generation simultaneous with broadening would result in clear CEP-dependent fringes.
.

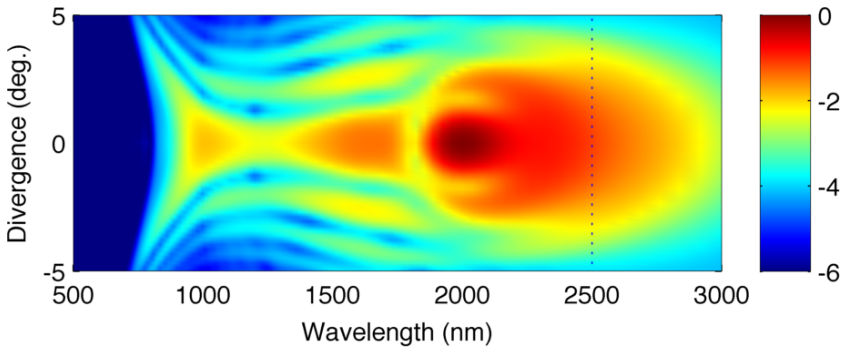

Figure 2.13: Simulated far-field profile at the output of the YAG plate when propagating a 30 fs pulse at 2μm, reproducing some of the features of the experimental results in figure 2.8. Dotted line: limit of measurement in figure 2.8.

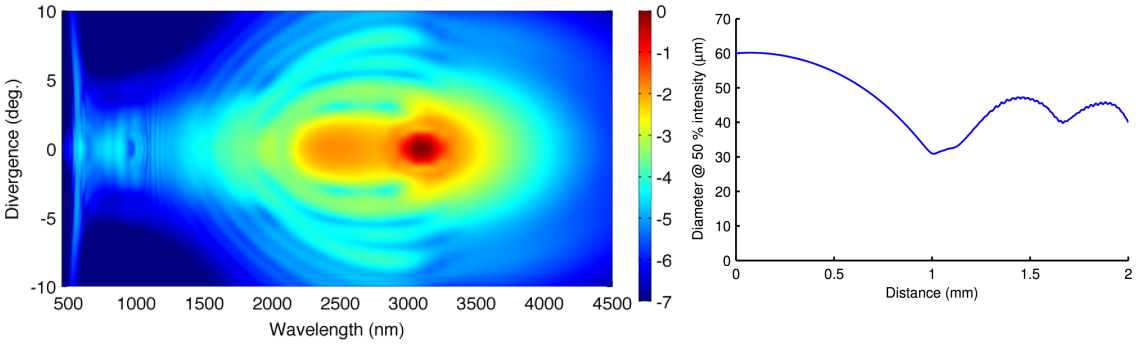

Figure 2.14: Simulated far-field profile at the output of the YAG plate when propagating a 85 fs pulse at 3μm, reproducing both the breadth and fish-wave nature of the experimental results in figure 2.9. a) Far-field profile. b) Beam diameter evolution during propagation.

2.3.3 Pulse profiles from simulations

Given the overall agreement between the simulated and measured spatiospectral profiles we used the 3D simulation to gain insight into the temporal propagation dynamics. We

find that in the 3 μm case, due to a favourable interplay of linear and nonlinear effects the pulse temporal profile on-axis significantly shortens (fig. 2.17), while a post pulse with less than 30% of the peak intensity is formed. The resulting predicted pulse has an intensity FWHM duration of 7.2 fs. The interplay between SPM with positive n2 and anomalous dispersion tends to both generate new frequencies as well as to compress them in the peak of the pulse, extending the nonlinear interaction length and possibly supporting spatiotemporal solitonic action [73]. This suggests that the broadening process can have a stabilising effect and be robust in regards to input pulse fluctuations, which would be of interest to demonstrate experimentally. Examining the spectrogram of the on-axis pulse reveals that indeed all frequencies are approximately compressed, without any complex structures having formed. This suggests that the output phase of the supercontinuum is smooth and well-behaved, which is of interest to many applications.

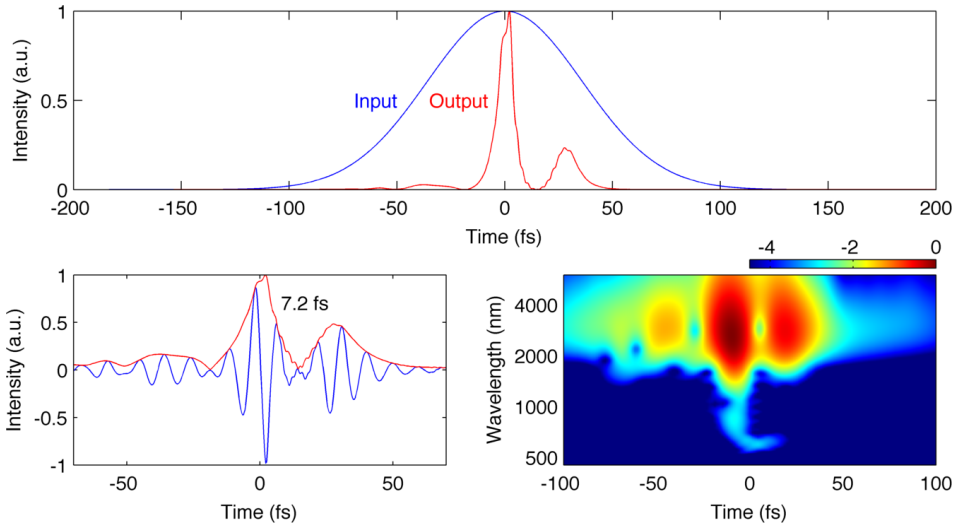

Figure 2.15: Numerical prediction of self-compression for the on-axis pulse undergoing filamentation in the YAG plate. (a) Blue: initial 85 fs gaussian input pulse normalised intensity profile. Red: propagated on-axis pulse normalised intensity profile, predicting an a ten-fold self-compression effect in the temporal duration (b) Electric field (blue) and (envelope) of the output pulse. (c) Spectrogram of the output pulse, revealing that the short-wavelength frequency tail exits the YAG plate simultaneously with the main peak.

2.4 Conclusion and future steps

In this chapter we have demonstrated multi-octave phase-stable supercontinuum generation through filamentation in bulk material of SWIR-/mid-IR femtosecond pulses. The measured spectra spanned 500-2500 nm when pumping at 2.1 μm and 450-4500 nm

(corresponding to 3.3 octaves) when pumping at 3.1 μm with a spectral energy density of 1 pJ/nm-10 nJ/nm. The intensity and phase stability indicate shot-to-shot stability of the waveform. We obtained an angularly resolved far-field spectrum with the main features captured by full 3D simulations. This approach demonstrates a simple and robust method for coherently extending the spectrum of an amplified femtosecond mid-infrared pulse down to the visible. Further extending the spectrum down to the UV should be possible using media with a larger band-gap and different dispersion profile, while simultaneously increasing the input energy, e.g. CaF_2 or LiF or similar [74]. Additionally, extrapolating this trend one can hypothesise that by pumping further into the mid-IR one could develop fully coherent light sources capable of spanning several important parts of the electromagnetic spectrum simultaneously (spanning from various important organic absorption lines at 6 μm to important excitation lines in the visible/UV).

Due to a mix of favourable nonlinear effects, self-compression is theoretically predicted, while the measured angularly resolved far-field spectra agree with the numerically simulated ones. The predicted self-compression effect was later successfully experimentally verified in the PhD thesis of Matthias Baudisch and the work of Michael Hemmer [75].

Despite self-compression effects, convenient usage of pulses with such broad spectrum in different experimental conditions demands variable dispersion compensation, to compensate propagation through eventual dispersive media. Several approaches to this problem are possible, albeit all of them pose a big challenge over such broad spectrum: a) a 3-octave pulse shaper, possibly built with a small apex prism as the dispersive element and a deformable mirror; b) specially designed chirped mirrors, which pose a big design challenge due to the inverse relation between attainable compensation magnitude and bandwidth [76] - for such a broad spectral range a great number of reflections would be needed, which would eventually introduce a residual oscillatory phase which would greatly diminish the peak power; c) a multi-channel compressor, where through dichroics narrow parts of the spectrum are separated, dispersion compensated and then later recombined with the right delay. This last approach has been demonstrated to work with a spectrum covering 2 octaves [23], relying on a great number of custom coatings.

If minimum pulse duration is the objective then amplitude shaping can greatly help optimising it, although at great expense of total pulse energy. Attenuating the region between 2.5 and 4μm to 0.1% one can reduce the intensity FWHM of the TL pulse to a single half-cycle (figure 2.16(a)). This would reduce the spectral energy densities to 10 pJ/nm across the whole spectrum, which is enough for most pump-probe studies. Even though this reduces the energy to 3% of what it was, the reduction in attainable pulse duration leads to a comparable peak power in this scenario, if all frequencies are compressed (24%).

An alternative approach to the compression of this spectrum that would employ more standard 'designs' would be to build a multi-channel compressor based on several prism or grating compressors. By recombining the (long) output from each compressor with the appropriate delay, one can optimize the interference between channels to achieve a sub-cycle pulse duration (Figure 2.16). Each of the channels can still have residual TOD

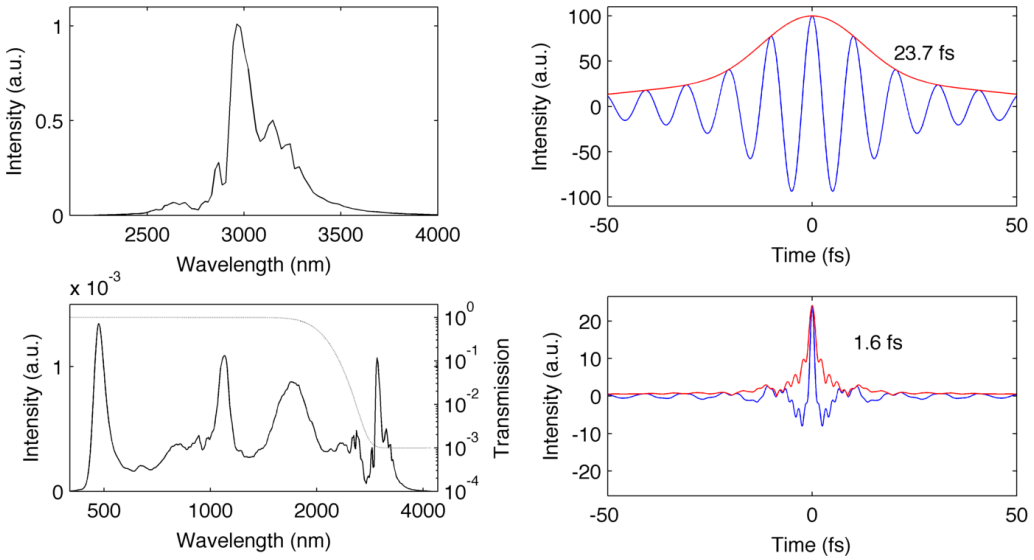

Figure 2.16: Possible temporal pulse shapes supported by the generated spectrum. By compressing only the long wavelength region represented in (a) with high efficiency one could in principle generate a few cycle pulse (23.7 fs) with more than 5 μJ, which could be used for strong field experiments. If a significant energy loss is acceptable then a much shorter TL pulse can be achieved by attenuating the spectrum in the long wavelength region by applying an amplitude filter. This filter would fully transmit below 2μm but have 0.1% transmission in the 3μm region with a smooth transition in between (dashed line, (c)) leading to a spectrum with almost constant intensity from 500 nm to 3.5 μm (black line (c)). By compressing this whole spectral range one could in principle generate a sub-cycle pulse with an intensity FWHM of 1.6 fs, or 780 attoseconds of E^2 FWHM, using the same criteria as in [10]. Note that even though the spectrum in (c) only has 3% of the energy of the spectrum in (a), the corresponding TL pulses have peak powers with the same order of magnitude (24%), owing to the much shorter pulse duration in the case of (d).

and FOD, but since the delay between channels is adjustable individually these low dispersion orders will become 'local' phase features, only diminishing the peak power and creating satellite pulses, but retaining a short main peak pulse duration (Figure 2.16). Given this, separation of the different spectral channels and adequate temporal jitter compensation between them would also significant problems to solve with this approach.

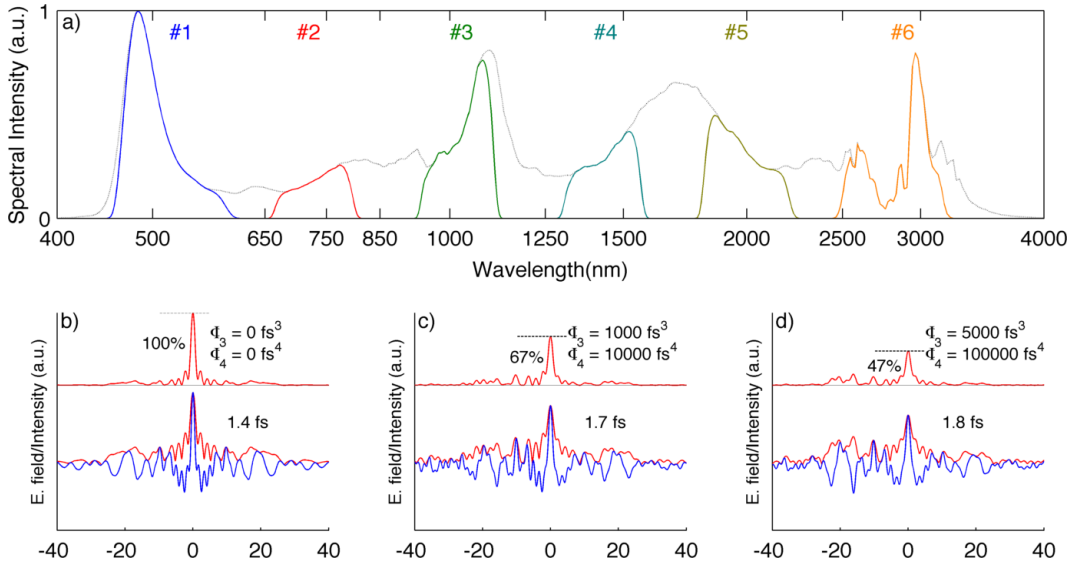

Figure 2.17: Illustration of a possible strategy to recompress the generated spectrum down to the sub-cycle regime with current technology. (a) The amplitude shaped spectrum is split through dichroic mirrors into 6 wavelength ranges, each of them recompressed using a prism or grating compressor. Gaps between the spectral ranges are considered to reduce spectral width of each channel and ease compressor design. All channels would then be recompressed and synchronised into the same beam. (b) Achievable pulse considering perfect compression without residual phase in any of the compressors. Top: Intensity profile, having a 1.4 fs FWHM duration. Bottom: Electric field. (c) Achievable pulse considering that all compressors have a residual phase of 1000 fs^3 and 10k fs^4 for zero GDD, leading to an 1.7 fs sub-cycle pulse with 67% of the peak intensity of the perfectly compressed case. (c) Achievable pulse considering that all compressors have a residual phase of 5000 fs^3 and 100k fs^4 for zero GDD, leading to an 1.8 fs sub-cycle pulse with 47% of the peak intensity of the perfectly compressed case. The feasibility of this scheme is not only limited by the availability of dichroic optics to separate and recombine the spectrum, but also by the scheme used to keep all the different channels synchronised, which is not (yet) a trivial task.

If enhancing the energy is needed, for example for applications in e.g. strong field physics, there are currently two approaches that might be appropriate. First, Fourier-plane OPA [77] could be used to amplify such broad bandwidth, as with this arrangement

crystal phase matching requirements can be relaxed. Pump optimisation can also be used to apply a stronger gain in certain parts of the spectrum and not others, allowing amplitude shaping. Additionally, the Fourier plane arrangement doubles as a phase shaper. Another approach would be serial OPAs with different crystals [78], which given good dispersion compensation allows a much simpler setup. Finding the crystals with the right amplification bandwidth and full transparency between 500 and 4.5μm is another pending issue.

Chapter 3

High intensity, few-cycle phase-stable pulses at 2 μm: towards phase-matched HHG in the water window

3.1 Intense few-cycle femtosecond laser development

Over the last 20 years research fields such as strong field physics[79] and more recently attoscience[17] have relied on intense femtosecond lasers sources to study and control physical processes. Notably, the development of Ti:Sapphire (Ti:Sa) CPA technology [80, 81, 82] was particularly enabling, as it allowed for the first time the construction of short pulse lasers with the appropriate specifications for productive scientific use.

Additionally, the invention of carrier-envelope phase stabilisation schemes[52] allowed the realisation of stabilised frequency combs [83], as well as high intensity waveform-controlled electric fields [63], which are in turn allowed the generation and measurement of an isolated attosecond pulse [84] for the first time.

Despite its success, Ti:Sa technology does not cover all use cases, specifically it only generates pulses around the emission wavelength of the gain medium (650 nm-1100 nm). Additionally, due to gain narrowing limitations nonlinear pulse compression schemes are necessary to reach the intense few-cycle regime, which increases complexity and limits reliability. Recently, a desire to explore new physics by driving light-matter interactions with longer wavelengths has emerged, hence the development of new sources is necessary. In this project we set to build a few-cycle laser system at 2 μm with mJ-level energy for high harmonic generation. In the following sections we will briefly discuss the state-of-the-art in broadband few-cycle pulse generation in the SWIR and MIR, and follow by presenting our system design and results. We will then present results from the application of these pulses to HHG and shortly conclude, indicating a few future directions for this line of work.

3.2 Current approaches

Laser development of oscillators and amplifiers based on stimulated emission in the SWIR/MIR has been concurrent with Ti:Sa systems [85, 86], but only recently has the few-cycle regime been demonstrated ([31]). Parallel to stimulated emission systems, the development of parametric amplification based on χ^2 processes [87] made possible the simultaneous amplification of much broader coherent spectra, as the amplification bandwidth in Optical Parametric Amplification (OPA) is no longer dictated by an existing stimulated emission transition, but by the phase-matching properties of non-centrossymetric materials, where much more flexibility exists.

Similarly to CPA, in order to be able to scale energy and power to regimes not allowed by Ti:Sa technology, Optical Parametric Chirped Pulse Amplification (OPCPA, [88]) is another alternative, where the pulse to be amplified is stretched to match the duration of a longer pump pulse. This allowed the use of other pump laser technologies, where the gain medium has a narrow emission line not supporting the fs regime, but that are more practical or scalable than Ti:Sa. Thanks to this method few-cycle pulses with high average power from the visible to the mid-IR have been demonstrated, inclusively sub-two-cycle OPCPA systems with average powers reaching tens of watts have been demonstrated (e.g. [89]), where the output power was mostly limited by the available pump power. Besides the discussed features of parametric sources, it is also possible to passively stabilise the carrier envelope phase, which is necessary for e.g. isolated attosecond pulse generation. If one parametric amplification stage is seeded and pumped with two waves with correlated CEPs which change coherently from shot-to-shot, the third generated wave will have a constant CEP from shot-to-shot [90]. This greatly simplifies system design when compared to the usual intra-cavity feedback loops, acousto-optic crystals and low jitter electronics necessary to stabilise the phase in Ti:Sa systems [63]. Up to the starting date of this project, several groups had developed CEP-stable few-cycle OPA/OPCPA systems in the SWIR/MIR range: Vozzi et al demonstrated CEP stable pulses with 1.2mJ, 17 fs at 1.5 μm, by employing Ti:Sa-pumped Type II OPA in BBO, seeded by intrapulse DFG of filamentation broadened pulses [91, 92, 93] . Unfortunately the pump laser repetition rate was 10 Hz, which limits average power (12 mW in this case), but notably they were able to attain a 3.5 cycle pulse duration without dedicated dispersion compensation optics. At similar average powers, the system from Mucke et al [94, 95], based on OPCPA pumped by Nd:YAG in KTP and BBO, seeded by a supercontinuum was able to generate 3.5 mJ pulses at 20 Hz, 1.5 μm, with a pulse duration of 74 fs, compressible to 20 fs/1.5mJ through filamentation [96]. Also following an OPCPA approach, Fuji et al [97] and later Gu et al [98], developed a system seeded by intrapulse DFG of filamentation broadened Ti:Sa, but using picosecond Nd:YLF pump technology in conjunction with PPLN amplification stages, attaining a 2 cycle (15.7 fs) pulse duration at 2.1 μm, with 740 μJ of energy at 1 kHz, with an additional copropagating 180 μJ of superfluorescence, which contributed to the 9% RMS energy stability. Similarly, Moses et al built a Nd:YLF-pumped, PPLN-based OPCPA seeded by intrapulse DFG of an octave-spanning Ti:Sa oscillator, generating 23 fs pulses at 2.3μm,

containing 200 μJ at 1kHz [99], later upgraded to 2.6 mJ [100]. At longer wavelengths, higher repetition rates and lower energies, Chalus et al generated 2 μJ, 96 fs at 3.1μm, 100 kHz [65, 101], later upgraded to 18 μJ, 67fs at 160 kHz [102].

Concurrent with this project, a number of systems were developed, including commercial white-light seeded, Ti:Sa-pumped OPA systems [103, 104]. Notably, Schmidt et al, using such a system delivering 1.2 mJ, 70 fs at 1.8 μm at 100 Hz discovered that post-compression through hollow core fiber propagation of these pulses results in broad spectrum with the opposite phase of bulk propagation in fused silica, allowing compression down to the sub-two cycle regime without sophisticated dispersion compensation [105, 106]. Additionally, Ishii et al have developed a Ti:Sa pumped OPCPA based on BiBO at 1.6 μm, capable of generating 550 μJ pulses with 9 fs at 1 kHz [107].

3.3 OPA design

In this project we set to build a few-cycle laser system at 2 μm with mJ-level energy for high harmonic generation. In this section we will detail most of the design decisions, as well as discuss some important design considerations.

3.3.1 Pump/Crystal choice

At the start of this project a KMLabs Red Dragon capable of producing up to 6 mJ, 21 fs pulse at 3 kHz was available on our laboratory. As the reported efficiencies for high-energy Ti:Sa pumped OPAs in the literature exceeded 10-20% (e.g. in [93]), a final energy above 1 mJ seemed within reach by using this laser as the pump, which was sufficient for the envisioned purposes. Given that the pump wavelength and bandwidth is set, the universe of usable crystals is greatly reduced. PPLN [108], BBO [109] and BiBO [110, 111] are regularly used for amplification above 1 μm using a broadband 800 nm pump. In order to maximise amplification bandwidth, one needs to have low group velocity mismatch between the pump and the waves to amplify, as well as between those waves. Fortunately, some materials have a zero dispersion wavelength, creating a broadband region around which the group velocity variation is minimized. Additionally, by using type I OPA (e->o+o) and choosing the appropriate cut-angle one can find a shorter wavelength whose group delay is similar to this region, in the perpendicular polarization. This process can also be explained in terms of a vanishing quadratic term in the phase mismatch calculation [112]. In the case of BiBO, the zero GVD point is at 1580 nm, which will allow an octave spanning amplification bandwidth around this value when pumped at 790nm (at 11.4° xz-cut). In comparison, BBO has a zero dispersion wavelength of 1444 nm, corresponding to a 718nm pump [110]. The octave-exceeding amplification bandwidth of BiBO when pumped by TiSa pulses has been experimentally confirmed [113], by amplifying a chirped white light continuum spanning from 1.1 to 2.7 μm up to 50 μJ energy. Subsequently, Petrov et al [112] demonstrated the feasibility of high energy scaling by extracting 1.1 μJ (signal plus idler) at 1.2 μm from a dual stage OPA pumped by a 4 mJ, 135 fs Ti:Sa amplifier. The presence of these results

in the literature motivated BiBO as the best candidate for amplification of high energy pulses at 2 μm, when pumped with a short Ti:Sa pump pulse. Additionally, it has the advantage of not being hygroscopic [110], having high transmission up to 2.5 μm, a high damage threshold (>300 GW/cm^2 for 20-40 fs pulses [110]. Testing in this thesis indicated >500 GW/cm^2), and a comparatively high d_{eff}, which further makes it more attractive than BBO or PPLN. Additionally, BBO and BiBO can be found commercially in crystals with apertures up to 25mm, which is helpful for scalability of the system, whereas PPLN is not as easily scalable.

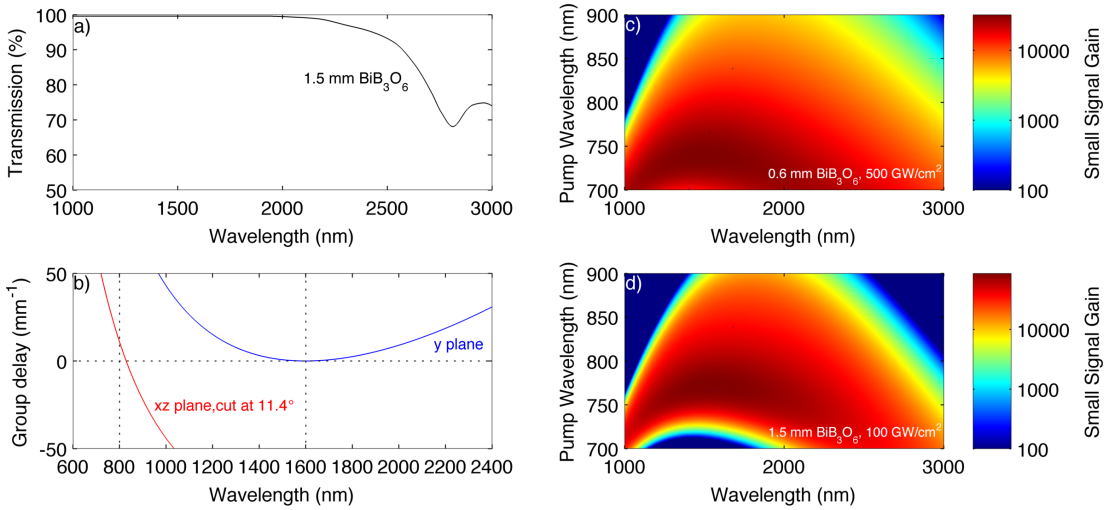

Figure 3.1: BiB_3O_6 crystal characteristics. a) Transmission in the IR of a 1.5 mm thick BiB_3O_6 sample (data from [112]). b) Group velocity in function of wavelength for the two relevant propagation axis for type I OPA in BiB_3O_6. c) Small signal gain [109] in function of pump and signal wavelength for a 0.6 mm crystal pumped at 500 GW/cm^2, a gain configuration used in this work, revealing a broadband amplification bandwidth. d) Same as c), for a different high gain configuration (1.5mm thick crystal, 100 GW/cm^2).

3.3.2 Seeding scheme

Given the octave spanning bandwidth of the amplification medium one still needs to chose a suitable seed generation scheme. As said in the previous section, difference frequency generation can be used to generate a CEP stable seed, if both pump and signal waves are derived from the same CEP-unstable laser, the idler wave will have its CEP stable from shot-to-shot [90]. This process is illustrated in figure 3.2.

In order to exploit this property one can, in principle, use one of three possible schemes, as illustrated in Fig. 3.2b) to d). If the pump laser has enough bandwidth (or if such bandwidth is generated through subsequent broadening/supercontinuum generation), one can do DFG between the edges of the spectrum of such broadband pulse by

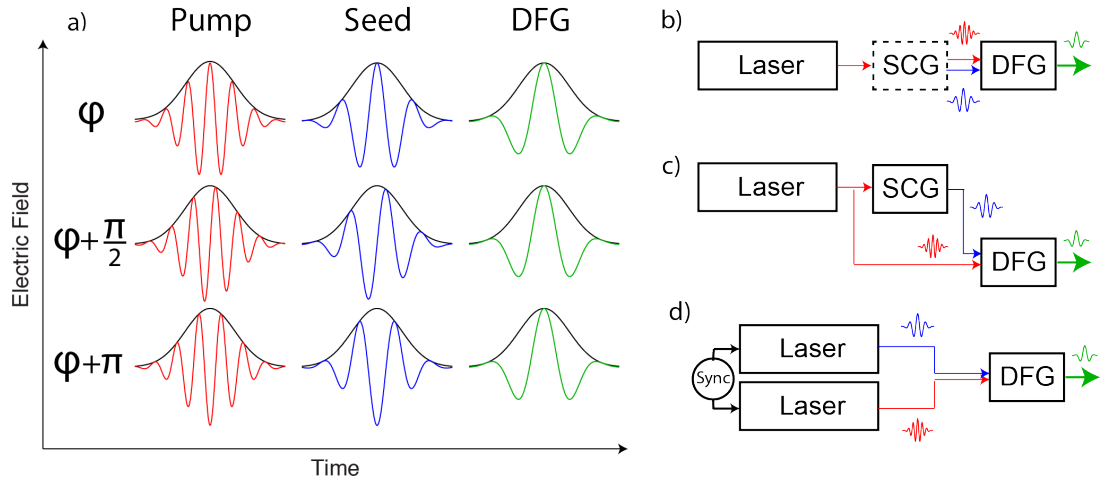

Figure 3.2: Passive CEP stabilisation through difference frequency generation. a) Illustration for 3 different CEPs of this process. For any pump CEP the DFG CEP will be the same, equal to the CEP difference between pump and seed. It follows that if the phase of both beams is not related from shot-to-shot, then the DFG phase will fluctuate. b) Intrapulse DFG scheme to generate a phase-stable idler. c) Mach-Zender scheme to generate a phase stable idler. d) Generalized scheme to generate a passively CEP stable wave.

just focusing it in an appropriate crystal with the appropriate phase. This scheme is able to generate pulses spanning from 1.1 to 2.5 μm with up to few hundreds of nanojoules [93, 97, 107]. Another possible scheme is the generation of new frequencies on the long wavelength side of the pump laser spectrum through supercontinuum generation, and then by using a Mach-Zender configuration one can do high gain DFG by combining both the newly generated frequencies and an appropriate amount of pump in a DFG crystal. This scheme has the advantage of one being able to control the pump parameters and possibly make the seed interact with much more pump energy than in the previous scheme. With this method it is typical to generate μJ level pulses after the DFG interaction [109]. A third scheme is based on DFG between two synchronised laser sources. The previous scheme is a particular, simple case of this scheme, which can in principle accommodate optical or electronic synchronization, as well as additional SCG, further amplification, additional nonlinear processes, etc. Since the interferometric stability between the two waves will determine the actual CEP stability of the DFG output care must be taken that the synchronisation mechanism attains jitters less than a fraction of the optical cycle. Optical synchronisation is routinely able to provide this with proper interferometer design, but few electronic systems are able to do sub-cycle synchronisation (e.g. Balanced optical cross correlators [114] and the Hänsch-Couillaud method [115]). In this work we have decided to use the scheme in figure 3.2 c), i.e. using WLG in solids to generate a nJ seed at 1.3 μm, for reasons of compactness and simplicity. Additionally, previous experience from members of the team with high energy nonlinear compression in gas indicated that it can be unreliable in certain situations, while filamentation in solids is well understood [54, 63], is typically more reliable, has low energy requirements, and is easy to troubleshoot in day to day operation. There are also benefits in efficiency compared to the first scheme: for comparison in [107] 300 μJ were used to generate 100 nJ of seed using the second scheme, while in our work $<$100 μJ were used to generate 1 μJ, in a more compact setup. Despite this, due to the intrapulse nature of the first scheme contrasting to the Mach-Zender configuration used in the second one, it is expected that the CEP stability attained with the first method is better. Recently, a method to generate 41 μJ seed pulses using intrapulse DFG was demonstrated [116] with 0.33 mJ of input power, although it requires pulse compression to sub-4fs at 800nm - which is not straightforward, as will be explained in chapter 4. Given that, this scheme would enable a significant simplification of the OPA part of the system, as amplification would start already at the tens of microjoule level with appropriate bandwidth.

3.3.3 OPA vs NOPA

For the DFG stage one needs to use a collinear geometry in order to generate a CEP stable pulse without any angular dispersion. Two more OPA stages were used to amplify this CEP-stable seed to mJ-level energy. The traditional motivation to use a non collinear geometry in OPA is to increase amplification bandwidth [117]. Given the octave-exceeding bandwidth that BiBO posses in a collinear geometry, owing to a very low group delay mismatch between pump and signal in Type I OPA (1.1-2.7 μm) we

have designed the two OPA stages as collinear (initially), as it simplifies alignment, beam paths and matching pulse fronts (which can be an issue when pumping with a short pulse). In final iterations of the system a small non collinear angle (<2 deg) was used to ease beam separation and remove the need for a dichroic combiner, which is dispersive. We have found no influence of this angle on the amplification bandwidth for the thin crystals used (<1.5 mm).

3.3.4 Pump bandwidth transfer and travelling wave amplification

The typical mindset of OPA and OPCPA involves thinking of the pump wave as an energy reservoir and the seed wave as containing the bandwidth that will allow a short pulse to be generated. This is true for amplification stages in general, but in the specific case of using a broadband pump in a DFG stage the possibilities are more interesting in terms of bandwidth transfer (of course, within the phase-matching possibilities that the crystal allows). If our broadband pump is well compressed, the gain will be temporally limited to the duration of the pulse, leading to a generated third wave/DFG with a similar pulse duration. If the seed is also compressed, then the effect of the higher gain at the peak of the seed pulse will result in a temporally narrowed DFG wave, whose spectral breadth is bigger than each of the other two waves (fig 3.3a)).

If, however, the seed is not well compressed, the short pump will overlap in time with only a portion of the seed spectrum and generate a DFG wave with a narrower spectrum, whose duration and spectral breadth are equivalent to the pump (Fig 3.3b)). This situation is similar to the case of seeding the DFG with a narrowband signal. Additionally, notice that in this case the spectral breadth of a broadband pump pulse (e.g. a 25 fs pulse from a Ti:Sa amplifier at 800nm - 10 cycles), can eventually be used as the pump to generate DFG at a much longer wavelength, which can result in a much lower number of cycles (e.g. 25 fs is 2 cycles at 3.75 μm). Hence broadband pump DFG can serve as a straightforward route to generate few-cycle supporting spectra at SWIR/MIR wavelengths, given that an adequate pump and crystal pair is available. In the case of uncompressed pump pulses (only residual GDD will be considered on our analysis) three main situations can arise. If the seed is compressed, the seed bandwidth and pulse structure will be transferred to the generated wave (not represented in Fig 3.3) but the efficiency of the process will be low. In case the seed is stretched to better interact with the pump and increase efficiency, the other 2 situations arise. If both pulses have opposite GDD signs, then the opposite edges of each spectrum will interact, resulting in a DFG pulse with up to as much bandwidth as if both seed and pump were compressed, although with significant GDD (Fig 3.3c)). In the case of similar GDDs, the same edges of the two spectra will interact and result in a possibly much narrower spectrum than the input ones (Fig 3.3d)). One important situation for the work of this thesis is when the seed wave has significant TOD. In this case the pump pulse is well compressed, the TOD will not be transferred to the generated wave (to a certain degree). It is worthwhile to note that these considerations are only valid when the GVM between pump, signal and idler is low. Only when all waves travel with similar group velocities in the nonlinear medium can the process be thought of as travelling wave amplification. To summarise, in

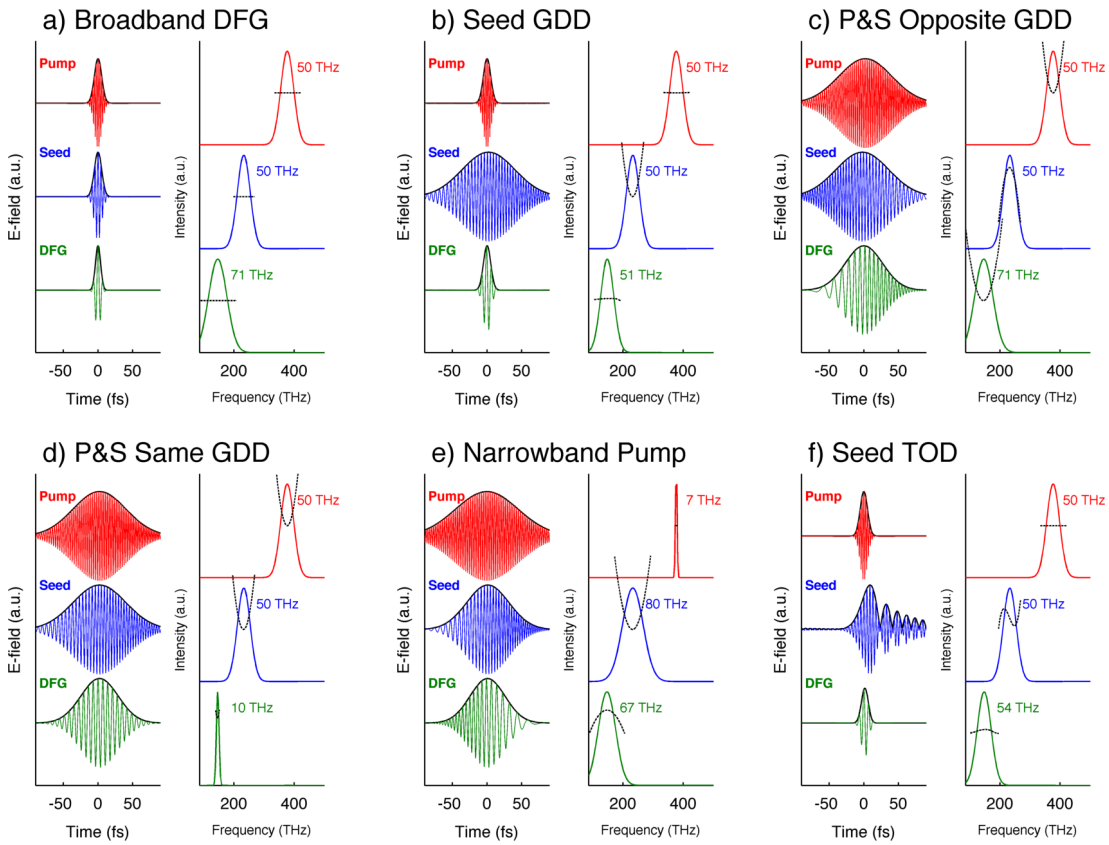

Figure 3.3: Illustration of pump/seed bandwidth transfer to the generated wave during DFG, for an infinitely thin medium. Representation in the temporal domain (left) and corresponding spectrum and phase (dotted lines) in the spectral domain (right) for 6 relevant situations. a) DFG with short pump and seed, leading to a generated wave with more spectrum than the input waves due to temporal gain narrowing. b) DFG with short pump and stretched seed (or equivalently short pump and narrowband seed), leading to the pump bandwidth/pulse duration being transferred to the generated wave. c) DFG with stretched broadband pump and seed with opposite GDDs, leading to the same bandwidth as the compressed case, but with residual GDD. d) DFG with stretched broadband pump and seed with the same GDD. The energy difference between the temporally overlapping instantaneous wavelengths is constant across the pulse, hence a narrowband pulse will be generated. e) DFG using a narrowband gaussian pump and a stretched broadband seed, leading to a generated wave with the opposite GDD. This property can be useful in OPCPA (e.g. [118]). f) DFG in the presence of heavy seed TOD. Due to the temporal gating the gain bandwidth is lost, but the TOD is not transferred to the generated wave.

order to extract large bandwidths from a DFG stage with a broadband pump, it might be sufficient to assure that the pump and seed don't have the same GDD (ignoring efficiency optimisation considerations). If bandwidth exceeding the pump bandwidth is desired, then careful matching of opposite phase between seed and pump can be helpful. Additionally, when the pump is compressed, the TOD of the seed is not transferred to the DFG output. An additional remark is that in the case of amplification of the seed wave (instead of generation of a third wave), short temporal gain due to a short pump pulse duration is of little use if the seed duration does not match it, only leading to a decrease in amplification efficiency and bandwidth. Hence a broadband pump is quite attractive for DFG stages, but poses additional complications for amplification stages, as will be seen in this chapter.

3.3.5 Design considerations: managing dispersion across the OPA chain

When designing ultra broadband OPAs one has to take into account that dispersive propagation of the pulse the elements of the setup may significantly stretch or compress the pulse, which can both mismatch the seed-pump pulse duration and decrease conversion efficiency, but also produce a stretched pulse at the output of the OPA, that is harder to compress to a few-cycle pulse duration. Initial designs were based on balancing propagation through materials with positive and negative GVD (figure 4.5), but since all materials available had positive TOD this lead to uncompensated high order phase which prevented good final compression at the output. Additionally, the gain narrowing resulting from the gaussian pump temporal profile reduced the final amplified bandwidth, since the seed pulse has a slightly residual GDD at both second and third OPA stages. Precise removal of this GDD using dispersive propagation would lead to even higher final TOD, and further stretching of the pump was found to lead to reduced conversion efficiency. The possibility of going to a stretched seed design, with a simple compressor at the end of the system and stretched pump pulses was investigated but quickly abandoned, as it would require significant changes and would add a lot of complexity to the system, which would become a broadband pump OPCPA. In later designs we prioritised removing as much dispersion from the beam path as possible, and managed to keep both the amplification bandwidth as well as the efficiency across the OPA chain. Additionally, by amplifying the signal in the first OPAs and delaying the DFG till the end we managed to reduce the total accumulated GDD through propagation, as the signal wavelength (1.3μm) is at the zero dispersion wavelength of fused silica, which most of our optics were made out of.

3.3.6 Design considerations: separation of signal and idler in type I collinear OPA

Type I amplification in BiBO has a remarkable bandwidth but amplifies both signal and idler in the same polarisation. If the amplification geometry is fully collinear with a collimated pump, the two beams are undistinguishable except for the wavelength range. Separating both beams is important due to the fact that only the idler is CEP-stable,

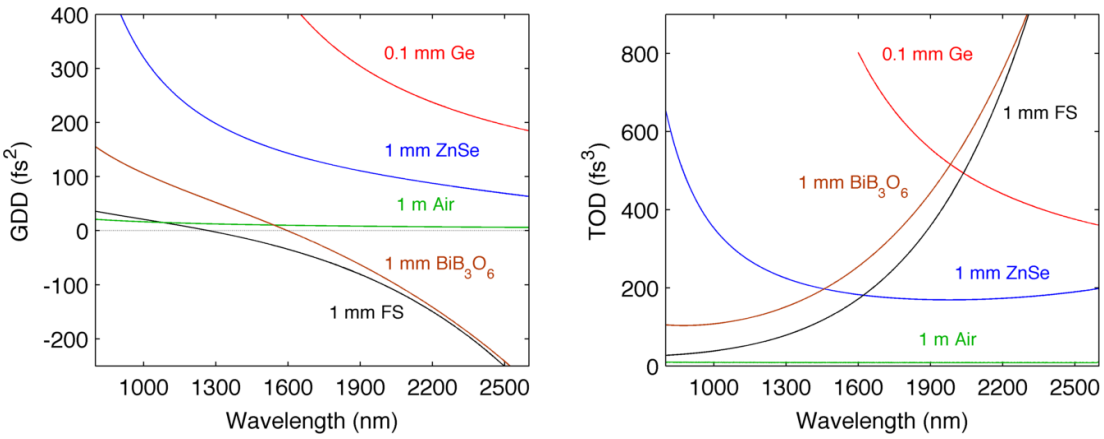

Figure 3.4: GDD and TOD values accumulated after propagation through several thickness of various optical materials relevant to this work. Note the absence of materials with negative TOD. Data from: Germanium [119], ZnSe [120], Air [121], BiBO [122], Fused Silica [123].

hence the presence of even a small amount of signal in the output beam would generate an unstable waveform from shot-to-shot. In the first iterations of the system a mix of thin germanium filters (high absorption < 1.6 μm) and dichroic filters was used. Germanium, despite performing well after the output of the DFG could not be used for the higher energy stages due to significant 2PA at higher intensities. The dichroic filters available leaked a small amount of radiation (<1%), but fortunately due to the dispersion present in the OPA chain this radiation did not arrive at the next OPA stage at the same time (i.e. did not interact with the pump), hence it only contributed to a pulse pedestal. In later designs a slight noncollinear angle was introduced, which allowed spatial separation of the beams, including with the pump. This simplified the design as now less pump, signal and idler separators were now needed, and it increased the bandwidth of the resulting idler, as the pulse was kept better compressed throughout the all amplification stages.

3.4 Results

The system was worked on from April 2010 to August 2013, where it went through several iterations, both due to different design, but also due to changes in the pump laser. Due to the imperfect design of the KM Labs Red Dragon system, specifically regarding beam profile quality, it was rebuilt in order to improve beam profile. The OPA system was also redesigned 3 times, with each taking into account the lessons learned from the previous iteration. In this section we present the 3 designs in chronological order.

3.4.1 3 Stage collinear OPA at 3 kHz - I

Seed

To create the 1.3 μm seed for the DFG stage, 2.7 μJ from the pump pulse are focussed with a parabolic reflector with f=10 cm onto a 2mm thick sapphire plate, with the long wavelength part of the generated supercontinuum (1.1 to 1.5 μm) containing 3 nJ of energy. The 2.7 μJ are measured after an iris, which is used to optimise the coupled energy and NA, such that the system runs immediately below the multifilamentation threshold, resulting in the maximum spectral density at higher wavelengths [54]. The spectrum of the SC after a 2 mm thick silicon filter (transmiting only above 1.05 μm) is represented in figure 3.5, as well as the spectrum of the Ti:Sa pump laser used across the WLG/OPA chain. Note that this supercontinuum is expected to extend into higher wavelengths than 1.5 μm, albeit with an exponentially decreasing intensity with increasing wavelength [54]. This allowed amplification up to 1.6 μm.

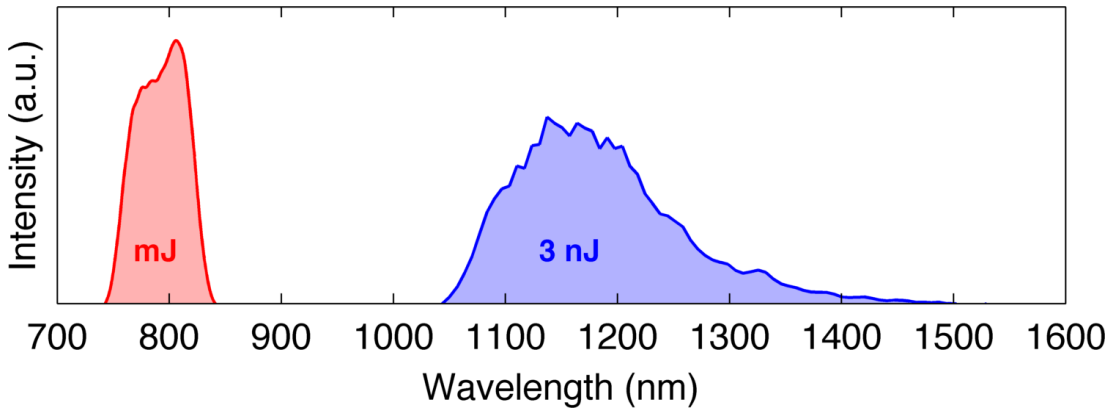

Figure 3.5: Red: spectrum of the Ti:Sa amplifier used in this work. Blue: 1.3 μm seed spectrum, generated through filamentation in sapphire. For this measurement the spectrum was filtered using a 2 mm thick silicon filter, effectively absorbing all radiation below 1050nm, allowing a measurement of the long wavelength tail with better signal to noise ratio. During further experiments the silicon filter was not used, as its dispersion was detrimental to performance.

DFG

The 1.1-1.6 μm seed was polarisation rotated using a periscope and then collinearly combined with 40 μJ of pump using a dichroic combiner, reflective for 800 nm (R>99%) and transmissive for the 1.1-2.7 μm range (T<5%). The substrate was 3 mm thick, which amounts to 4.2 mm propagation at the used 45 degrees incidence. Given that the zero dispersion wavelength of fused silica is at 1.3 μm the propagation of the pulse through the combiner will mostly accumulate TOD and will not significantly stretch the

pulse. The two collinearly-combined, perpendicularly-polarised beams are focused by a f=1 m concave silver mirror into an uncoated 1.5 mm long BiBO crystal cut at 11.3 degrees for Type I DFG between 800 nm and 1.3 μm. By doing in-focus amplification, pump beam profile irregularities could be ignored and high gain could be obtained over the whole beam, without the danger of hotspots decreasing the quality of the amplified beam. The collimation of the WLG seed was adjusted such that the waist was in the crystal plane by measuring the transmitted >1050 nm leak of a silicon filter with a silicon camera. An iris in the pump beam provided a way to fine-tune the pump intensity (as the crystal is in the focus), in order to tune the amplification to be just before saturation effects appear (which are easily detectable by monitoring the output spectrum), leading to a peak intensity of roughly 100 GW/cm^2. After propagation through the crystal, the amplified signal and generated idler contained 3.3 μJ of energy, where 1 μJ is in the idler. The spectrum of the amplified and generated radiation is represented in figure 3.6. Due to the extremely broadband seed and amplification bandwidth, both idler and signal overlap in the 1.6 μm spectral region. Spectral fringes dependent on CEP are washed out in figure 3.6 due to the long integration time used (10 ms at 3 kHz = 30 pulses). With a 1ms integration time small contrast unstable fringes were occasionally observable in a 50 nm region around 1.6 μm.

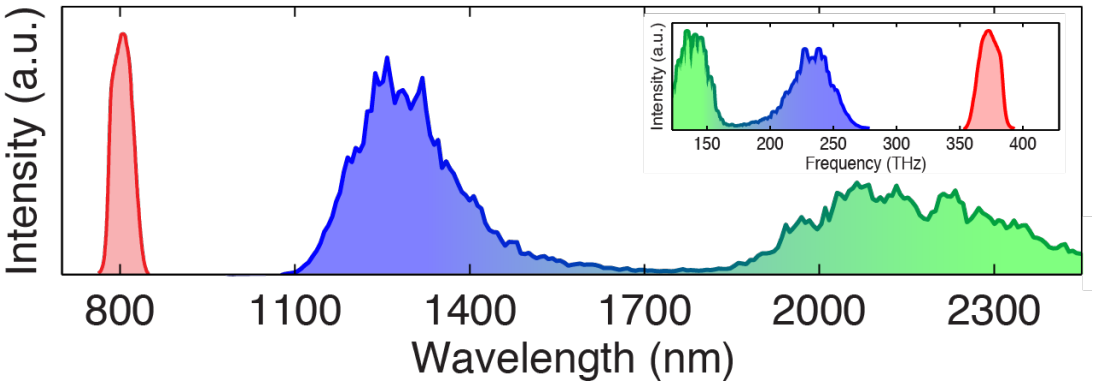

Figure 3.6: Pump (red), Signal (blue) and Idler (green) waves after the DFG in the wavelength domain, which exaggerates the bandwidth of the idler in comparison with the pump. Inset: Same data but in the frequency domain, revealing that the three waves have comparable bandwidth, hence support similar pulse durations.

To make sure there are no CEP unstable wavelength components in the final 2.1 μm pulse we used a 0.5 mm thick germanium filter at Brewster angle after the the crystal, such that all the radiation below 1.65 μm was rejected with high efficiency. The final spectrum is represented in figure 3.4.1). The 0.5 mm thick filter at 76 degrees amounted to 2 mm propagation through germanium, which introduces normal GVD. In order to assure the quality of the seed phase (i.e. suitable to generate few-cycle pulses) a pulse measurement was undertook. An homebuilt surface third harmonic

generation autocorrelator was used to measure the pulse duration. A 3 mm-thick fused silica lens was used to focus the pulse, both to assure high quality focusing as well as introducing anomalous GVD to compensate the effect of the germanium plate. The measured autocorrelation trace (figure 3.4.1 b)) matched the one calculated from the measured spectrum when adding 55 fs^2 of GVD, resulting in a pulse with roughly 22 fs of intensity FWHM.

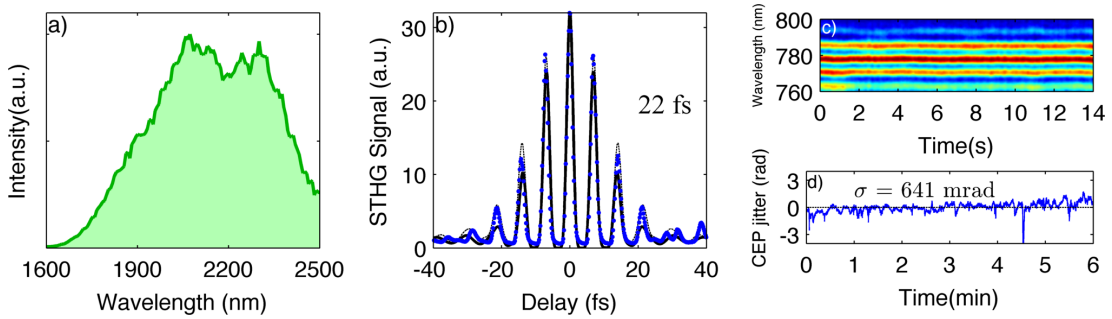

Figure 3.7: Pulse characterised after OPA1. (a) Spectrum after filtering with a 0.5mm Germanium filter (high absorption below 1600nm) (b) Surface third harmonic autocorrelation measurement of the output, compressed with a fused silica lens. Blue dots - measurement. Black line: THG autocorrelation corresponding to a transform limited pulse calculated from the measured spectrum (17 fs intensity FWHM). Dashed line: THG autocorrelation calculated from a pulse with 55 fs^2 of GDD which best matches the measured autocorrelation, corresponding to a 22 fs intensity FWHM pulse. (c) f-2f interference fringes, revealing a stable CEP. 14 second piece of the 6 minute f-2f measurement, revealing a stability of 124 mrad. (d) Calculated CEP jitter for the 6 minute CEP measurement, corresponding to a standard deviation of 641 mrad.

The CEP stability of the seed was also verified (figure c)). An f-2f interferometer was used to monitor the CEP of the pulses, where filamentation in YAG was used to generate the octave spanning continuum. In order to confirm the f-2f nature of the observed fringe pattern, the delay between pump and seed was sinusoidally perturbed, which modulated the generated idler CEP. With the perturbation off, the obtained fringe pattern was monitored over a period of 6 minutes, which yielded a 500 mrad CEP jitter, calculated using FTSI methods [124]. The nature of the observed CEP noise was mostly 1/f: the shorter the observation time, the better the CEP stability - for 14 seconds we observed a best jitter of 124 mrad; for 7 seconds, 87 mrad (figure 3.4.1 c). This indicates that an active, slow CEP feedback loop would be able to correct for the observed fluctuations (as will be verified in the next section). The integration time used was 4 ms, hardware limited by the spectrometer used (HR4000). This accumulates 20 shots per acquisition, which assuming the CEP noise is all at frequencies above 250 Hz would result in a stability 4x worse ($\propto \sqrt{N}$). Given the environmental, 1/f nature of the observed CEP noise, we hypothesise this is not the case. The sources of this CEP noise

can be a mix of factors. Given the Mach-Zehnder nature of the interferometer between seed and pump, with beam paths of the order of 30 cm, environmental fluctuations can give rise to interferometric path differences between the pulses which will slowly change the CEP. Additionally, supercontinuum generation at 800 nm in sapphire has been measured to have an intensity to phase coupling with a slope of approximately 140 mrad per % variation of the pump intensity [63]. Given that the seed laser had a long term pk-to-pk variation of 1.5%, we can expect that at least 210 mrad are due to the seed CEP variation in relation to the pump. Intensity to phase coupling can also occur during OPA due to cross phase modulation between the intense pump and generated idler. Additionally, the same process can also occur in the supercontinuum stage of the f-2f interferometer, possibly increasing the measured value. Despite that, the slow nature of the observed CEP fluctuations is promising, as they can be compensated by introducing a slow feedback loop [63].

OPA stages

The filtered idler output from the DFG is combined with 1.0 mJ of pump and sent to a second OPA stage, whereas the pump has 100 GW/cm^2 and the crystal 1 mm of thickness, cut at 11.3 degrees, which amplifies the idler to 20 μJ. The generated signal and remaining pump are then discarded using dichroic filters, and the transmitted idler sent to the next OPA stage. The third OPA stage was pumped with 4.4 mJ, at 100 GW/cm^2, and employed a 0.6 mm thick crystal at 11.3 degrees. A thicker crystal was not available at the time for this experiment. The resulting idler energy, after filtering pump and signal was 165 μJ when OPA stages were tuned for energy, where the spectrum was able to support 20 fs pulses. When adjusting the OPA stages for bandwidth, a spectrum capable of supporting 17 fs with 145 μJ of energy was obtained. Temporal characterization of the output using STHG autocorrelation revealed a pulse duration far from TL - 38 fs, estimated by considering a pulse with 100 fs^2, which gave the best fit to the central part of the autocorrelation. Compression improvement with dispersive materials was not attempted at this point. Due to the beam profile of the pump laser the resulting beam had several hotspots, and it was unknown whether the low achieved conversion efficiencies were due to the beam profile issues. The decision to improve the pump laser, instead of further optimising OPA design was then made at this time.

3.4.2 3 Stage collinear OPA at 3 kHz - II

The new design is represented in figure 3.9. The available pump laser was capable of supplying 6 mJ, 35 fs pulse at 3 kHz with a smooth beam profile. Taking into account what was learned while building the first design of the system, several changes were done:

- The in-focus design of OPA1 worked reliably in the previous iteration and was kept, but in order to get more energy transferred to the idler a shorter crystal was used (0.6 mm), which enabled us to pump with much higher intensities for the

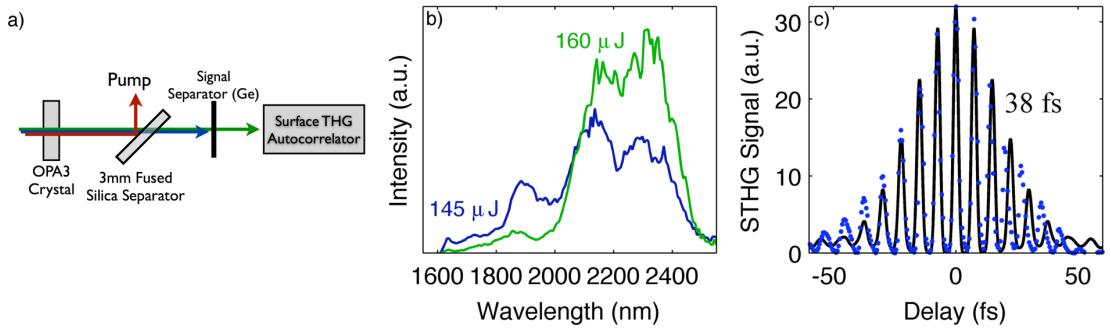

Figure 3.8: Pulse characterised after OPA3. (a) Schematic of the 3 wave separation and pulse measurement setup. (b) Spectrum after OPA3, measured for two different pump-seed tuning conditions; Green: optimised for maximum power, supporting 20 fs pulses; Blue: optimised for bandwidth, supporting 17 fs pulses. (c) STHG autocorrelation measurement of the pulse when tuned for maximum power; Blue: measurement; Black: Calculated THG autocorrelation calculated from the measured spectrum assuming the pulse has a residual phase of 100 fs^2 of GDD, corresponding to a 38 fs intensity FWHM.

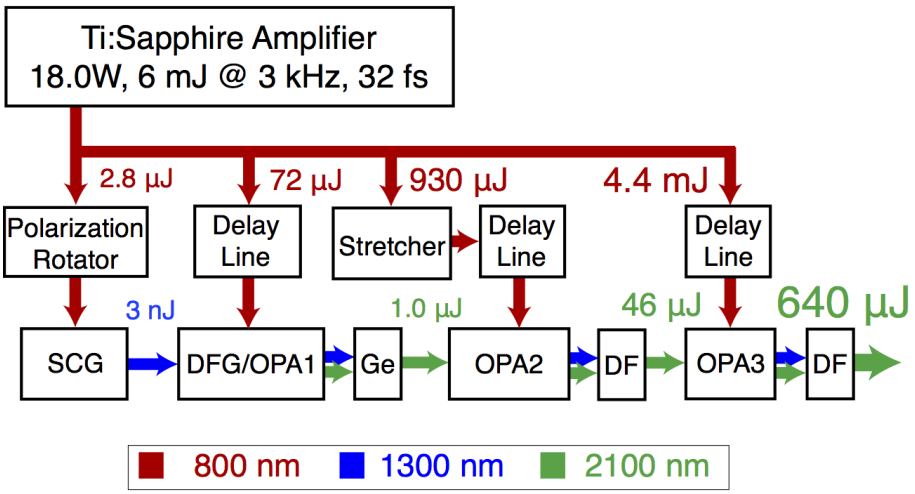

Figure 3.9: System design and energy results. SCG: supercontinuum generation stage (2mm Sapphire). Stretcher: 6mm SF56 window. Ge: 0.5 mm thick germanium wedge. DF: dielectric filters.

same beam profile before reaching saturation (400 GW/cm^2), hence making the seed interact with more energy (72 μJ). This lead to an increase in output energy and an idler energy of 1 μJ after filtering, with virtually the same spectrum.

- The second OPA now used a 1.5 mm crystal and the third a 1 mm thick crystal. Efficiency was improved - OPA2, pumped with 930 μJ at 61 GW/cm^2, amplified the seed to 46 μJ, and OPA3, pumped with 4.4 mJ at 100 GW/cm^2 amplified it to 640 μJ.

- We have found that due to the high GVD imparted by the germanium filter the pulse was positively stretched in OPA2 and was much longer than the pump. A measurement of the amplified bandwidth in function of pump delay is represented in figure 3.14 a). In order to keep the bandwidth we have stretched the pump pulse of OPA2 to 200 fs using a 6mm SF56 window. The gain bandwidth of OPA3 in function of pump delay is represented in figure 3.14 b) - one can see that it is mostly limited by the residual TOD of the amplifier chain - the anomalous dispersive propagation through the combiners and filters compensated the normal GVD of the germanium, but positive TOD accumulated. The final spectrum had a transform limit intensity FWHM duration of 28 fs (fig. 3.11), which corresponds to 4 cycles at 2.1 μm, which contrasts with the 18 fs potentially attainable with the spectrum generated in OPA1/DFG.

At the output, after pump and signal rejection the system produced 640 μJ of radiation at 2.1 μm with the spectrum represented in figure 3.11. The pulse duration was measured this time using an homebuilt SD-FROG [125], by slightly altering the setup described in [126]. The nonlinear signal was produced in a 1 mm thick piece of Sapphire. The measured pulse had 64 fs duration (Fig 3.12) due to residual anomalous dispersion. Given that the measurement of amplification bandwidth at OPA3 indicated that the pulse had no noticeable GVD at that point, we conclude that this anomalous GVD was introduced mostly due to the pump and signal separators, which amounted to 4 mm FS propagation. By introducing an extra 5 mm ZnSe plate, which has normal dispersion, we managed to recompress the pulse down to 42 fs (fig 3.12), where the difference with TL (28 fs) is due to uncompensated higher order dispersion.

The system had a power stability of 1.5% RMS over 10 minutes, measured with a power meter (Ophir Nova 2). CEP stability at the output of the system was also verified: by employing an f-2f interferometer similar to the one described in the last section, a CEP jitter of 410 mrad over 10 minutes. The difference with the results from the last section is possibly due to better pump laser stability. Given that the observed CEP jitter is again mostly at low frequencies, we have implemented a slow feedback system to correct for these slow drifts. A custom program written in C calculated the CEP from each measured spectrum, with 4 ms integration time/12 shots and through a PI algorithm calculated a feedback perturbation, which was applied to a piezoelectric actuator that increased the DFG pump-seed delay by an interferometric amount. Each iteration took 20 ms to execute, limited by the spectrometer minimum data transfer

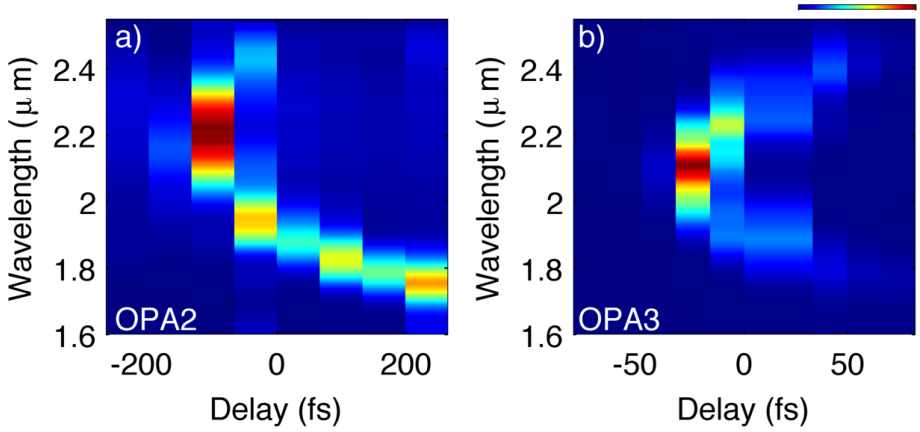

Figure 3.10: Amplified bandwidth after OPAs 2 and 3 in function of seed-pump delay, effectively serving as an XFROG measurement. a) OPA2 output spectrum in the idler in function of pump-seed delay without the SF57 stretcher in OPA2 delay line. The long tail at lower wavelengths and quadratic feature at higher ones reveals a mix of second and third order dispersion in the seed pulse, imparted by the germanium filter. b) OPA3 output spectrum, with the pump of OPA2 blocked. The residual quadratic shape reveals strong residual third order dispersion, and suggests that the positive GVD of the germanium filter was compensated by dispersive propagation through the fused silica dichroic elements between both OPAs.

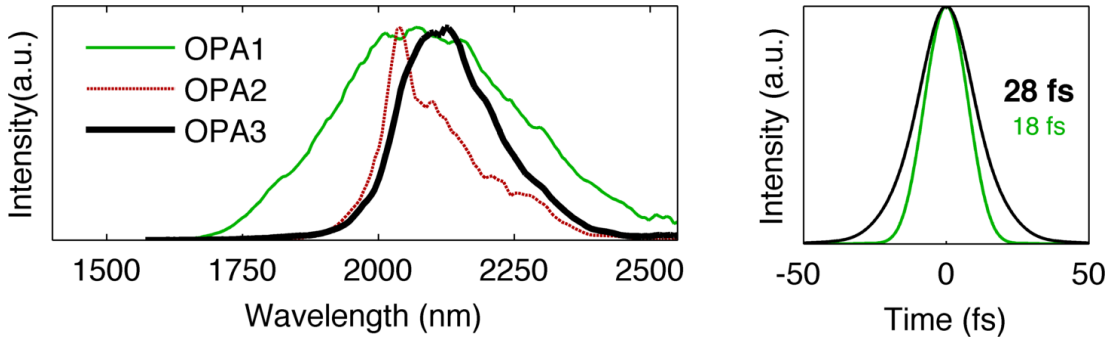

Figure 3.11: Filtered output spectrum after each stage. Due to dispersive propagation between the stages there is significant gain narrowing in OPA2. Right: Fourier transform limit comparison between the pulse after OPA1 (green) and at the end of the amplification chain (OPA3).

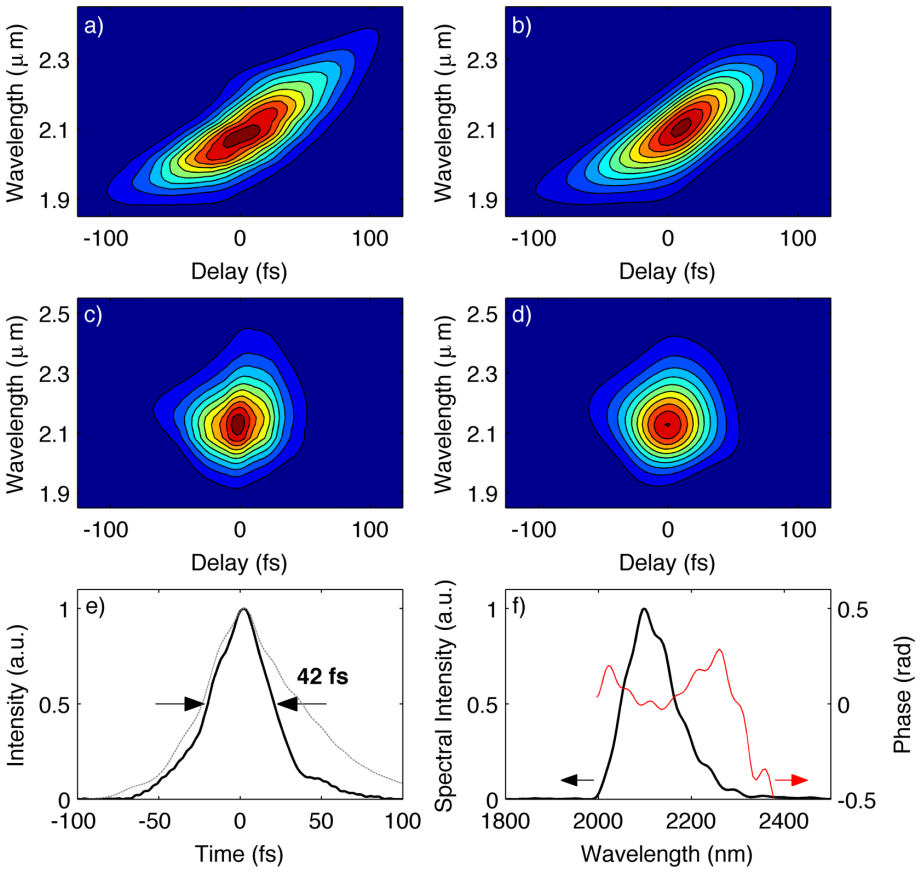

Figure 3.12: Temporal pulse measurement of the output of the system using SD-FROG. a) At the output, measured FROG trace. b) Retrieved trace, corresponding to a 64 fs pulse. c) Measured FROG trace after propagation through 5 mm of ZnSe. d) Retrieved trace, corresponding to a 42 fs pulse. e) Temporal profile of the retrieved pulses at the output (dotted line) and after recompression (solid line). e) Retrieved spectrum (black line) and phase (red line) for the compressed case.

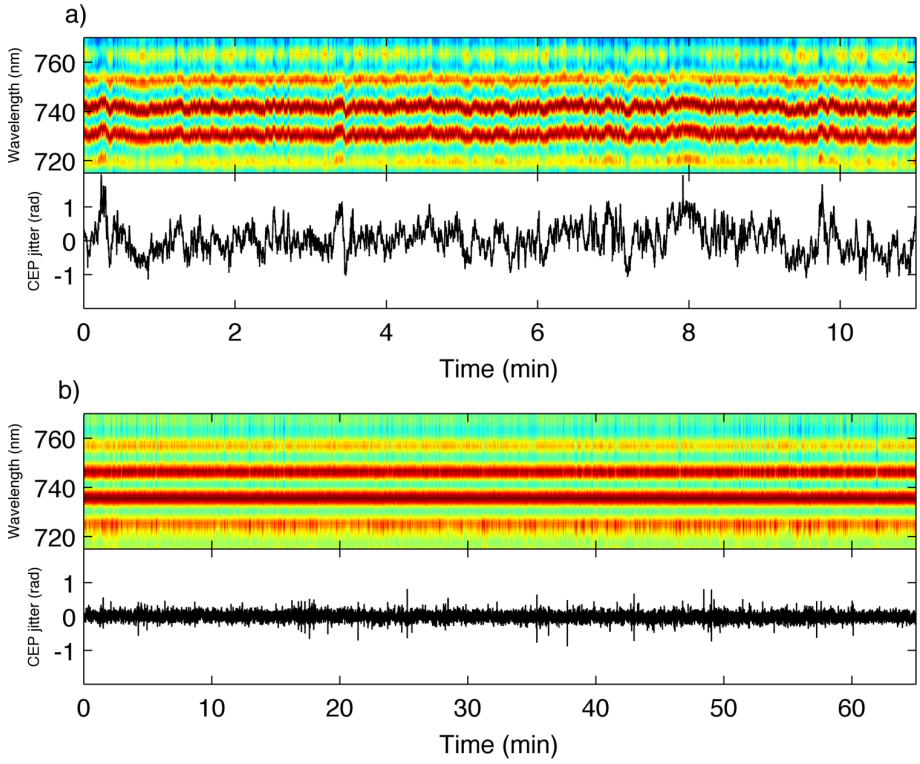

Figure 3.13: Long term CEP measurements with and without feedback. a) Open-loop 11 minute long measurement revealing a CEP jitter of 410 mrad. b) Closed-loop measurement revealing a CEP stability of 80 mrad over more than one hour.

time, limiting the bandwidth of the feedback loop to 50 Hz. With this, the slow CEP drift was eliminated, resulting in a stability of 80 mrad over 1 hour (figure 3.14).

3.4.3 Noncollinear OPA at 3/4 kHz

In order to solve the gain narrowing problem that the propagation of the seed through dispersive media provoked we have resorted mainly to two design changes:

1. DFG allows us to use travelling wave amplification - OPA does not, i.e. by delaying the DFG process to the last crystal, the pulse duration of the seeding wave is less determinant, as the bandwidth/pulse duration of the pump would be transferred to the generated idler. Hence the DFG was now deferred till OPA3, where OPA1 and OPA2 were used to amplify the signal at 1.3 μm. This wavelength is also less susceptible to the dispersion of the dichroic combiners/separators, whose substrate is made out of fused silica (which has zero GDD at 1.3 μm).

2. A slight noncollinear angle was used in OPA1 and 2 (<1 degree), which allowed the pump, signal and idler beams to be separated geometrically. This reduced the

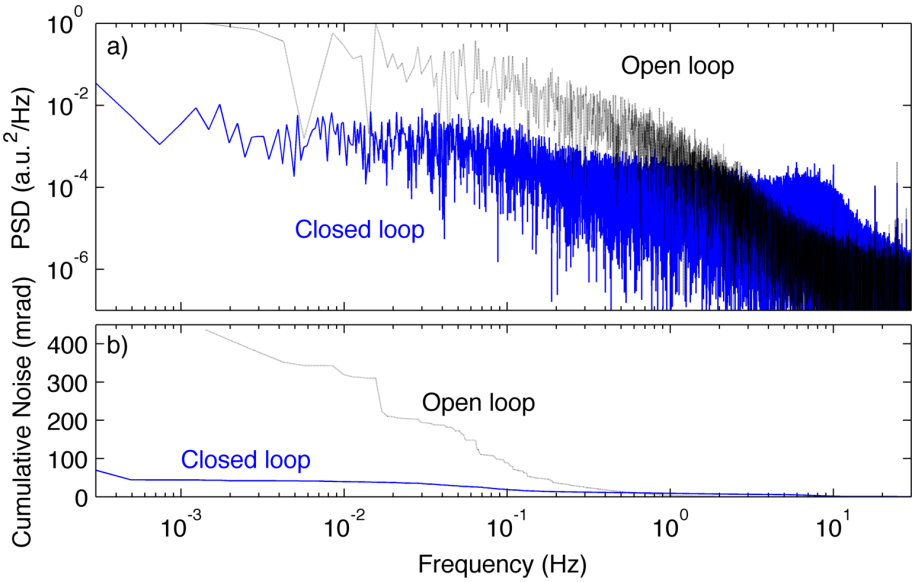

Figure 3.14: Frequency analysis of the CEP measurements in figure 3.14. a) Normalized power spectral density of both open and closed loop measurements. The feedback loop was able to compensate most of the low frequency noise, albeit introducing residual noise at higher frequencies. b) Cumulative noise of both measurements, resulting in 410 mrad for the open-loop measurement, and 80 mrad for the 60 minute measurement.

number of dichroics that were needed between OPA stages, greatly reducing the dispersion imparted in the seed/signal pulse up to the last OPA, and increasing efficiency and generated bandwidth at the expense of compactness.

With this scheme we were able to generate an idler with a spectrum similar to the one from the DFG in the previous system, i.e. supporting a < 3 cycle pulse. Additionally, the WLG stage was upgraded to employ a 3mm YAG plate instead of the 2mm Sapphire, which leads to a higher seed energy at 1.3 μm (as demonstrated in [54]). A schematic of the system layout is represented in figure 3.15.

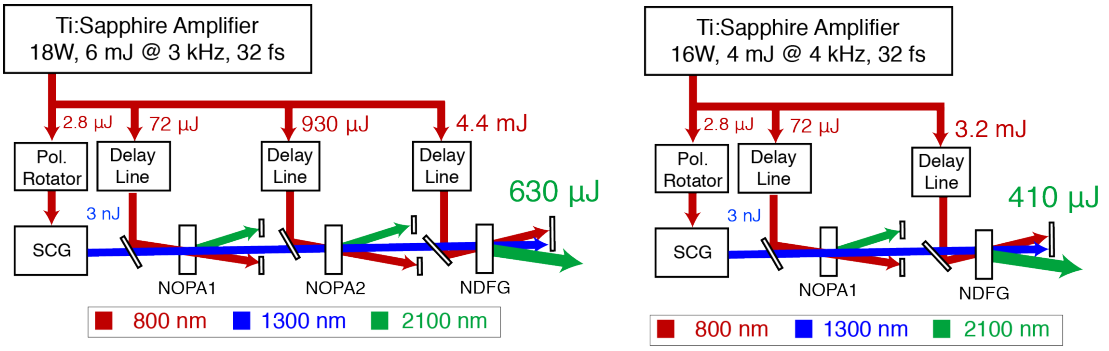

Figure 3.15: Block diagram schematics of the NOPA systems working at 3 kHz (left) and later 4 kHz. (right). SCG - Supercontinuum Generation.

For the 3 kHz pump OPA system (Fig 3.15a) the pumping energies and intensities were the same as in the COPA from section 4.2, the only changes being realignment and removal of the filters between OPAs, as well as the pump stretched in pump 2. This yielded virtually the same output energy at 2μm with a broader spectrum. Later, with the 4 kHz pump, the second OPA was found unnecessary - by removing all optics except steering mirrors between OPA1 and OPA3/DFG and decreasing pump 3 beam size to 5 mm, corresponding to 150 GW/cm^2, one greatly increased the gain in the final OPA/DFG without reducing total efficiency (the common concern with high gain stages is the usually lower efficiency when compared to low gain/power amplifiers, hence one would want the final amplifier to have relatively low gain. This was not an issue in this case, even with an energy gain of >100). The spectra obtained at the exit of the system, are represented in figure 3.16, for both signal and idler waves, in each case OPA1 and DFG delays were optimised for maximum power in the respective wave. The resulting spectra are sufficient for sub-2-cycle pulse generation at 1.3 and 2.2 μm, when coupled with adequate dispersion compensation.

One limitation of non-collinear DFG is that the generated pulse has pulse front tilt, which might be a limitation for applications. This can be mitigated by minimising the pump-seed angle. Still, even for small angles, the effect can be detrimental over large bandwidths. In order to verify if the imparted pulse front tilt would be a limitation for HHG we have measured the spatio-spectral profile in focus by scanning a 10 μm slit

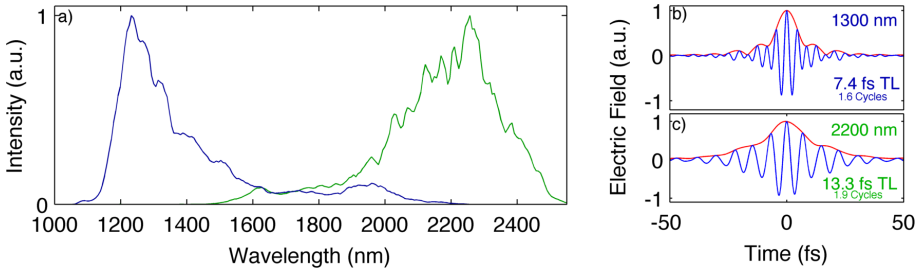

Figure 3.16: Spectral and supported durations for the NOPA configuration. a)Spectrum at the output of the system for signal (blue) and idler (green), when OPA1 and DFG are optimised for power in the respective wave. b) Fourier transform limit of the generated signal, supporting a 7.4 fs pulse (1.6 cycles at 1.3 μm) c) Fourier transform limit of the generated signal, supporting a 13.3 fs pulse (1.9 cycles at 2.2 μm)

across the focus of the beam (f=10 cm) and measuring the transmitted spectrum. A significant pulse front tilt would result in a change in central wavelength across focus [127]. The scanning direction was along the plane defined by the noncollinear angles between beams in the NOPA, i.e. where one would expect spatial-chirp from the noncollinear interaction. The results of our measurement are represented in Fig 3.16. A residual quadratic dependency of the spatio-spectral shape was found (Fig 3.16b), meaning that one side of the focused beam has more 'centre' frequencies, while the other edge has low and high frequencies. Additionally, the faint components below 1.7 μm were found to have a larger beam-size than the rest of the spectrum. Besides these features, all frequencies are present across the intense part of the beam, without any strong spatio-temporal couplings.

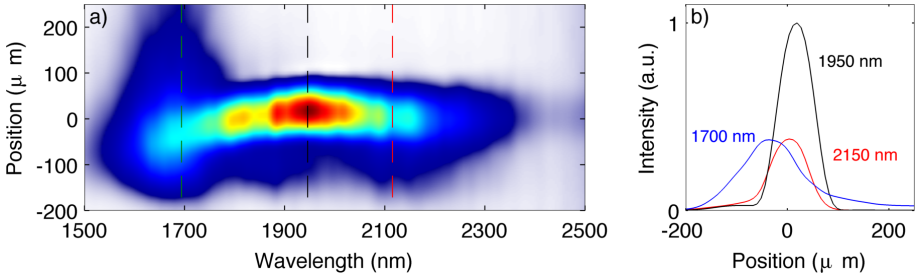

Figure 3.17: Measurement of spatio-spectral profile in focus for the NOPA configuration, exhibiting a residual variation of center wavelength across the intense part of the beam. a) Spatio-spectral profile. b) Three line outs across the dashed lines of a), for 3 different wavelengths.

Regarding temporal compression, our previous experience and understanding of OPA performance led us to believe that we are able to achieve sub-30 fs pulses with this setup.

The experiments of section 5.2 and 5.3 were prioritised over an effort to measure such pulses. For the HHG experiments the dispersion between the DFG crystal and the gas target was reduced to only 4 m of air and a 1 mm fused silica window. For the spectrum in figure 15 (green), which supports a 13.3 fs TL pulse, this residual phase would result in a 20 fs pulse, which for a 25 μm spot size would correspond to $>3 \times 10^{14}$ W/cm^2, enough for a >300 eV HHG cutoff in neon, which reaches the water window. Due to the availability of an HCF setup setup and reports on nonlinear pulse compression that impart a phase opposite of propagation in bulk materials [106], we have attempted nonlinear broadening in a 250 μm core, 70 cm long hollow core fiber, in a 1.5 bar Xe chamber. The overall throughput was 40% (375 in, 150 μJ out) and the output spectrum covered more than an octave, but attempts at compression using a pair of fused silica wedges proved unsuccessful - by observing the third harmonic of the signal, one could only decrease its intensity by increasing wedge insertion. The lack of a maximum of THG intensity suggests that an optimum compression point was possibly not reached. Additionally, theoretical work suggests that for 2.0 μm, the nonlinear phase is only able to compensate for 1-2 mm of fused silica [128], which is given by the output window of the HCF chamber plus the minimum insertion of the wedges. Given this uncertainty, the low throughput and priority of the HHG experiments further work reverted to using the OPA output. Given the coherent nature of the broadening process it is feasible to assume that with adequate dispersion compensation one could compress the spectrum in Fig 3.18 to near-TL duration, which corresponds to a 0.8 cycle pulse at 1.93 μm (inset, fig 3.18).

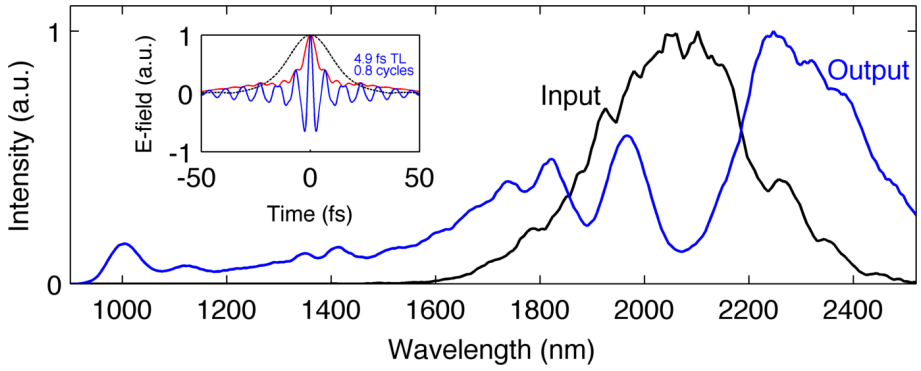

Figure 3.18: Spectral broadening through hollow-core fiber compression. Black: input spectrum for the HCF. Blue: Spectrum after propagation through a 70 cm long, 250 μm core HCF filled with 1.5 bar Xe with 40% transmission. Inset: Fourier transform limit of the spectrum represented in blue, supporting a 0.8 cycle pulse at 1.93 μm.

3.5 Applications

3.5.1 HHG in Xenon

During the development of this source we have tested it using high harmonic generation. Light sources with longer electric field periods lead to higher ponderomotive energies of the recolliding wave packet in HHG, which translates in the emission of higher energy photons. During the development of the system described in section 3.4.2 an attempt at verifying this was done. As it was a first experiment with HHG with this source, we used Xenon as the target gas, which generally leads to a higher single atom response due to the higher ionisation rate, hence possibly a stronger, easier to detect signal. Phase-matched HHG in Xenon and Argon with 800 nm pulses is typically limited to 40-50 eV due to the low saturation intensity of the medium [129], i.e. the higher intensities needed to reach higher cutoffs would result in excessive ionisation of the medium (for the same pulse duration). The setup for our experiment is represented in figure 3.19. At this time the OPA system was able to output 320 μJ pulses, of which only 150 μJ were delivered into the HHG target. The beam was focused by an f=10 cm CaF_2 lens into a through-hole, 0.5 mm long effusive target, filled with Xenon at a backing pressure of 200 mbar, where HHG took place. The fundamental beam is then filtered out by a 100 nm Aluminum thin foil, and spectrally dispersed in a XUV spectrometer composed of a free-standing transmission grating and a peltier-cooled XUV CCD. The measured spectrum, corresponding to a 60 s integration, is represented in figure 3.18. HHG up to above the Aluminium edge at 72.8 eV is observed. The high harmonic nature of the signal is clear at lower wavelengths, but harmonic contrast starts to decrease with increasing photon energy, possibly due to the lower resolution of the spectrometer at these energies. An HHG cutoff at 75 eV driven by a 2.1 μm source would correspond to a peak intensity of $5\times\ 10^{13}$ W/cm^2.

3.5.2 HHG in Argon

A study of HHG in argon was done using the same setup as fig 18, but with a spectrometer based on a grazing incidence flat-field grating, capable of studying the 50-200 eV spectral region. Pulses with 300 μJ from the 4 kHz NOPA (spectrum represented in fig 3.16, green) were focused using an f=10 cm silver mirror at low angle to minimize astigmatism into a 0.5 mm thick gas target with 0.5 mm thick walls. The target was connected to a gas regulator supplying argon gas at a chosen pressure, in this case corresponding to 0.7 bar of backing pressure. The residual fundamental co-propagating with the HH radiation generated on target is filtered out by a 200 nm Zr filter, which has high transmission (>50 %) between 90 eV and 190 eV. The HH radiation is then sent into a homebuilt flat-field X-ray spectrometer, whose detection device is a peltier-cooled CCD camera. A typical HHG spectrum is represented in fig 3.20a. A normalized spectrum generated with a 1 mJ, 40 fs pulse from a Ti:Sa amplifier (800nm) in neon with the same setup and similar focusing conditions is represented for comparison. Despite the higher ionisation potential of neon compared to argon and a lower pulse energy at 2

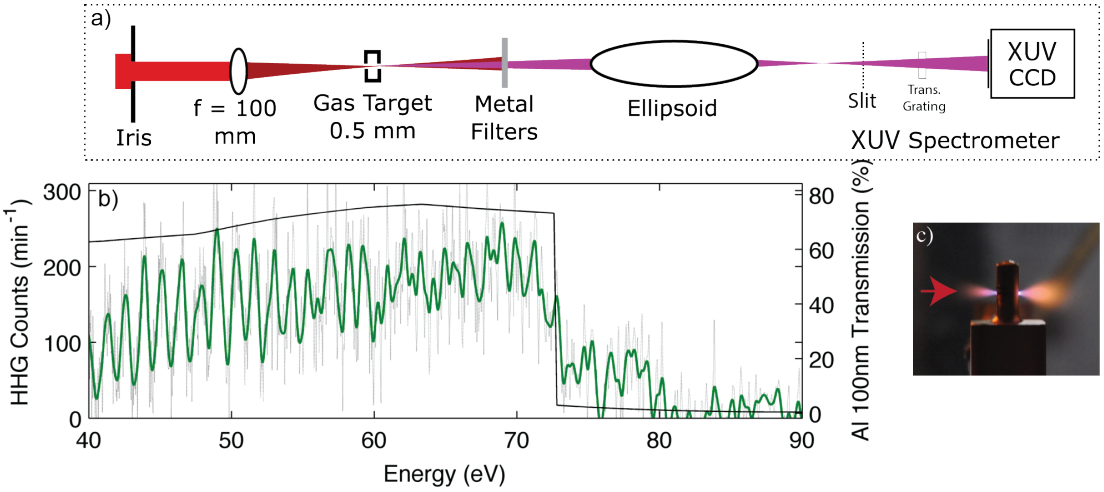

Figure 3.19: Application of the OPA source to HHG in Xe, generating radiation up to the Al L-edge at 72 eV, corresponding to an intensity exceeding $5\times\ 10^{13}$ W/cm^2. a) Experimental Setup. Trans. Grating: Free-standing transmission grating. b) Gray: measured HHG spectrum in 200 mrad of Xe. Green: Signal after fourier filtering, to better illustrate the harmonic periodicity of 0.6 eV. c) Photo of the target during the measurement. Laser propagates from left to right.

μm compared to 800 nm, the 2 μm generated spectrum reaches a higher cutoff (180 eV) due to the ponderomotive scaling nature of HHG [129]. Still, the flux at lower photon energies is still higher for the 800 nm case, possibly resulting from the higher microscopic response or higher input energy. Regardless, a systematic study is needed over a range of parameters to make a proper comparison in terms of yield.

3.6 Further work and conclusion

Despite not achieving the initial objective of generating HH radiation in the water window with this source, several demonstrations were done in this chapter, such as a compact 2-stage, WL-seeded NOPA, capable of generating spectra for <2 cycle pulses with energies not far from a millijoule. There are several possibilities for further work. Scalability of the output energy of this scheme only depends mostly on the pump laser - crystal apertures up to 25 mm are available commercially [130], hence at 200 GW/cm^2 one could use 50 mJ of pump energy, and possibly extract 5 mJ (considering typical efficiencies for the system built in this chapter). Introducing an OPCPA scheme might be advantageous, as the reported damage limits for BiBO under picosecond regime approach 48 GW/cm^2[131] at 56 ps at a similar wavelength (1064nm), which amounts to a maximum pump of 500 J if using a 1 cm^2 crystal at 10 GW/cm^2, 50 ps. Whether it is possible to have sufficient gain using such parameters is yet to be proven.

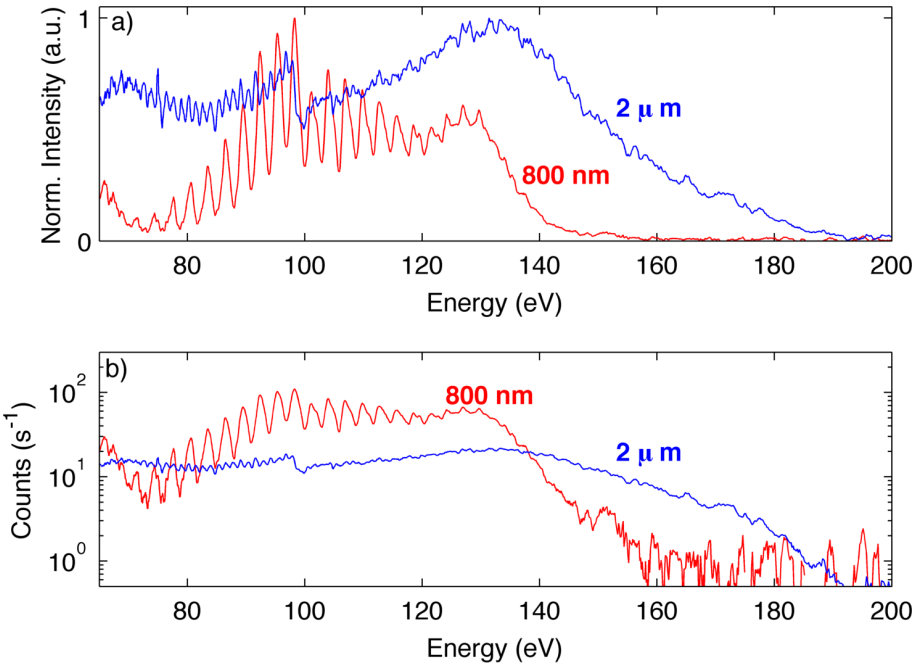

Figure 3.20: Application of the OPA source to HHG in Argon, and comparison with HHG in neon with a 1 mJ, 40 fs, 800 nm pulse. a) Normalized spectrum. b) Comparison of counts per second per pixel on camera for the two measurements.

However, moving into an OPCPA design introduces more additional design constraints and subsystems. Also, extraction efficiency of OPCPAs is typically lower than OPA systems. Another possibility for further scaling, either in energy or bandwidth, another interesting approach is a FOPA design [77] - by placing the OPA stage in the fourier plane of a 4-f shaper, due to the spectral separation the seed will locally have a long pulse duration, which is advantageous for pumping with longer, high energy picosecond pump pulses. Also, it opens the possibility of using different crystals, cut for different spectral regions, which can allow both power and bandwidth scalability. The complexity of this scheme is however much higher than typical OPAs.

If phase-stable broadband output is desired, another interesting prospect is the one of pumping the COPA configuration with a CEP stable pump. This would generate a phase stable spectrum, resulting from the coherent combination of signal and idler, spanning from 1.1 to 2.5 μm Additional copropagating wavelengths in the VIS-NIR, generated in the WLG stage, could be amplified in a serial OPA, pumped by the SHG of 800 nm, a scheme which has been demonstrated to be able to support larger bandwidths in the VIS-NIR range [132], extending the total hypothetical bandwidth to 600-2.5 μm. Dispersion compensation and CEP, intensity and timing jitter between different parts of the spectrum would be the main issues to solve at this point.

Regarding dispersion compensation in the SWIR range, besides the arduous task of designing, building and testing a 4f pulse-shaper for the output beam, one could also introduce an AOPDF [133] in the system to programmatically change the phase of the output pulse. Given the low efficiency and maximum energy input of AOPDFs one would need to insert it between amplification stages and perhaps add an additional stage to compensate for the AOPDF losses. Additionally, the shaping window would be greatly reduced if further amplification stages used short pump pulses, as pre compensation of phase might lead to certain parts of the spectrum moving out of the narrow temporal gain window the short pump pulses provide. This added complexity suggests that an AOPDF-including design would be more flexible and realisable when designed as an OPCPA (such as in [98, 107]). Another practical point is that the price of this component is comparable to the rest of the OPA system presented in this chapter. Another option for dispersion compensation is chirped multilayer mirrors [134] which can accomodate octave-spanning bandwidths, e.g. in the VIS-NIR [135]. The design and fabrication of these optics is both time consuming and expensive, and results in a solution with limited degrees of freedom, hence it is only attractive to pursue in case of more common laser designs or when no other option is available. In summary, in this work we have designed and implemented a bandwidth and energy scalable optical parametric amplifier in the SWIR. Energies up to 640 μJ at 3 kHz or 400 μJ at 4 kHz with pulse durations of 42 fs or less at 2.1μm were obtained, and CEP stability was demonstrated (80 mrad over 1 hour). This source was applied to HHG in argon reaching a cutoff of 180 eV, which demonstrates ponderomotive scaling of HHG in relation to 800 nm sources. Further work is needed to achieve higher photon energies, specifically the so-called water window, at 282-543 eV, attainable by phase-matched HHG in neon or helium with 2 μm pump lasers [129] at intensities achievable with this source, estimated to reach 4x10^{14} W/cm^2 with

a 25 μm focus size.

Chapter 4

Simultaneous compression, characterisation and phase stabilisation of 1.4 cycle pulses at 740nm using a single dispersion scan setup

4.1 Introduction

High peak power laser pulses with single-cycle durations are increasingly sought after due to their potential for strong field physics [17] and ultrafast spectroscopy studies [136, 137]. Ironically, the correct measurement of these pulses is as much of a problem as their generation, since such broadband sources require a significant amount of optimization, which is unfeasible without reliable diagnostics. Without a sufficiently sensitive and precise measurement technique it is actually impossible to characterize the performance of the source. For the last 30 years significant work has been done in femtosecond pulse measurement, where reliable techniques were invented and studied. These have led to many significant advances in several fields, most notably in strong field physics, including the generation of attosecond pulses [84] and the observation of valence electron motion [138]. In the sub-1.5-cycle regime, techniques such as FROG [139], SPIDER [140, 141] and attosecond streaking [142] have been used to measure pulses down to 0.88 cycles in duration [23]. Despite their success, such techniques employ setups with numerous optical elements, often requiring interferometric beamsplitting and recombination (in the case of streaking the requirements are even higher - one needs a working attosecond beamline to provide the shorter temporal gate pulse). This complexity translates into additional alignment and calibration time, which reduces the usefulness of the technique. It is therefore interesting to investigate simpler, more straightforward ways to accomplish the same task. Recently, we demonstrated a new technique dubbed dispersion-scan (or d-

scan), whose experimental implementation is straightforward, only requiring the addition of a second-harmonic generation (SHG) stage with sufficient bandwidth to the standard chirped mirror compressor employed to manage dispersion throughout the experimental setup [143]. The principle behind d-scan is to monitor the generated SHG spectrum as a function of dispersion around the optimum compression point and using this information, together with a measurement of the pulse spectrum, to retrieve the spectral phase, thereby fully characterizing the pulse temporally. Furthermore, the retrieval algorithm is robust regarding bandwidth limitations in the nonlinear process used, eliminating the source of one of the most common systematic errors that plagues few-cycle pulse measurement [144]. To this date, d-scan has been demonstrated with few-cycle laser oscillators [145, 143, 146] and a high energy hollow-fiber compressor yielding 4.5 fs pulses [147].

In this work we demonstrate the feasibility to use d-scan in the sub-1.5-cycle regime by characterizing 1.4-cycle/3.2 fs pulses generated in a hollow fiber compressor, with dispersion compensation performed using state-of-the-art octave-spanning chirped mirrors. The setup was composed of the usual chirped mirror compressor with glass wedges for dispersion fine-tuning, plus a SHG stage to monitor the SHG spectrum of the pulse as a function of dispersion. This setup, besides being able to both compress and characterize the pulses temporally, also doubles as an f-2f interferometer [52] when the laser spectrum is octave-spanning. As such, we also demonstrate that one can use it to monitor and stabilize the CEP jitter of the pulses, achieving a stability of 140 mrad over 100 minutes. One difficulty encountered during this study concerns the limited flexibility of chirped mirror compressors - their phase is essentially fixed, except for the variable glass thickness introduced by the wedge pair. This allows one to optimize the pulse phase unidimensionally, and for the case where the compensated phase matches the nonlinear plus propagation phase perfectly, one achieves perfect compression for a certain glass thickness. For situations where the phase to be compensated for does not match the target phase of the chirped mirror compressor, one will still be able to have zero GDD at a certain wavelength but not across the whole spectrum, i.e., there might be a significant amount of higher order phase, most commonly TOD. When working with near-single cycle pulses this can affect the result greatly as an apparently small amount of TOD over a large spectrum can significantly increase the pulse duration, decrease the peak power and create satellite pulses. Hence it would be desirable to be able to tune the final TOD of the pulse without having to resort to a new set of chirped mirrors. One possible way to achieve this would be by changing the fine-tuning element (e.g., glass wedges) to a material with an exactly symmetric dispersion with respect to the rest of the experimental setup, which is not always possible, as there exists only a limited number of materials, each with its specific dispersion curve. In this work we found that in cases of excessive negative TOD in the VIS-NIR range one can exchange propagation through glass to propagation through water to increase the amount of positive TOD in the pulse, leading to considerably better performance in the case of our compressor. We have demonstrated a reduction of pulse duration from 3.8 to 3.2 fs, accompanied by a significant improvement in pulse contrast and peak intensity.

4.2 Experimental

4.2.1 Laser source

Our laser system is composed of a CPA Ti:Sapphire amplifier (Femtolasers FemtoPower Compact PRO CEP) seeded by pulses from a broadband few-cycle CEP-stabilized prism-less Ti:Sa oscillator (Femtolasers Rainbow) temporally stretched in bulk glass. The amplifier features a prism compressor and chirped mirrors for TOD precompensation before amplification, delivering 33 fs pulses (intensity FWHM) with up to 850 μJ at 1 kHz. While the spectrum of the amplifier is sufficient to support 24 fs pulses, there is significant uncompensated residual phase due to sub-optimal TOD precompensation and self-phase modulation in the prisms. We found this not to be a limiting factor regarding the generation of compressible octave-spanning spectra. The output from the amplifier is focused by a f = 1.5 m lens into a 1 m long, 250 μm core hollow fiber (HF) containing Argon at 1 atm of pressure. Spatial coupling into the fiber is optimized using an iris placed before the lens, transmitting roughly 400 μJ out of 580 μJ. After propagation through the fiber and output window, the beam contains 200 μJ, corresponding to 50% transmission, with a typical RMS power stability of 0.5% over 1 hour.

4.2.2 Dispersion scan

A schematic of the dispersion scan setup is represented in Fig. 4.1. The beam is collimated with an f = 1.25 m silver mirror and then sent through a pair of antireflection (AR) coated (650-1050 nm) 8 degree BK7 wedges that constitute the variable dispersion element of the d-scan setup, as well as the feedback element for the CEP slow-loop. These two tasks have different requirements, though: for d-scan one needs a fast stage (>5 mm/s) with coarse resolution (10 μm steps); for CEP feedback one needs a high-resolution stage with fast response time. We found that it is less expensive to have a different stage in each wedge, each optimized for a particular task. For d-scan we mounted one of the wedges in a linear motion guide coupled to a stepper motor using a trapezoidal leadscrew, encoded with a slide encoder with 140 μm resolution, which due to the small angle of the wedges results in a 20 μm glass insertion resolution. For CEP feedback we mounted the second wedge on a Newport AG-LS25 piezo motor driven stage, capable of fast, ripple-free, no backlash, high-precision motion. The beam is then compressed in a double-angle chirped mirror compressor (Ultrafast Innovations GmbH), designed to compensate propagation through 1 m of air and 1 mm of fused silica from 500 nm to 1050 nm for every 2 bounces. The reflectivity bandwidth of the mirrors extends down to 450 nm, exhibiting a sharp cutoff at this wavelength. After ten bounces, half at 5 degrees incidence angle and half at 19 degrees, a small percentage of the beam is reflected by a small angle wedge for the dispersion-scan measurement. The transmitted beam is free to be used in experiments, containing 160 μJ.

The central part of the reflected beam is blocked by a thin wire for later separation of the SHG and fundamental beams [146] and is then focused by a f = 250 mm concave silver mirror into a 5 μm thick BBO crystal cut for type-I SHG at 800 nm, generating

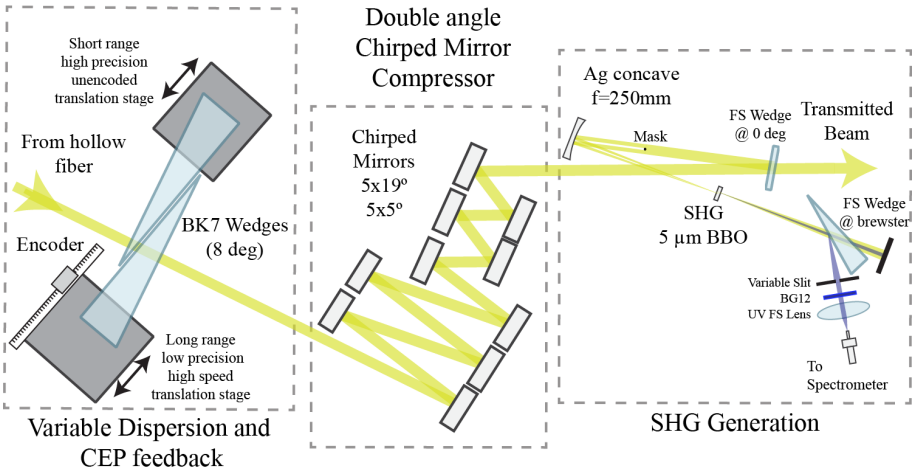

Figure 4.1: Schematic of the d-scan setup.

a broadband SHG signal in the s-polarization plane (this signal can in fact be seen as sum-frequency generation, SFG, resulting from the convolution of the fundamental spectrum with itself, whose shape and intensity strongly depends on the spectral phase [143]). To retain only this s-polarization signal, a reflection from an uncoated fused silica wedge oriented at Brewster's angle reflects 12% of s-polarization and a residual amount of p-polarization, effectively serving as a broadband polarizer. Most of the remaining fundamental is then cut by a variable slit and a BG12 filter is added to further improve rejection of the fundamental. The resulting beam is then coupled into a spectrometer (HR4000, Ocean Optics), intensity calibrated from 200 to 1100 nm by the manufacturer. By measuring the SHG/SFG spectrum as a function of BK7 propagation thickness, the experimental d-scan trace is recorded. The total BK7 range used for this study was 4.2 mm, corresponding to a total of 210 spectra at 20 μm steps. A complete trace is typically acquired in 10-30 seconds, depending on the integration time and stage speed used. The experimental trace, together with the measured fundamental spectrum, is used to retrieve the spectral phase using an algorithm based on the one described in [143, 146], although in the present study a different kind of bootstrap method was employed: 5 d-scan traces were measured successively and retrieved independently, and statistics were done on the 5 retrieved spectral phases. This way, the uncertainty will include the sensitivity of the algorithm to experimental noise. Each retrieval takes about 1 minute in a state-of-the art workstation. As discussed in [143, 146], a common problem when characterizing such broad spectra is the bandwidth of the nonlinear process employed. In fact, even the bandwidth of a 5 μm BBO crystal would be narrow for these pulses. Still, there is no need for calibration and marginals, since we can introduce a smooth response function in the retrieval, as discussed in [143], and the algorithm correctly converges to the correct phase and response function pair.

4.3 Experimental results

In the process of optimising our pulse compression setup we have encountered several challenges that prevented us from directly attaining the 1.4-cycle regime. In hindsight, these problems are easily identifiable just by glancing at the d-scan traces. In this section we will illustrate the steps we have taken to overcome them.

4.3.1 Hollow fiber compressor

A typical spectrum of the beam after the hollow fiber compressor and the chirped mirrors is shown in 4.2(a) (dashed line). At -10 dB, this spectrum spans from 450 nm to 1020 nm and supports a 2.9 fs pulse. Considering only the frequencies that the chirped mirror compressor can actually compress (500-1050 nm), it would support a 3.2 fs pulse. The repeatability of these parameters in day-to-day operation is surprisingly good: although the exact position and amplitude of the central peaks can change every time the fiber is realigned, the span and transform-limit of the spectrum is extremely consistent. As studied in a previous work, a wavelength dependence on mode size is present on the collimated beam (as expected from diffraction), which does not translate to spatio-temporal structure in the focus [147].

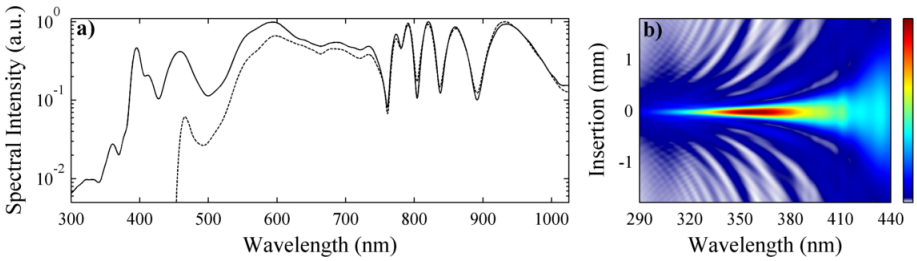

Figure 4.2: (a) Black line: Typical spectrum generated in the HF compressor, supporting a 1.9 fs pulse at 690 nm. Dashed line: Typical spectrum, after propagation through the wedges and the chirped mirrors, supporting a 2.9 fs pulse at 722 nm. (b) Theoretical d-scan trace calculated from the spectrum in (a) (dashed line) and assuming a flat spectral phase.

The calculated d-scan trace corresponding to a perfectly compensated spectral phase is given in Fig. 4.2(b), where we see that all frequencies in the main peak of the pulse are compressed for the same wedge insertion; the maximum of the SHG signal provides the reference (zero) wedge insertion. Any deviation from this horizontal, smooth, flat shape then corresponds to uncompensated spectral phase, where different parts of the spectrum will be compressed for different insertions, hence giving a different SHG/SFG signal.

4.3.2 Double-angle chirped mirror alignment

Double-angle chirped mirrors have the advantage over double-chirped mirror pairs that their manufacture requires only one coating-run [148], hence eliminating potential mismatches between independent batches. In contrast, they need to be used at two fixed incidence angles for which the corresponding GDD oscillations will have opposite phase and cancel each other out. If these two angles are not properly matched, residual oscillations can remain that will result in deficient compression, namely in a reduction of the peak intensity of the main pulse. As theoretically exemplified in [143], these oscillations show up as fringes in the dispersion-scan trace. In order to better distinguish the fringes from the actual chirped mirror compressor from those caused by the nonlinear phase introduced by propagation in the hollow core fiber, we resorted to using a source with a known smooth spectral phase, namely the few-cycle oscillator studied in [145, 143]. After an initial alignment of the chirped mirror compressor, where the angles were adjusted to within ±2 degrees, it was obvious from the fringes present in the d-scan traces that this precision was not enough (Fig. 4.3(a)). After a much more precise alignment we were able to reduce these fringes to a minimum (Fig. 4.3(b)).

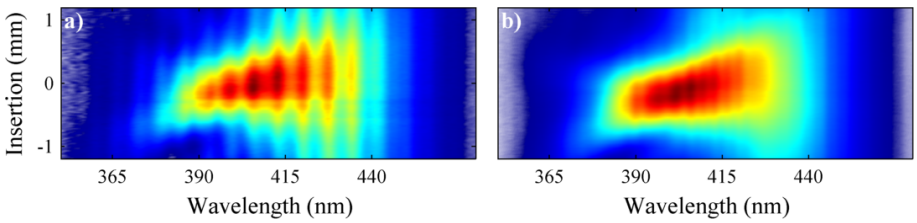

Figure 4.3: (a) Measured d-scan trace of a few-cycle laser oscillator with a smooth spectral phase, as used in [143], with mirror angles adjusted to within ±2 degrees. (b) The same measurement, after tweaking the chirped mirror angles to minimize residual phase oscillations.

4.3.3 Influence of the input phase

As thoroughly studied [149], the input phase into an hollow fiber compressor has a great influence on the output phase, hence the input phase has to be carefully optimized to yield the best compressible phase at the output of the spectral broadening stage. As theoretically demonstrated in [143], characteristic features in the d-scan trace have an explicit meaning: the vertical position of the trace (0th order) corresponds to GDD mismatch, i.e., if the trace moves for the same insertion range it means the GDD out of the hollow fiber has changed; a more pronounced tilt in the trace (1st order) corresponds to more TOD, and the sign of the tilt gives us the TOD signal; curvature in the trace corresponds to higher orders of dispersion; as explained in the last subsection, fringes in the d-scan trace correspond to very high orders of dispersion, i.e., phase oscillations. In the present work we have verified that the input phase of the hollow fiber compressor

has a strong nonlinear influence on the phase of the output pulse and has to be carefully optimized to achieve the flattest phase. In fact, as the input phase is varied using the amplifier prism compressor, the TOD affecting the output pulse goes through a minimum (Fig. 4.4), which in general we have found not to be correlated with the broadest achievable spectrum. Still, the optimization procedure for achieving the flattest possible phase is straightforward - by measuring successive d-scans for several prism insertions one can easily find the position that minimizes the observed tilt in the traces, i.e., that minimizes the output TOD, which is essential to have the best compression.

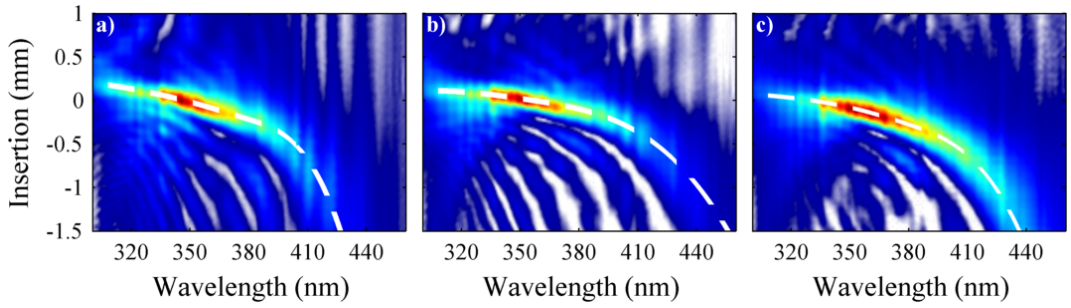

Figure 4.4: (a) to (c) d-scans for increasing prism insertion in the prism compressor. The tilt of the high intensity part of the trace goes through a minimum, as shown in (b), corresponding to minimum TOD and best overall compression.

4.3.4 Pulse compression

After optimizing the CPA compressor prism position for best compression after the hollow fiber we were, however, not able to achieve a pulse completely free of residual TOD. One can hypothesize that this is caused by at least one of three factors: 1) the phase of the chirped mirrors is not adequate for perfect compression of the hollow fiber output, possibly due to manufacturing limitations; 2) due to different parameters used in this work, the optimum output phase has a final TOD different than the one the chirped mirrors were designed for; 3) the control over higher dispersion orders in the Ti:Sa amplifier is insufficient for full optimization of the output phase of the HF compressor, i.e., there is no fine control over all orders, as changing the prism position changes GDD and TOD at the same time. A CPA system incorporating a pulse shaper would in principle be able to do such fine optimizations but was not available for this work. The duration of the compressed pulse is nevertheless sub-2-cycle, as shown experimentally in Fig. 4.5. The retrieved pulse has an intensity FWHM of 3.8 ± 0.1 fs, which corresponds to 1.6 cycles at 722 nm.

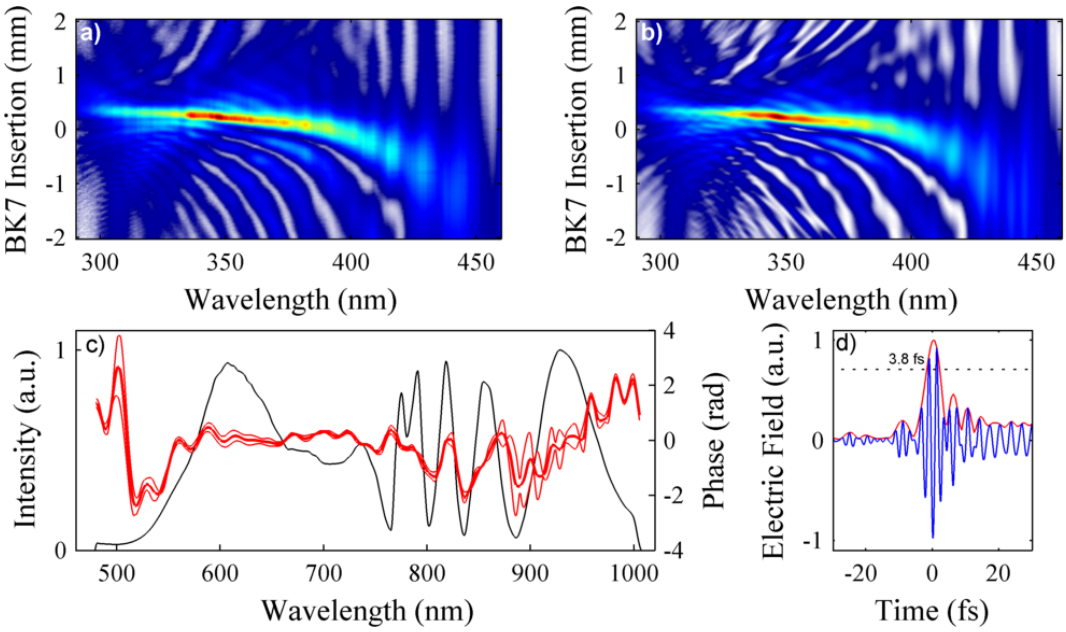

Figure 4.5: Representative measured (a) and retrieved (b) d-scans for the setup in Fig. 4.1. (c) Measured spectral intensity (black) and retrieved phase (thick red line, with the standard deviation indicated by thin red lines). (d) Retrieved electric field of the pulses for the BK7 wedge insertion that minimizes the intensity FWHM duration, corresponding to a 3.8 fs pulse.

4.3.5 Pulse compression optimization

Despite the achieved 1.6-cycle pulses, there is a significant difference between the transform-limited duration of the spectrum and the measured duration (from 2.9 fs to 3.8 fs, a 31% increase), mainly due to residual TOD (approximately -40 fs^3). Additionally, this TOD creates several post-pulses (Fig. 4.5(d)), which take a significant amount of energy away from the main pulse. Clearly, a small TOD adjustment would increase the peak intensity as well as shorten the pulse duration below the 1.5-cycle regime, both improvements greatly desirable for strong field physics experiments. The first possible solution to this problem would be to design and fabricate chirped mirrors with a more adequate phase. This is, however, costly and time consuming. Another possible solution is to replace the BK7 wedges with a material with the appropriate GVD/TOD ratio such that the output phase of the hollow fiber plus the material propagation is perfectly compensated for by the bounces in the chirped mirrors, but the universe of available materials is limited and that would not add the degree of freedom one needs to account for possible variations in the hollow fiber output phase. Hence, besides the BK7 wedges, one can add another material such that by controlling its thickness the right GVD/TOD ratio can be obtained. Since we need to add TOD for a certain value of GDD, this means this material must have a lower GVD/TOD ratio than BK7 ($<$1.3 fs^{-1}). In order to find such material one can search through GVD and TOD values available in the literature for transparent materials commonly available in optical laboratories (Fig. 4.6). Preferably, the choice should fall on common optical glasses or crystals, but those either have a similar or a higher GVD/TOD ratio than BK7. Air propagation also has a much higher ratio than BK7. Water, however, is ideal for this task, as it has a GVD/TOD ratio of 0.7 fs^{-1} [150]. This way, one only needs to add approximately 2.5 mm of water and remove 1.35 mm of BK7 to add the required 40 fs^3 of TOD for the same value of GDD. Equivalently, one can keep the same BK7 insertion and add more chirped mirror bounces.

This way, we added 4 more bounces off the chirped mirrors and used 4 mm of propagation through deionized water, which was the length of water that minimized the tilt in the trace. A typical resulting dispersion-scan trace is represented in Fig. 4.7, along with the retrieved scan and temporal and spectral analysis. We observe a clear increase in the quality of the compressed pulses compared to Fig. 4.5: shorter duration, higher intensity and reduced post-pulses. The retrieved pulse duration in these conditions was 3.2 $\pm$ 0.1 fs at a central wavelength of 722 nm, corresponding to a 1.4-cycle pulse. The relative intensity of the residual satellite pulses is reduced from 22% (Fig. 4.5(d)) to 10% (Fig 7(d) a 54% decrease.

4.3.6 Measurement bandwidth analysis

Due to the large bandwidth of these pulses it is important to assure that the bandwidth of the SHG/SFG crystal is sufficient to retrieve the phase over the whole spectrum. As noted in [143, 146], the SHG of pulses with broad spectrum needs to be analyzed as intra-pulse SFG: all frequencies mix with each other, as long as they are compressed. Hence the signal at e.g. 400 nm is not only due to the SHG of the components at

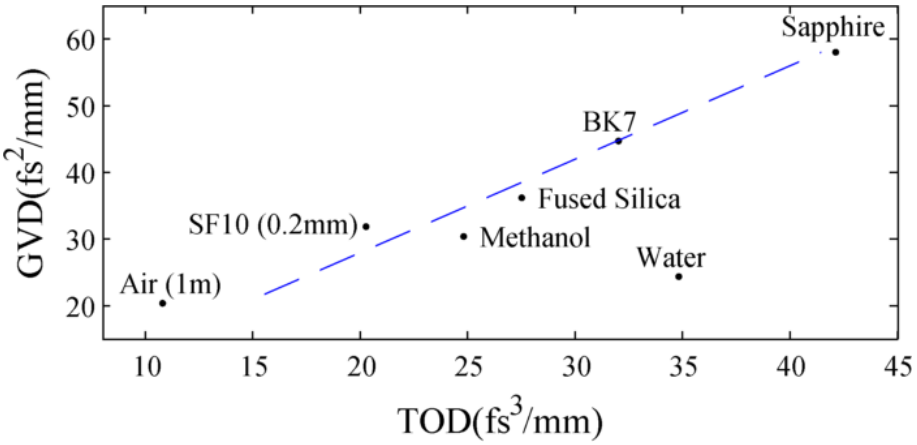

Figure 4.6: GVD and TOD values at 800 nm for materials commonly available in optical laboratories; values for water taken from [150]. The GVD/TOD ratio of BK7 is represented by the blue dashed line.

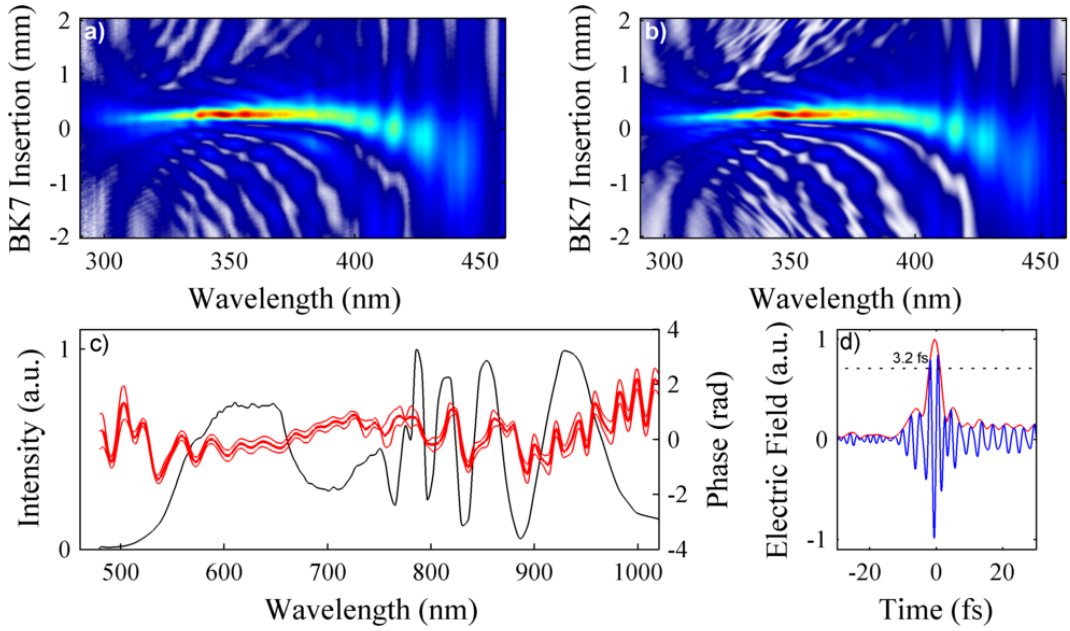

Figure 4.7: Measured (a) and retrieved (b) d-scans for the setup in Fig. 1, with an additional 4 mm of propagation through water and 4 additional chirped mirror bounces. (c) Measured spectral intensity (black) and retrieved phase (thick red line, with the standard deviation indicated by thin red lines). (d) Retrieved temporal profile for the BK7 insertion that minimizes the intensity FWHM duration, corresponding to a 3.2 fs, 1.4-cycle pulse.

800 nm, but also has information on the phase of all pairs of frequencies that SFG to 400 nm. These different SFG signals will interfere with each other and generate the different features of the d-scan trace. In this work, the SFG signal was measured and retrieved between 290 and 450 nm. The signal above 450 nm was contaminated with a small amount of fundamental, hence was not usable. So one can argue that there is no SHG spectrum of the components outside the range of 580-900 nm, only SFG - e.g., signal from the mixing of 500 and 1000 nm will be located at 333 nm. This signal is enough to correctly retrieve the phase. In order to demonstrate that the measurement has information on the components outside the 580-900 nm range, one can do a simple calculation. If the measurement is indeed sensitive to the phase of the edges of the spectrum, then a small numerical perturbation introduced in this phase will change the shape of the corresponding d-scan trace, generating a trace with a larger error when compared to the measured trace. If the measurement is not sensitive, then one would expect no changes to the features of the trace and the error would be similar. This is demonstrated in Fig. 4.8. We considered a small temporal delay on the wavelengths above 950 nm (5 fs, Fig 4.8(a), red curve) and the wavelengths below 550 nm (3 fs, Fig 4.8(a), blue curve), which increased the pulse duration from 3.2 fs to 3.3 fs in both cases. We then calculate the error between measured and calculated traces: for the retrieved phase it is 0.7%, while for the 950 nm perturbation it is 2.4% and for the 550 nm one 2.2%. In order to visualize the change in the d-scan trace generated by perturbing the edges of the spectrum, we have represented the difference between the calculated traces and the measured one (Figs. 4.8(b), (c) and (d)). We see that a small change in the phase away from the center of the spectrum creates significant changes in the center of the d-scan trace, which makes it possible to retrieve the phase across the whole bandwidth.

4.3.7 Carrier-envelope phase stabilization

As mentioned previously, the dispersion-scan setup doubles as an f-2f interferometer. If used on a partial reflection of the main beam, it can serve for CEP monitoring and feedback, making it a single and complete solution for the generation and measurement of CEP-stable, high energy few-cycle pulses. Due to the high reflectivity of the chirped mirrors at 450 nm it is possible to couple some of the fundamental beam into the spectrometer, along with the SHG, simply by opening the variable slit. In these conditions we immediately obtain low contrast but consistent f-2f fringes in the d-scan trace. By further optimizing the alignment for fringe contrast we can achieve a good signal from which the slow CEP drift introduced from the output of the oscillator to just after the chirped mirror compressor can be extracted. The corresponding error provides a feedback signal to the second (piezo-actuated) wedge in the d-scan setup for fast correction of the CEP drift. Typical results are presented in Fig. 4.9, revealing a stability of 140 mrad over 100 minutes (measured at 50 Hz, 4 shots per spectrum - limited by the spectrometer minimum integration and data transfer times). Assuming the phase noise is at frequencies of 250 Hz or above, the phase stability would then be 280 mrad.

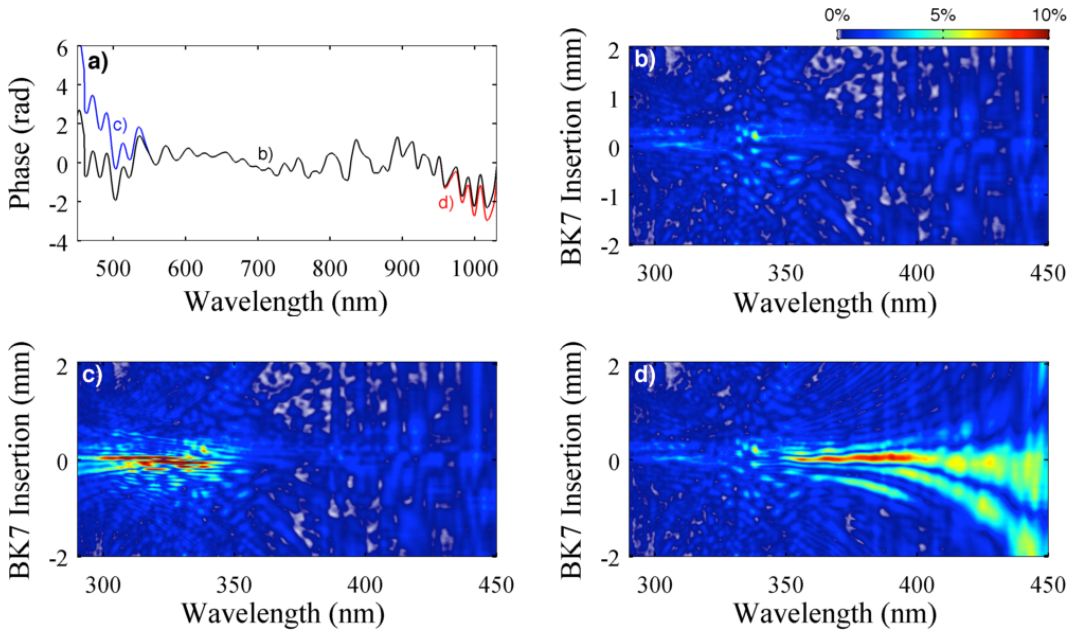

Figure 4.8: Illustration of the SFG nature of the d-scan trace. a) Retrieved phase (black) and perturbed phases (5 fs delay above 950 nm - red; 3 fs delay below 550 nm - blue). b) Absolute difference between measured and calculated trace for the retrieved phase, scaled by the peak of the measured trace, corresponding to a total error of 0.7%. c) Similar to b) but for the phase perturbed below 550 nm. Features with more than 10% amplitude appear at the SFG wavelengths between the whole spectrum and the <550 nm components, corresponding to a total error of 2.3%. d) Similar to b) but for the phase perturbed above 950 nm, corresponding to a total error of 2.2%.

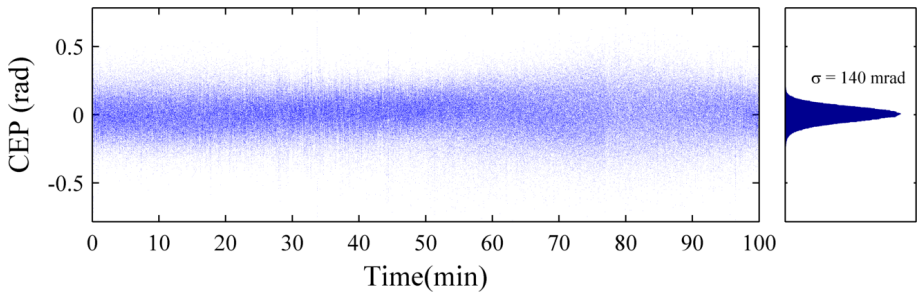

Figure 4.9: CEP jitter evolution over 100 minutes, demonstrating a stability of 140 mrad (integrated over 4 shots).

4.4 Conclusion

In conclusion, we report on a convenient single setup for simultaneous dispersion compensation, temporal characterization and CEP stabilization of octave-spanning pulses in the single-cycle regime, based on post-compression of a standard CPA laser amplifier using an Ar-filled hollow-fiber and ultra-broadband double-angle chirped mirrors. The employed pulse characterization technique - d-scan - only requires adding a broadband SHG stage to the usual post-compression setup, and motorizing the dispersion and CEP adjusting elements (e.g. glass wedges). The resulting d-scan traces provide a powerful visual and analytical tool for optimization of both the chirped mirror angles and the residual TOD of the system, and the same d-scan setup allows measuring and stabilizing the CEP drift of the compressed pulses. Minimization of TOD by using a small propagation path in water resulted in 1.4-cycle, 3.2 fs pulses with 160 μJ (<0.5% rms) and a residual CEP jitter of 140 mrad over 100 minutes. The simplicity and robustness of the demonstrated d-scan based source and setup should be useful for strong-field applications and attoscience. Furthermore, the ability to measure the spectral phase over more than one octave hints at the possibility of using this technique to measure and characterize sub-cycle pulses over a broad range of frequencies, only limited by the bandwidth of the nonlinear process employed.

Chapter 5

Attosecond lighthouse using long wavelengths: isolated attosecond pulses at 300 eV

5.1 Introduction

High harmonic generation using intense femtosecond lasers allows practical generation of fully coherent XUV/soft-X-ray radiation, typically in the form of multiple successive attosecond pulses, each generated by a different half-cycle of the driving pulse. In order to reduce the number of emitted attosecond pulses to one, several gating techniques have been devised, allowing either temporal or spectral selection of a single isolated attosecond pulse, which can then be used for experiments. Examples of these techniques are a) spectral selection of the highest energy photons emitted by the most intense half-cycle of a few-cycle pulse [142], b) polarisation-engineering of the driving pulse such that only a single successful recollision event occurs [151], c) using an intense laser which rapidly fills the ionisation fraction of the medium, arresting the emission of further attosecond pulses after the first [152], d) temporal tailoring of the driving field using multicolour synthesis to favour a single emission event [24], e) as well as exploiting long-range, time-dependent phase matching to achieve coherent build-up of a single attosecond pulse [153]. Recently, a new gating technique, based on a time-dependent attosecond pulse emission direction achieved by waveform rotation of the driving pulse, dubbed the attosecond lighthouse (ALH) was proposed [154] and demonstrated [4, 155] as a convenient way to generate isolated attosecond pulses, as each successive generated attosecond pulse can be selected and isolated simply by spatial filtering. An additional advantage of the ALH is that given an appropriate driving laser (few-cycle, >100-uJ level energies, CEP-stable), the experimental realisation is straightforward, as the required amount of wavefront rotation can be added easily by introducing a small angle glass wedge in the beam path [154]. Despite such developments, the current generation of isolated attosecond pulse sources is mostly limited to the XUV spectral range [35]. Generation of attosecond pulses at higher photon energies, specifically in the water window soft-X-ray range (284-543 eV)

would allow new applications, as the K-shell absorption edges of several biological building blocks are attainable, permitting e.g. element-specific time-resolved studies of charge transfer in biological molecules. Extension of IAP generation through HHG to higher photon energies requires scaling of the ponderomotive energy of the recolliding wave packet [156], which depends linearly on the intensity of the driving laser and inversely on the square of the laser wavelength. Extension of the HHG cutoff by scaling intensity was early achieved [157], but efficient X-ray generation is difficult due to the unfavourable phase-matching conditions created by the highly ionised plasma. Additionally, possible decoherence effects derived from extreme sensitivity to shot-to-shot fluctuations might present a significant obstacle for this approach [158]. Extension of the HHG cutoff by employing a longer wavelength laser presents an additional challenge, as the single-atom microscopic emission decreases dramatically as the wavelength increases [159, 160, 161, 162]), due to additional wave packed diffraction for longer HHG driving periods, leading to a less localised wave-packet at the recollision event. Fortunately, this lower yield can be partially compensated using ionisation assisted phase-matching in high pressure media [129], where the free-electrons created by the previous half-cycles delay the current half-cycle precisely by the amount opposite of the other sources of delay in relation the copropagating HHG radiation, leading to macroscopic buildup over a distance, only limited by reabsorption or driving pulse spatiotemporal deformation effects. This approach has been demonstrated as leading to similar photon numbers as the lower-wavelength driven HHG sources, which are sufficient for current experiments, e.g. [163, 164]. Given the desire for reliable sources of isolated attosecond pulses in the water window, it is worth investigating the possibility of extending the attosecond lighthouse to longer wavelengths by employing longer wavelength pulses. In this chapter we demonstrate the attosecond lighthouse up to the carbon K-edge at 300 eV. Furthermore, we perform a pratical comparison between IAP generation with the attosecond lighthouse vs IAP generation through high-frequency filtering, using the same, few-cycle, CEP-stable long wavelength laser source. This comparison serves as a guidance for researchers in the field evaluating which method to consider. We support the experimental data with SAR HHG simulations, which allow us to predict the pre/post-pulse contrast of the generated isolated attosecond pulses, as well as give insight into the temporal structure. We conclude that when comparable contrast ratios are predicted, the lighthouse leads to higher photon flux due to the losses caused by the filters necessary in high frequency filtering. Both techniques are predicted to lead to sub-400 as pulses. Additionally, we demonstrate the attosecond lighthouse in argon at 150 eV. The observed half-cycle resolved spectra are reminiscent of the expected single-atom response, modulated with a energy-dependent efficiency curve which varies with CEP.

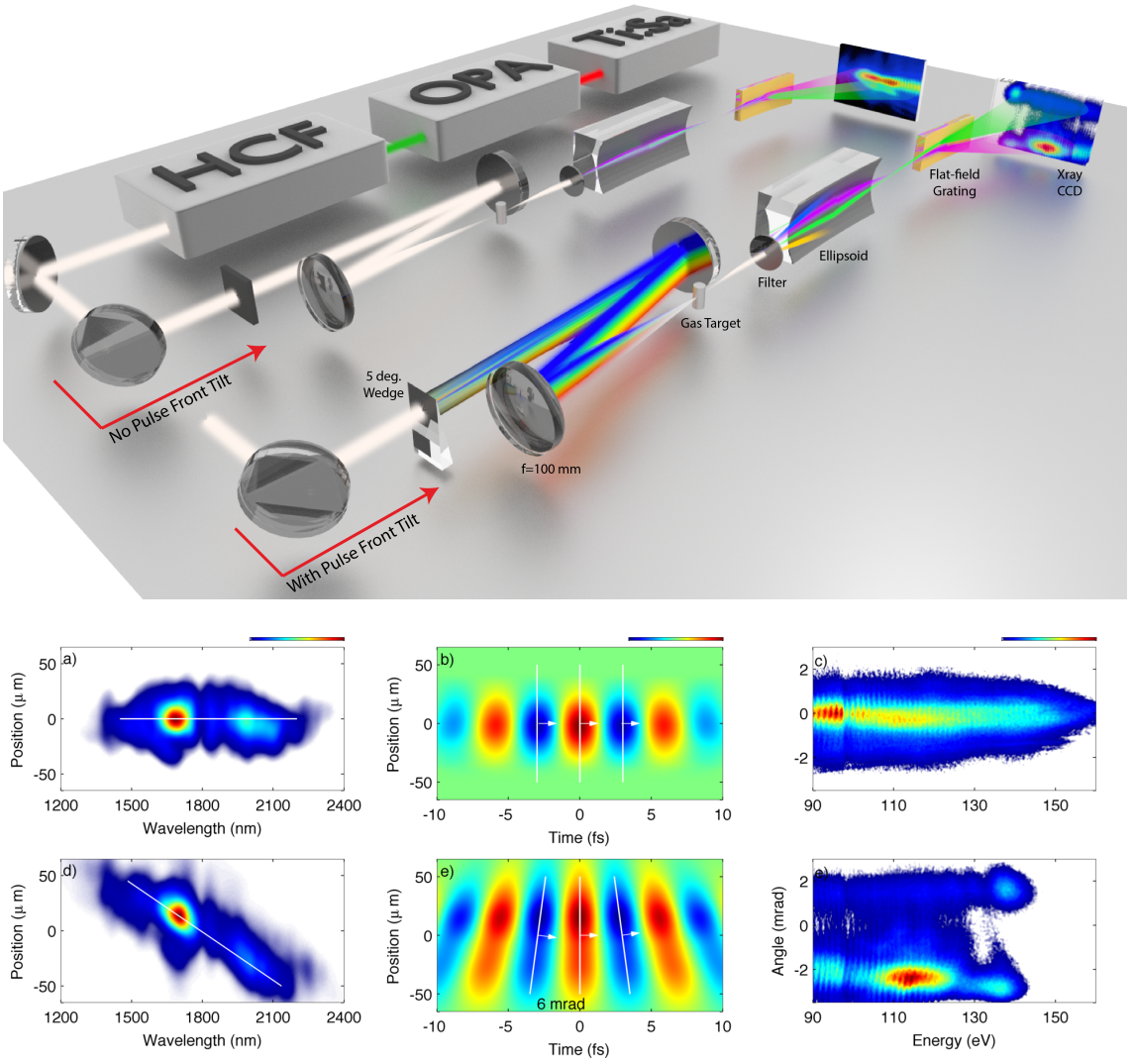

Figure 5.1: Experimental Setup (a) Schematic of the experimental setups, where the 1.8 μm pulses are focused in a high pressure gas target to intensities capable of HHG at 300 eV. Left: Setup without pulse front tilt (PFT), where are an RG1000 filter is used to compress the pulse on target. Right: Setup with pulse front tilt. A 5 degree fused silica wedge is inserted in the beam path to introduce the wavefront rotation necessary for the attosecond lighthouse effect. (b, c) Comparison between measured spatiospectral profiles for the without PFT (top) and with PFT (bottom) conditions. (d, e) Calculated wavefront from the measured spatiospectral profiles, revealing a wavefront rotation of 3 mrad per half-cycle. (f,g) Measured spatio-spectral profiles in both experimental conditions, revealing well-separated beamlets separated by 3 mrad when generating HHG in argon with WFR, as well as discrete harmonics without WFR. Due to the geometry of the experiment a maximum of two beamlets could be observed in the CCD at a given time.

5.2 Results

5.2.1 Experimental setup

High-energy pulses from a Ti:Sapphire amplifier system with 40 fs, 7 mJ at 1 kHz are frequency converted to 1.85 μm using an optical parametric amplifier, resulting in CEP-stable 0.8 mJ pulses with 40 fs. These are spectrally broadened through nonlinear propagation in a hollow core fibre filled with 1.5 bar of argon, which both broadens the spectrum and introduces adequate dispersion for subsequent compression down to 13 fs with bulk material [106]. A small part of the beam is sent to an f-2f setup which monitors and controls the CEP, leading to an RMS CEP jitter of 90 mrad at the selected CEP value. The CEP-stable pulses are then clipped by a variable Iris and propagated through a 3mm thick RG1000 filter (no WFR) or a 5 degree fused silica wedge at zero degrees incidence (with WFR). The iris allows optimisation of harmonic yield and cutoff during measurements. The resulting beam is then focused with an f=100 mm spherical mirror into a gas target (OD 1.5 mm, ID 0.5 mm) with 0.3 mm diameter entrance and exit holes, filled with neon at a backing pressure of 3.6 atm or argon at 0.8 bar. The residual fundamental radiation is filtered with a 100nm thick aluminium foil and the transmitted radiation is refocused using a grazing-incidence ellipsoidal mirror (Zeiss). An homebuilt spectrograph, consisting of a motorised slit, flat-field imaging reflective grating (Hitachi, 2400 lines/mm) and a cooled, back-illuminated CCD (Princeton Instruments) is used to measure the spatio-spectral profile of the radiation in function of CEP. Photon numbers are estimated using the measured spectra, the camera quantum efficiency and the measured grating diffraction efficiency. The angular aperture of the system is limited by the CCD height, leading to a range of 6 mrad.

The experiment was first done without any wavefront rotation, generating multiple attosecond bursts in the same emission direction, although due to the few-cycle nature of the pulse it is possible to spectrally filter only the emission from the highest intensity driving half-cycle, leading to an isolated attosecond pulse. Depending on the transmission of the filter employed different attenuation of the pre-/post pulses can be achieved. By replacing the 3mm-thick RG1000 filter acting as the dispersive bulk compressor of the pulses by a 5 degree wedge with the input face perpendicular to the incident beam, one introduces the wavefront rotation sufficient to create the lighthouse effect (Figs. 5.1 (d) and 5.1(e)). In Figures 5.1 (f) and (g) we compare spatio-spectral profiles generated through HHG in Argon without and with WFR, respectively. When applying WFR, we observe well-separated beamlets, due to the attosecond lighthouse effect, which were separated by 3 mrad, as expected from the measured spatio-spectral profile of the driving laser in focus (Fig 5.1 (e)). Due to the geometry of the experiment and size of the CCD camera, a maximum of two beamlets could be observed in the CCD at a given time. Due to the characteristics of Argon, phase-matched high harmonic generation is limited to the <160 eV range with the used pulses, as the intensities required to reach higher cutoffs lead to excessive ionisation which hampers phase matching, a mechanism described in [129].

Employing Neon instead of Argon as the nonlinear medium allows phase matching

of significantly higher energies [129], mostly due to a lower ionisation ratio. With neon at 3.6 bar of backing pressure and without WFR, we observe generation of radiation up to 380 eV (Fig 5.2(b)) - extending into the water window, covering the K-edge of Carbon (284 eV) and the L-edge of Calcium (342 eV). The absence of radiation below 200 eV is mostly due to the high reabsorption of neon at these energies. The peak of the spectrum has a centre energy which is highly dependent on the CEP of the driving pulse (Fig 5.2(a) and Fig 5.2(b)), characteristic of an half-cycle cutoff (HCOs, [165]), which gives insight into the different electron trajectories contributing to the HHG radiation. This indicates that by high frequency filtering one can obtain an isolated attosecond pulse when choosing the right CEP, as only emission from a single half-cycle will have predominantly produced the highest energy photons.

5.2.2 Attosecond lighthouse at 300 eV

When introducing WFR in the driving pulse, the measured spectrum spans up to 310 eV (Fig 5.2(c)), covering the Carbon K-edge (284 eV). The reduction of cutoff energy is compatible with the smaller peak intensity caused by the introduction of wavefront rotation, as it increases beam size and decreases spectral content, leading to a longer pulse. Due to the increased pulse duration we don't expect the the cutoff of successive half-cycles to vary significantly, which is verified experimentally with a practically constant cutoff with regards to CEPs (Fig 5.2(c)). As in the case of Argon, a CEP-dependent emission angle is found, with the emitted beamlets changing direction in function of CEP, as observed in Fig. 5.2 (b) and Fig. (a-c). Each of these beamlets corresponds to an isolated attosecond pulse, which can be easily selected by spatial filtering. The measured spectrum is sufficient to support a 30 as pulse, if the attochirp introduced by the generation process, would be fully compensated. Dispersion management for XUV attosecond pulses has been achieved using thin metal foils [166] or specially designed multilayer mirrors [167]. Given the flat phase of metallic foils at these energies [35], multilayer mirror designs seem to be the only avenue for compression, despite possessing significant losses and limited bandwidths [168].

5.2.3 Photon flux

For most applications, the utility of an laser source is closely related to its ability to deliver the most photons per second on target, as higher photon fluxes allow lower measurement times and higher signal to noise ratios. From the spatio-spectral measurements we estimated the relative photon flux we would have on target, i.e. after refocusing, for both generating schemes (Fig. 5.4). Without WFR, the overall generation is more efficient than when using the lighthouse technique, leading to a signal 5x stronger at the peak of the spectrum and 10x more photons when integrating over the 200-400 eV energy range. Despite this, with WFR, high frequency filtering is still needed to attenuate the low energy region of the spectrum (<250 eV) in order to isolate a single attosecond pulse - which is unnecessary with the attosecond lighthouse. In order to attenuate the <250 eV region, one can increase the thickness of the Aluminum filter, as it attenuates lower

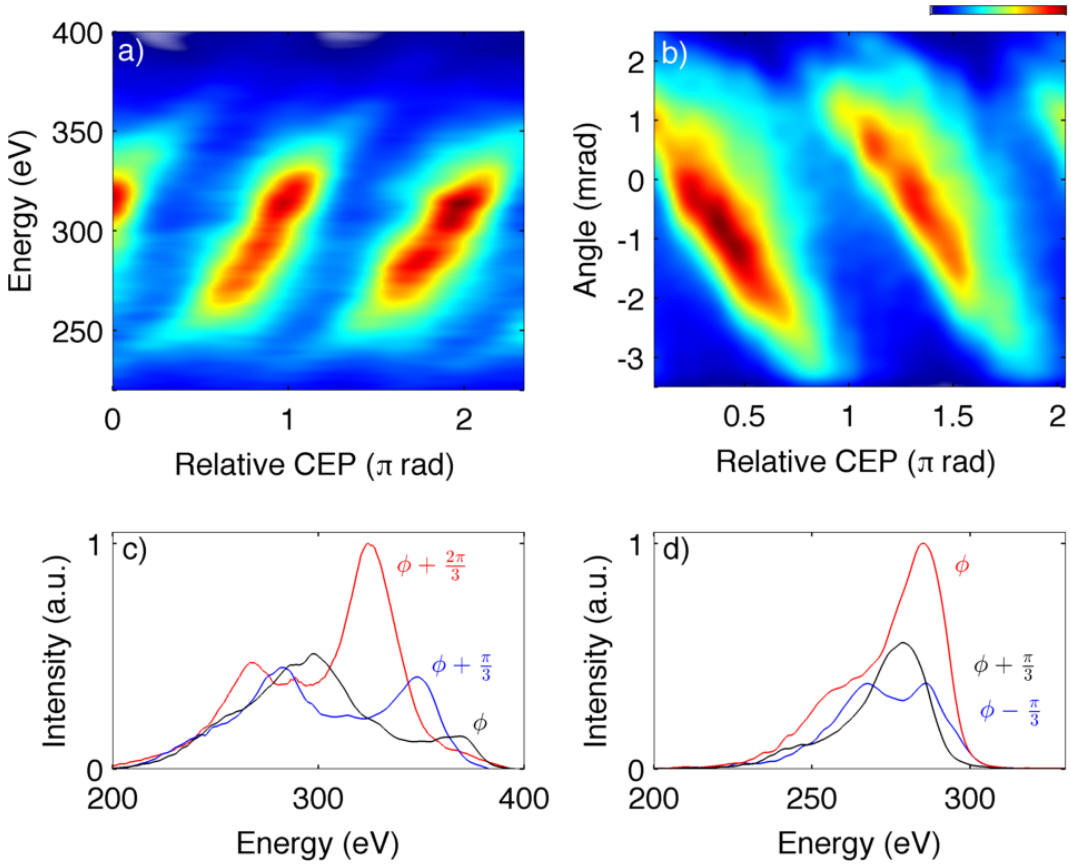

Figure 5.2: CEP dependence of neon-driven HHG - no WFR vs Attosecond Lighthouse (a) Spectrum in function of CEP of the driving pulse without WFR. (b) Spectra at 3 different CEPs for no WFR. Inset: spatio-temporal profile, for a fixed CEP. (c) When introducing WFR, the spectral range does not depend on CEP, only the intensity, when integrating over the whole measured beam profile. Due to the larger beam profile consequent to the introduction of PFT, the peak intensity is lower hence the generated cutoff is also lower than without WFR (300 vs 380 eV). (d) Integrated beam profile in function of CEP, revealing a clear angular mapping of the different beamlets, which move across the spectrometer angular range as the CEP is scanned.

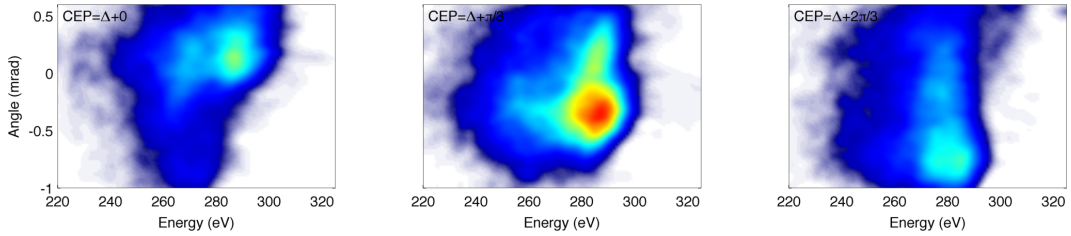

Figure 5.3: Far field spectro-spatial profiles in function of CEP. The propagation angle of the emitted beamlet scans the CCD vertically as CEP is varied.

energies more heavily than higher energies (5.4a)). For example, using a 400 nm filter instead of 100 nm used for these measurements one can attenuate the spectral region below 250 eV to have less than 3% of the total photon number, albeit decreasing the total photon number to less than that generated by the attosecond lighthouse.

5.3 Discussion

5.3.1 Simulation methods

The simulation results presented in this section were obtained with a model based on two different propagation codes. In the case of no WFR, cylindrical symmetry is assumed and nonlinear propagation using pseudo spectral methods is used to numerically evolve the driving laser electric field. Dispersion, diffraction, self-phase modulation, plasma dephasing and absorption are taken into account [169]. Ionization rates are calculated using the Ammosov-Delone-Krainov formula (ADK, [170]). After calculation of the driving laser field the single-atom HHG response is computed at every point of the propagation grid (resampled to provide appropriate resolution) using an augmented Lewenstein model [5, 160] with an electron birth factor that incorporates the ADK ionization rates [171, 172, 79] and photorecombination cross-section [173] for the recombination step [174]. Gaussian input pulses in the spatial and temporal domains were considered, and the target was considered to have a density of $1.2\text{x}10^{19}$ atoms per cm^3. The simulated target thickness was the full inner diameter (0.5 mm).

In the case of WFR, the single-atom response was calculated across the spatial dimension of the beam, using the code described above and used in [160]. The WFR was introduced by modelling the electric field using the spatio-spectral measured quantities, and using Gaussian integrated spectral and spatial profiles to minimize numerical noise. The pulse is propagated into the far field through Fourier analysis in order to calculate spatiospectral profiles.

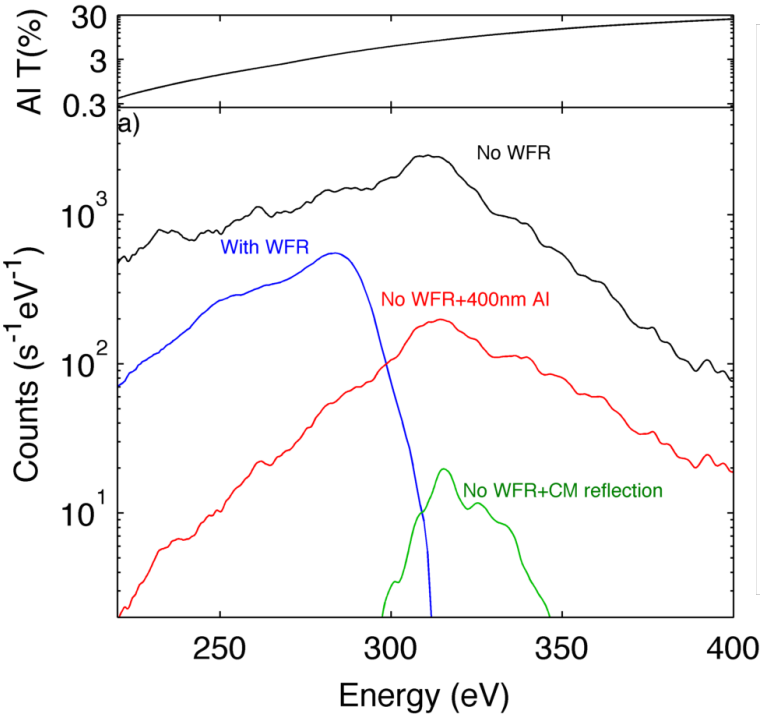

Figure 5.4: Comparison of measured photon counts. Black: no WFR, corresponding to a multiple attosecond pulse burst. Blue: Integrated spectrum generated with WFR, corresponding to a single beamlet, i.e. a single attosecond pulse. Red: Spectrum generated without WFR after filtering through a 400nm Al filter, which attenuates the low energy region where the undesired attosecond pulse is located, leading to a single attosecond pulse with high contrast. Green: Spectrum generated without WFR, after reflection from a chirped mirror designed for this energy range. Chirped mirror reflection profile from Ref. [168]. Top: transmission of a 400 nm thick foil of Aluminium.

5.3.2 Simulation results

Using the measured experimental conditions we performed high harmonic generation simulations in order to gain insight on the spatiotemporal properties of the generated attosecond radiation.

In the case of no WFR, HHG spectrum in function of CEP after propagation was simulated using the estimated peak intensity and measured pulse duration (Fig.5.5). A structure similar to figure 5.2 a) is observed, reproducing both the cutoff and tilt of the half-cycle cutoff trace [165]. No short-long trajectory interference is observed, similarly to the experimental data.

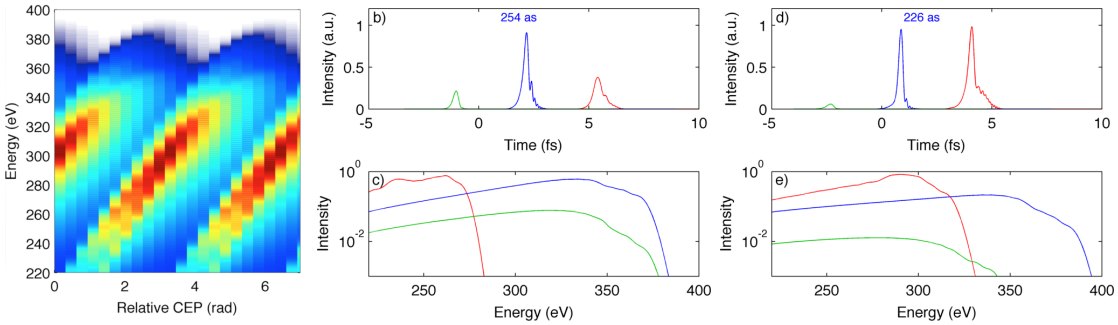

Figure 5.5: Simulated HHG spectrum in function of CEP without WFR. (a) Half-cycle cutoff scan, i.e. HHG spectrum in function of CEP, revealing a changing center wavelength characteristic of a few-cycle pulse. (b) Simulated temporal profile for the CEP that maximizes post-pulse contrast (1:2.7 in this case). (c) Corresponding half-cycle resolved spectra to (b). (d),(e) Same as (b) and (c) but for CEP more suitable to high contrast high-frequency filtering, i.e. if a spectral filter with high contrast ratio existed, transmitting only radiation above 345 eV, a high contrast isolated pulse would be generated. Due to the used filters having smooth transmission profiles this option was not considered.

In the case of WFR, we have calculated the microscopic response in the focus of the pulse. The spatio-temporal structure creates a set of attosecond bursts with varying wave-front angle relative to the propagation direction (Fig 5.6 (a)). Each of these bursts will propagate in different directions and reach the spectrometer at different positions. In Fig 5.6 (b) the spatio-spectral profile of the simulated beamlets is represented, where the simulation range was chosen to match the experimental one. The microscopic response includes both short and long trajectories, both will interfere (as they both cover the same energy ranges at different times) and create the observed interference pattern, which contrasts with the measured data (Fig 5.3). By applying a temporal apodization window to each emitted attosecond burst that rejects all the recombination events happening after the cutoff, one can simulate this process with only short trajectories contributing (Fig 5.7). One can see that there is a good match with experimental data on the structure and size of the produced beamlet, leading us to argue that the long trajectories were

suppressed. This indicates some influence of phase-matching, as phase-matched HHG is known to favour the short trajectories greatly [175].

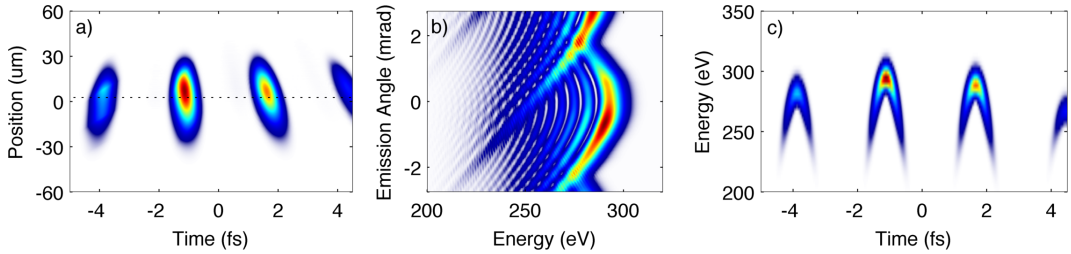

Figure 5.6: Simulation results with WFR, considering both short and long trajectories, for a single CEP. (a) Spatio-temporal profile of the generated beamlets in the near-field, revealing the gradually changing wave-front direction. (b) Spatio-spectral profile in the far field, revealing clear interference between the short and long trajectories. (c) Spectrogram of the emitted burst along the dotted line in (a).

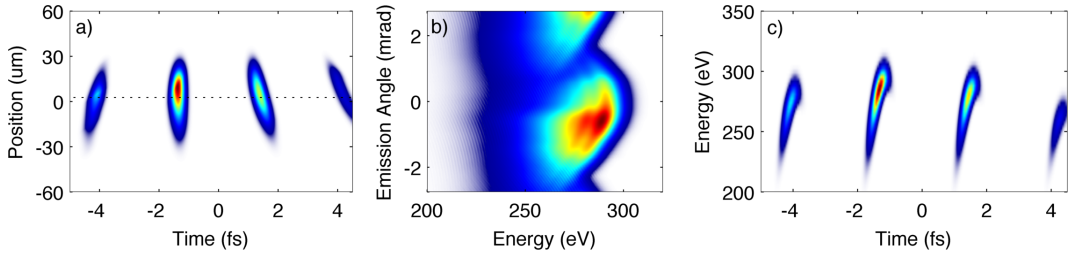

Figure 5.7: Simulation results with WFR, considering only short trajectories, for a single CEP. (a) Statio-temporal profile of the generated beamlets in the near-field, revealing the gradually changing wave-front direction. (b) Spatio-spectral profile in the far field. (c) Spectrogram of the emitted burst along the dotted line in (a).

5.3.3 Contrast ratio

Given the good agreement between measured and simulated data, we can compare two attosecond pulse generation techniques - high frequency filtering of few-cycle driven HHG and the attosecond lighthouse, in order to gain insight into the contrast ratio achievable with each technique (Fig.5.8)

In the case without WFR, by considering the effect of an 400 nm thick Aluminum filter and choosing the CEP that maximised pre- and post- pulse contrast one obtains an attosecond pulse with 230 as (Intensity FWHM) at 325 eV with a 1:5 and 1:10 intensity ratio to pre- and post- pulses, respectively. If the aluminium thickness would be shorter, the contrast to the post pulse would decrease, e.g. a 200 nm Al filter would result in a

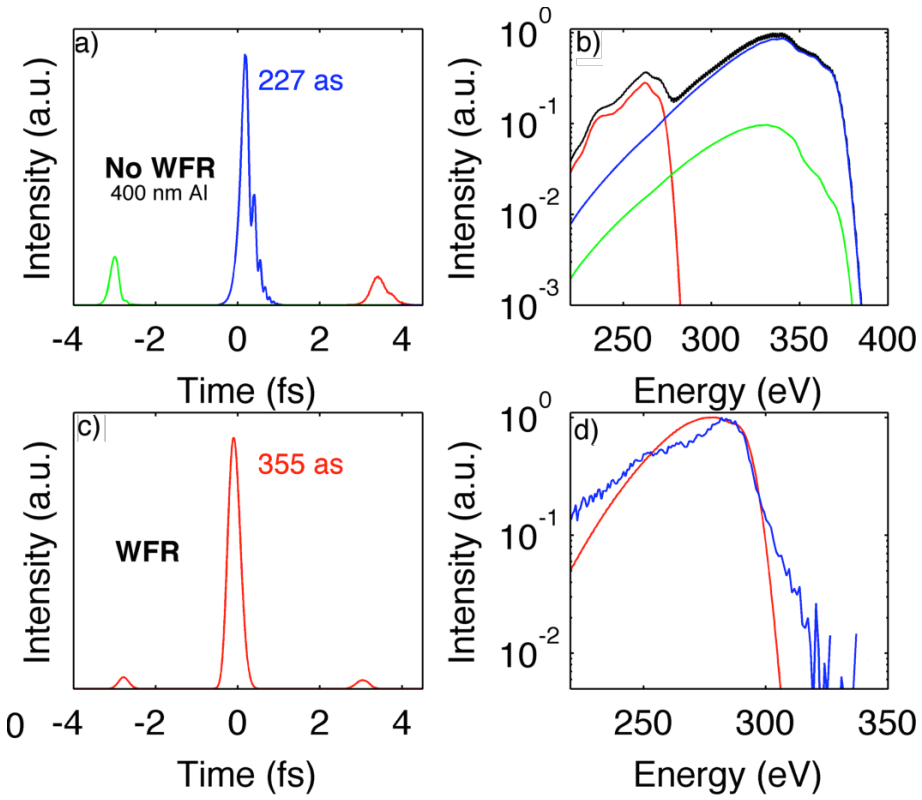

Figure 5.8: Simulated pulse profiles for both pulse attosecond pulse isolation methods. (a) Simulated temporal profile of the attosecond burst generated without WFR, filtered with a 400nm Al foil, leading to a pre/post pulse contrast of 1:5. (b) Half-cycle resolved spectrum corresponding to the pulse in (a). (c) Simulated pulse profile in the case of wavefront rotation, leading to a pre/post pulse contrast of 1:20. (d) Red: Spectrum corresponding to the central pulse in figure (c). Blue: Measured spectrum with WFR.

1:3.6 contrast. In the case of the attosecond lighthouse, simulations reveal that if one spatially filters the centre beamlet the resulting pulse has an intensity FWHM of 355 as, but a pre- pulse contrast of 1:20.

5.3.4 Phase-matching effects

The time-to-angle mapping created by the lighthouse effect is not only useful as a source of isolated attosecond pulses but also to study the underlying physics of high harmonic generation, as demonstrated in [155]. For HHG in both neon and argon, we found that the spectral structure of the beamlets changed rapidly between half-cycles. In the case of neon the emission is more intense only for a narrow range of CEP values (e.g. Fig 5(b)). Additionally, in the case of the attosecond lighthouse in Argon (fig 6) we observe

a constant cutoff, spectral range and peak spectral intensity as the CEP is varied, but a significant change in the position of the high intensity peak of the spectrum for small CEP changes. A rapid change of intensity/yield between half-cycles is compatible with the known ionisation dynamics of sub-two cycle pulses [142], where small changes in half-cycle intensity with CEP translate to enormous changes in ionisation fraction, hence greatly varying the emission intensity upon recollision. As pulse front tilt increases pulse duration in focus, in our case to 20 fs, we don't expect this effect to be significant in our case. Additionally this explanation does not explain the observations in Argon. Hence a different explanation is necessary. Our observations are compatible with the proposed concept of a temporally narrow phase matching window [153]. When employing long wavelength driving lasers the phase-matching conditions are highly sensitive to the ionisation fraction seen by a particular half-cycle [129], hence the small ionisation fraction changes done by varying the CEP can have big impact on the phase-mismatch seen by different half-cycles. Hence the temporal window over which high harmonic generation is efficient can be narrow, in extreme cases leading to the coherent buildup of a single half-cycle from a multi-cycle laser, as demonstrated in [153]. The observation of an CEP-dependent energy shifting peak overlaid in a spectrum resembling the single-atom response further suggests that phase matching effects are responsible for the observed features. For a temporal difference of 3 fs (i.e. one half-cycle) in relation to the envelope the phase-matched peak changes 30 eV.

5.4 Conclusion

In summary, we have demonstrated a source of isolated attosecond pulses at the carbon K-edge using the attosecond lighhouse, which is estimated to yield pulses with better contrast than those generated by traditional high-frequency filtering of few-cycle HHG. Experimental comparison between the two methods suggests that the attosecond lighthouse leads to more generated photons for conditions resulting in an isolated attosecond pulse. Simulations indicate that the generated pulses have sub-400 as durations, and pre-pulse contrast ratios of the order of 1:5 and 1:20 in the high frequency filtering and attosecond lighthouse cases, respectively. Using the time-to-angle mapping properties of the lighthouse effect, we identifed rapidly changing phase matching conditions, leading to significantly different spectral features for successive half-cycles, even though these possess the same cutoff. This further underlines the importance of phase-matching for long wavelength driven high harmonic radiation [129]. These results demonstrate an experimentally straightforward method to generate isolated attosecond pulses in the water window, which are long sought tools for element-specific sub-fs resolution studies of materials and biological compounds.

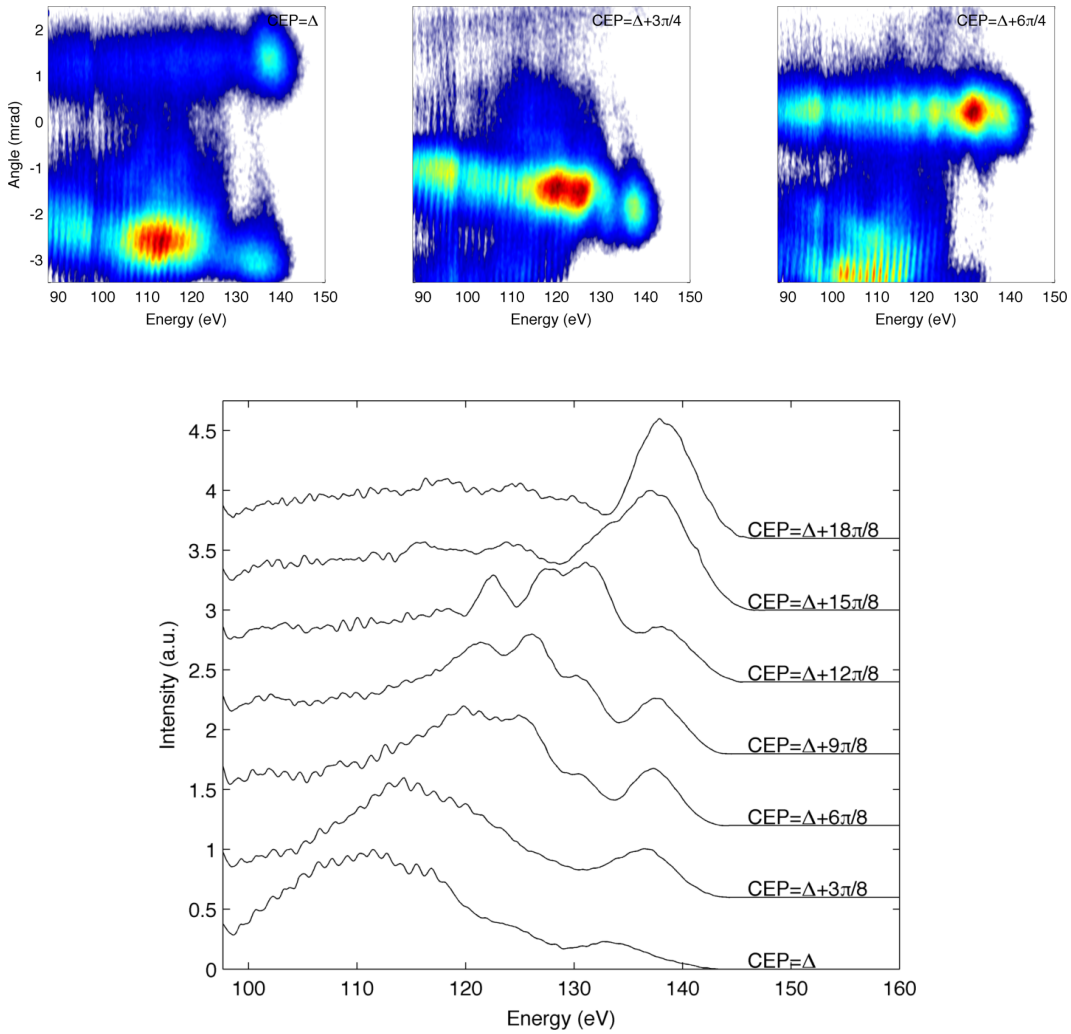

Figure 5.9: Rapidly changing phase matching conditions during HHG in Argon in function of CEP (a-c) Generated spatiospectral profiles for 3 CEPs, exhibiting a rapidly changing HHG emission spectrum between two adjacent half-cycles for the same CEP (a) and rapidly changing between CEPs. (d) Normalized spectra integrated over each beamlet for various CEPs, revealing a shifting phase-matched peak with CEP. The spacing of the observed fringe patterns agree with the interference pattern characteristic of short- and long-trajectory interference.

Chapter 6

Conclusion

In this thesis we have explored the generation and control of phase-stable intense few-cycle light pulses covering different regions of the spectrum, from the mid-IR to the soft-X-ray. Different techniques such as supercontinuum generation, optical parametric amplification and high harmonic generation were used for this effect. Amongst the achievements of this thesis are:

3.3 Octave supercontinuum generation

We have demonstrated for the first time multi-octave phase-stable supercontinuum generation through filamentation in bulk material of SWIR-/mid-IR femtosecond pulses. The measured spectra span from 500-2500 nm when pumping at 2.1 μm and 450-4500 nm (corresponding to 3.3 octaves) when pumping at 3.1 μm with a spectral energy density of 1 pJ/nm-10 nJ/nm. Intensity and phase stability indicate shot-to-shot stability of the waveform. Angularly-resolved far-field spectra were measured, matching the predictions from current theoretical understanding of filamentation. Numerical simulations corroborate this result and predict self-compression to the single-cycle limit.

Pulses with spectral densities in excess of 1 pJ/nm are sufficient for many time resolved spectroscopy experiments, which when coupled with the spectral bandwidth of this source results in a flexible tool for the study of fundamental physical and chemical processes from the visible to the mid-IR. The field of ultrafast optics and few-cycle pulse generation has already reached the octave-spanning, single-cycle limit and now intense sub-cycle pulses are beginning to be explored. This source, when coupled with appropriate phase compensation, would enable electric fields with tailorable waveforms, down to the half-cycle oscillation limit.

High intensity, phase-stable 2 μm source

We have developed a compact, 2-stage white-light seeded NOPA based on Ti:Sa pumped BiB_3O_6, capable of generating spectra for <2 cycle pulses at 2 μm with energies of 600 μJ. Pulses with 42 fs were measured with a previous iteration of the source, and a CEP stability of 80 mrad over 1 hour has been demonstrated. High harmonic spectra

were generated using this source, demonstrating ponderomotive scaling of HHG and generating harmonic spectrum up to 190 eV. Spectral broadening capable of supporting a single-cycle pulse has also been demonstrated with hundreds of μJ of energy.

This scalable, phase-stable source with broadband spectrum at 2 μm demonstrates the feasibility of intense, few-cycle sources in the SWIR, which can enable high harmonic generation at higher photon energies through ponderomotive scaling, including phase-matched soft-X-ray generation in the water window.

1.4 cycle pulse generation and diagnostics at 740 nm

Reliable and straightforward diagnostics for near-single-cycle pulses are essential for the operation of such sources. In this work we developed a convenient technique for simultaneous dispersion compensation, temporal characterization and CEP stabilization of octave-spanning pulses in the single-cycle regime. The employed pulse characterization technique - d-scan - only requires adding a broadband SHG stage to the usual post-compression setup. The resulting d-scan traces provide a visual tool for day-to-day diagnostic of the quality of pulse compression. The same d-scan setup allows measuring and stabilizing the CEP drift of the compressed pulses. Using this technique we demonstrate 1.4-cycle, 3.2 fs pulses with 160 μJ (<0.5% rms) and a residual CEP jitter of 140 mrad over 100 minutes. The simplicity and robustness of the demonstrated source and d-scan setup enables strong-field applications and e.g. attoscience experiments with complete knowledge of the employed optical waveform in a practical fashion.

Attosecond lighthouse at 300 eV

The availability of isolated attosecond pulses at the Carbon K-edge (284 eV) would allow a series of novel experiments, including time- and space- resolved spectroscopy of biological compounds or diffractive imaging with extreme resolution. In this work we have demonstrated a source of isolated attosecond pulses at the carbon K-edge using the attosecond lighthouse technique. Experimental comparison between the two methods suggests that the attosecond lighthouse leads to more photon flux for conditions resulting in an isolated attosecond pulse on a second experimental target. The attosecond lighthouse effect is also demonstrated at 150 eV.

These results demonstrate an experimentally straightforward method to generate isolated attosecond pulses in the water window, which are expected to be an enabling technology for table-top, time-resolved soft-X-ray attoscience.

Summary

In Fig. 6.1 are represented together all the generated sources of coherent radiation in this thesis in the spectral domain.

With the increased availability of new sources of coherent radiation in new regions of the electromagnetic spectrum current applications and experiments are extended.

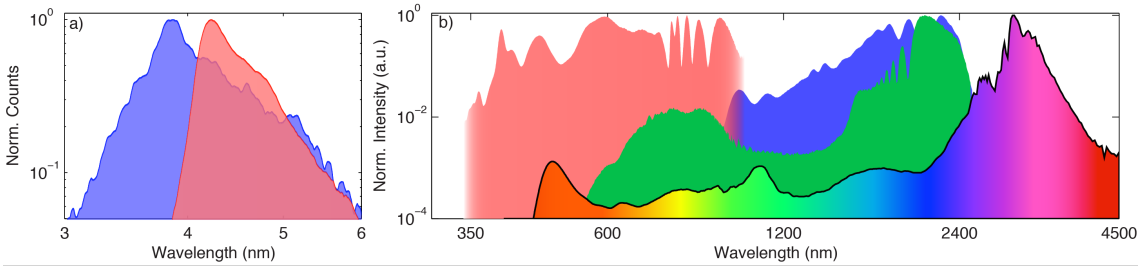

Figure 6.1: Summary of the generated sources of coherent light created in this thesis, compared in the spectral domain. a) soft-X-ray sources from chapter 5. Red: Pulses generated through the attosecond lighthouse effect. Blue: Pulses generated through HHG of a sub-2 cycle pulse, spanning one octave around the carbon K-edge (4.3 nm). b) Phase-stable, temporally coherent sources from the UV to the mid-IR. Red: 1.5 octave supercontinuum at 690nm generated through hollow core fiber compression; Blue: 1 octave supercontinuum at 1.9 μm generated through hollow core fiber compression. Green: 2 octave supercontinuum generated at 2 μm through filamentation in YAG. Rainbow: >3 octave supercontinuum generated at 3 μm through filamentation in YAG.

Ideally, these sources will provide the novel tools and insight that will allow unveiling the next generation of applications.

Bibliography

[1] J Ullrich et al. "Recoil-ion and electron momentum spectroscopy: reaction-microscopes". In: *Reports on Progress in Physics* 66.9 (2003), p. 1463. URL: http://stacks.iop.org/0034-4885/66/i=9/a=203.

[2] A. D. Shiner et al. "Probing collective multi-electron dynamics in xenon with high-harmonic spectroscopy". In: *Nature Physics* 7.6 (Mar. 2011), pp. 464–467. ISSN: 1745-2473. DOI: 10.1038/nphys1940. URL: http://www.nature.com/doifinder/10.1038/nphys1940.

[3] P Leemans W.\ et al. "Multi-GeV Electron Beams from Capillary-Discharge-Guided Subpetawatt Laser Pulses in the Self-Trapping Regime". In: *Phys. Rev. Lett.* 113.24 (Dec. 2014), p. 245002. DOI: 10.1103/PhysRevLett.113.245002. URL: http://link.aps.org/doi/10.1103/PhysRevLett.113.245002.

[4] Jonathan A Wheeler et al. "Attosecond lighthouses from plasma mirrors". In: *Nat Photon* 6.12 (2012), pp. 829–833. URL: http://dx.doi.org/10.1038/nphoton.2012.284.

[5] M Lewenstein et al. "Theory of high-harmonic generation by low-frequency laser fields". In: *Physical Review A* 49.3 (1994), p. 2117.

[6] Rafael R Gattass and Eric Mazur. "Femtosecond laser micromachining in transparent materials". In: *Nat Photon* 2.4 (Apr. 2008), pp. 219–225. ISSN: 1749-4885. URL: http://dx.doi.org/10.1038/nphoton.2008.47.

[7] Donald Umstadter. "Review of physics and applications of relativistic plasmas driven by ultra-intense lasers". In: *Physics of Plasmas (1994-present)* 8.5 (2001), pp. 1774–1785.

[8] Yong-Lai Zhang et al. "Designable 3D nanofabrication by femtosecond laser direct writing". In: *Nano Today* 5.5 (2010), pp. 435–448.

[9] Ridthee Meesat et al. "Cancer radiotherapy based on femtosecond IR laser-beam filamentation yielding ultra-high dose rates and zero entrance dose". In: *Proceedings of the National Academy of Sciences* 109.38 (2012), E2508–E2513. DOI: 10.1073/pnas.1116286109. URL: http://www.pnas.org/content/109/38/E2508.abstract.

[10] Mohammed Tharwat Hassan. "Synthesis and control of attosecond light transients". In: (2013).

[11] Kun Zhao et al. “Tailoring a 67 attosecond pulse through advantageous phase-mismatch”. In: *Opt. Lett.* 37.18 (Sept. 2012), pp. 3891–3893. DOI: 10.1364/OL.37.003891. URL: http://ol.osa.org/abstract.cfm?URI=ol-37-18-3891.

[12] Ahmed H Zewail. “Femtochemistry: Atomic-Scale Dynamics of the Chemical Bond Using Ultrafast Lasers (Nobel Lecture)”. In: *Angewandte Chemie International Edition* 39.15 (2000), pp. 2586–2631.

[13] C L Tang and D J Erskine. “Femtosecond Relaxation of Photoexcited Nonequilibrium Carriers in {\mathrm{Al}}_{x}{\mathrm{Ga}}_{1-x}\mathrm{As}”. In: *Phys. Rev. Lett.* 51.9 (Aug. 1983), pp. 840–843. DOI: 10.1103/PhysRevLett.51.840. URL: http://link.aps.org/doi/10.1103/PhysRevLett.51.840.

[14] J K Trautman et al. “Femtosecond dynamics of energy transfer in B800-850 light-harvesting complexes of Rhodobacter sphaeroides”. In: *Proceedings of the National Academy of Sciences* 87.1 (1990), pp. 215–219.

[15] M Drescher et al. “Time-resolved atomic inner-shell spectroscopy”. In: *Nature* 419.6909 (Oct. 2002), pp. 803–807. ISSN: 0028-0836. URL: http://dx.doi.org/10.1038/nature01143http://www.nature.com/nature/journal/v419/n6909/suppinfo/nature01143_S1.html.

[16] M Schultze et al. “Delay in photoemission”. In: *Science* 328.5986 (June 2010), pp. 1658–1662. DOI: 10.1126/science.1189401.

[17] Ferenc Krausz. “Attosecond physics”. In: *Reviews of Modern Physics* 81.1 (Feb. 2009), pp. 163–234. ISSN: 0034-6861. DOI: 10.1103/RevModPhys.81.163. URL: http://link.aps.org/doi/10.1103/RevModPhys.81.163.

[18] C O Alley et al. “Apollo 11 laser ranging retro-reflector: initial measurements from the McDonald Observatory”. In: *Science* 167.3917 (1970), pp. 368–370.

[19] Yves Salvadé et al. “High-accuracy absolute distance measurement using frequency comb referenced multiwavelength source”. In: *Appl. Opt.* 47.14 (May 2008), pp. 2715–2720. DOI: 10.1364/AO.47.002715. URL: http://ao.osa.org/abstract.cfm?URI=ao-47-14-2715.

[20] CoddingtonI. et al. “Rapid and precise absolute distance measurements at long range”. In: *Nat Photon* 3.6 (June 2009), pp. 351–356. ISSN: 1749-4885. URL: http://dx.doi.org/10.1038/nphoton.2009.94.

[21] C W Chou et al. “Optical Clocks and Relativity”. In: *Science* 329.5999 (2010), pp. 1630–1633. DOI: 10.1126/science.1192720. URL: http://www.sciencemag.org/content/329/5999/1630.abstract.

[22] Birgitta Bernhardt et al. “Cavity-enhanced dual-comb spectroscopy”. In: *Nat Photon* 4.1 (Jan. 2010), pp. 55–57. ISSN: 1749-4885. URL: http://dx.doi.org/10.1038/nphoton.2009.217http://www.nature.com/nphoton/journal/v4/n1/suppinfo/nphoton.2009.217_S1.html.

[23] A Wirth et al. “Synthesized light transients”. In: *Science* 334.October (2011), pp. 195–200. URL: http://www.sciencemag.org/content/334/6053/195.short.

[24] L. Chipperfield et al. “Ideal Waveform to Generate the Maximum Possible Electron Recollision Energy for Any Given Oscillation Period”. In: *Physical Review Letters* 102.6 (Feb. 2009), pp. 2–5. ISSN: 0031-9007. DOI: 10.1103/PhysRevLett.102.063003. URL: http://link.aps.org/doi/10.1103/PhysRevLett.102.063003.

[25] R R Alfano and S L Shapiro. “Direct Distortion of Electronic Clouds of Rare-Gas Atoms in Intense Electric Fields”. In: *Phys. Rev. Lett.* 24.22 (June 1970), pp. 1217–1220. DOI: 10.1103/PhysRevLett.24.1217. URL: http://link.aps.org/doi/10.1103/PhysRevLett.24.1217.

[26] R R Alfano and S L Shapiro. “Emission in the Region 4000 to 7000 \AA{}Via Four-Photon Coupling in Glass”. In: *Phys. Rev. Lett.* 24.11 (Mar. 1970), pp. 584–587. DOI: 10.1103/PhysRevLett.24.584. URL: http://link.aps.org/doi/10.1103/PhysRevLett.24.584.

[27] R R Alfano and S L Shapiro. “Observation of Self-Phase Modulation and Small-Scale Filaments in Crystals and Glasses”. In: *Phys. Rev. Lett.* 24.11 (Mar. 1970), pp. 592–594. DOI: 10.1103/PhysRevLett.24.592. URL: http://link.aps.org/doi/10.1103/PhysRevLett.24.592.

[28] D E Spence, P N Kean, and W Sibbett. “60-fsec pulse generation from a self-mode-locked Ti:sapphire laser”. In: *Opt. Lett.* 16.1 (Jan. 1991), pp. 42–44. DOI: 10.1364/OL.16.000042. URL: http://ol.osa.org/abstract.cfm?URI=ol-16-1-42.

[29] R Ell et al. “Generation of 5-fs pulses and octave-spanning spectra directly from a Ti:sapphire laser”. In: *Opt. Lett.* 26.6 (Mar. 2001), pp. 373–375. DOI: 10.1364/OL.26.000373. URL: http://ol.osa.org/abstract.cfm?URI=ol-26-6-373.

[30] C Chudoba et al. “All-solid-state Cr:forsterite laser generating 14-fs pulses at 1.3 μm”. In: *Opt. Lett.* 26.5 (Mar. 2001), pp. 292–294. DOI: 10.1364/OL.26.000292. URL: http://ol.osa.org/abstract.cfm?URI=ol-26-5-292.

[31] Nikolai Tolstik, Evgeni Sorokin, and Irina T Sorokina. “Graphene mode-locked Cr:ZnS laser with 41 fs pulse duration”. In: *Opt. Express* 22.5 (Mar. 2014), pp. 5564–5571. DOI: 10.1364/OE.22.005564. URL: http://www.opticsexpress.org/abstract.cfm?URI=oe-22-5-5564.

[32] J A Giordmaine and Robert C Miller. “Tunable Coherent Parametric Oscillation in LiNb{\mathrm{O}}_{3} at Optical Frequencies”. In: *Phys. Rev. Lett.* 14.24 (June 1965), pp. 973–976. DOI: 10.1103/PhysRevLett.14.973. URL: http://link.aps.org/doi/10.1103/PhysRevLett.14.973.

[33] Jay E Sharping et al. “Octave-spanning, high-power microstructure-fiber-based optical parametric oscillators”. In: *Opt. Express* 15.4 (Feb. 2007), pp. 1474–1479. DOI: 10.1364/OE.15.001474. URL: http://www.opticsexpress.org/abstract.cfm?URI=oe-15-4-1474.

[34] Paul B Corkum. “Plasma perspective on strong field multiphoton ionization”. In: *Physical Review Letters* 71.13 (1993), p. 1994.

[35] Michael Chini, Kun Zhao, and Zenghu Chang. “The generation, characterization and applications of broadband isolated attosecond pulses”. In: *Nat Photon* 8.3 (Mar. 2014), pp. 178–186. ISSN: 1749-4885. URL: http://dx.doi.org/10.1038/nphoton.2013.36210.1038/nphoton.2013.362.

[36] Hanieh Fattahi et al. “Efficient, octave-spanning difference-frequency generation using few-cycle pulses in simple collinear geometry”. In: *Opt. Lett.* 38.20 (Oct. 2013), pp. 4216–4219. DOI: 10.1364/OL.38.004216. URL: http://ol.osa.org/abstract.cfm?URI=ol-38-20-4216.

[37] F DeMartini et al. “Self-Steepening of Light Pulses”. In: *Phys. Rev.* 164.2 (Dec. 1967), pp. 312–323. DOI: 10.1103/PhysRev.164.312. URL: http://link.aps.org/doi/10.1103/PhysRev.164.312.

[38] Govind P Agrawal. *Nonlinear fiber optics*. Academic press, 2007.

[39] R Y Chiao, E Garmire, and C H Townes. “Self-Trapping of Optical Beams”. In: *Phys. Rev. Lett.* 13.15 (Oct. 1964), pp. 479–482. DOI: 10.1103/PhysRevLett.13.479. URL: http://link.aps.org/doi/10.1103/PhysRevLett.13.479.

[40] T K Gustafson et al. “Self-Modulation, Self-Steepening, and Spectral Development of Light in Small-Scale Trapped Filaments”. In: *Phys. Rev.* 177.1 (Jan. 1969), pp. 306–313. DOI: 10.1103/PhysRev.177.306. URL: http://link.aps.org/doi/10.1103/PhysRev.177.306.

[41] M D Feit and J A Fleck. “Effect of refraction on spotsize dependence of laser-induced breakdown”. In: *Applied Physics Letters* 24.4 (1974).

[42] B La Fontaine et al. “Filamentation of ultrashort pulse laser beams resulting from their propagation over long distances in air”. In: *Physics of Plasmas (1994-present)* 6.5 (1999).

[43] E T J Nibbering et al. “Conical emission from self-guided femtosecond pulses in air”. In: *Opt. Lett.* 21.1 (Jan. 1996), pp. 62–64. DOI: 10.1364/OL.21.000062. URL: http://ol.osa.org/abstract.cfm?URI=ol-21-1-62.

[44] A Couairon and A Mysyrowicz. “Femtosecond filamentation in transparent media”. In: *Physics Reports* 441.2-4 (Mar. 2007), pp. 47–189. ISSN: 03701573. DOI: 10.1016/j.physrep.2006.12.005. URL: http://linkinghub.elsevier.com/retrieve/pii/S037015730700021X.

[45] R L Fork et al. "Compression of optical pulses to six femtoseconds by using cubic phase compensation". In: *Opt. Lett.* 12.7 (July 1987), pp. 483–485. DOI: 10.1364/OL.12.000483. URL: http://ol.osa.org/abstract.cfm?URI=ol-12-7-483.

[46] M Nisoli, S De Silvestri, and O Svelto. "Generation of high energy 10 fs pulses by a new pulse compression technique". In: *Applied Physics Letters* 68.20 (1996).

[47] Samuel Bohman et al. "Generation of 5.0 fs, 5.0 mJ pulses at 1kHz using hollow-fiber pulse compression." In: *Optics letters* 35.11 (June 2010), pp. 1887–9. ISSN: 1539-4794. URL: http://www.ncbi.nlm.nih.gov/pubmed/20517451.

[48] J C Knight et al. "PURE SILICA SINGLE-MODE FIBRE WITH HEXAGONAL PHOTONIC CRYSTAL CLADDING". In: *Optical Fiber Communication Conference*. Optical Society of America, 1996, PD3. URL: http://www.opticsinfobase.org/abstract.cfm?URI=OFC-1996-PD3.

[49] Philip Russell. "Photonic Crystal Fibers". In: *Science* 299.5605 (2003), pp. 358–362. DOI: 10.1126/science.1079280. URL: http://www.sciencemag.org/content/299/5605/358.abstract.

[50] Jinendra K Ranka, Robert S Windeler, and Andrew J Stentz. "Efficient visible continuum generation in air-silica microstructure optical fibers with anomalous dispersion at 800 nm". In: *Lasers and Electro-Optics, 1999. CLEO'99. Summaries of Papers Presented at the Conference on*. IEEE. 1999, CPD8–1.

[51] Jinendra K Ranka, Robert S Windeler, and Andrew J Stentz. "Visible continuum generation in air-silica microstructure optical fibers with anomalous dispersion at 800 nm". In: *Opt. Lett.* 25.1 (Jan. 2000), pp. 25–27. DOI: 10.1364/OL.25.000025. URL: http://ol.osa.org/abstract.cfm?URI=ol-25-1-25.

[52] D. J. Jones. "Carrier-Envelope Phase Control of Femtosecond Mode-Locked Lasers and Direct Optical Frequency Synthesis". In: *Science* 288.5466 (Apr. 2000), pp. 635–639. ISSN: 00368075. DOI: 10.1126/science.288.5466.635. URL: http://www.sciencemag.org/cgi/doi/10.1126/science.288.5466.635.

[53] P St. J Russell et al. "Hollow-core photonic crystal fibres for gas-based nonlinear optics". In: *Nat Photon* 8.4 (Apr. 2014), pp. 278–286. ISSN: 1749-4885. URL: http://dx.doi.org/10.1038/nphoton.2013.31210.1038/nphoton.2013.312.

[54] M. Bradler, P. Baum, and E. Riedle. "Femtosecond continuum generation in bulk laser host materials with sub-μJ pump pulses". In: *Applied Physics B* 97.3 (Aug. 2009), pp. 561–574. ISSN: 0946-2171. DOI: 10.1007/s00340-009-3699-1. URL: http://www.springerlink.com/index/10.1007/s00340-009-3699-1.

[55] J Kasparian et al. "Infrared extension of the super continuum generated by femtosecond terawatt laser pulses propagating in the atmosphere." In: *Optics letters* 25.18 (Sept. 2000), pp. 1397–9. ISSN: 0146-9592. URL: http://www.ncbi.nlm.nih.gov/pubmed/18066229.

[56] P Kinsler. "Phase coherence and extreme self phase modulation". In: *ArXiv e-prints* (Aug. 2007). arXiv: 0708.4112 [physics.optics].

[57] D. Faccio et al. "Generation and control of extreme blueshifted continuum peaks in optical Kerr media". In: *Physical Review A* 78.3 (Sept. 2008), pp. 1–6. ISSN: 1050-2947. DOI: 10.1103/PhysRevA.78.033825. URL: http://link.aps.org/doi/10.1103/PhysRevA.78.033825.

[58] P Di Trapani et al. "Spontaneously Generated X-Shaped Light Bullets". In: *Phys. Rev. Lett.* 91.9 (Aug. 2003), p. 93904. DOI: 10.1103/PhysRevLett.91.093904. URL: http://link.aps.org/doi/10.1103/PhysRevLett.91.093904.

[59] Miguel A. Porras et al. "From X- to O-shaped spatiotemporal spectra of light filaments in water". In: *Optics Letters* 30.24 (Dec. 2005), p. 3398. ISSN: 0146-9592. DOI: 10.1364/OL.30.003398. URL: http://ol.osa.org/abstract.cfm?URI=ol-30-24-3398.

[60] M. Kolesik et al. "Physical Factors Limiting the Spectral Extent and Band Gap Dependence of Supercontinuum Generation". In: *Physical Review Letters* 91.4 (July 2003), pp. 4–7. ISSN: 0031-9007. DOI: 10.1103/PhysRevLett.91.043905. URL: http://link.aps.org/doi/10.1103/PhysRevLett.91.043905.

[61] Robert W Boyd. *Nonlinear optics*. Academic press, 2003.

[62] Couairon * A. et al. "Self-compression of ultra-short laser pulses down to one optical cycle by filamentation". In: *Journal of Modern Optics* 53.1-2 (2006), pp. 75–85. DOI: 10.1080/09500340500227760. URL: http://dx.doi.org/10.1080/09500340500227760.

[63] Andrius Baltuska et al. "Phase-controlled amplification of few-cycle laser pulses". In: *Selected Topics in Quantum Electronics, IEEE Journal of* 9.4 (2003), pp. 972–989.

[64] F Silva et al. "High-average-power, carrier-envelope phase-stable, few-cycle pulses at 2.1 μm from a collinear BiB< sub> 3</sub> O< sub> 6</sub> optical parametric amplifier". In: *Optics letters* 37.5 (2012), pp. 933–935.

[65] A Thai et al. "Sub-250-mrad, passively carrier–envelope-phase-stable mid-infrared OPCPA source at high repetition rate". In: *Opt. Lett.* 36.19 (Oct. 2011), pp. 3918–3920. DOI: 10.1364/OL.36.003918. URL: http://ol.osa.org/abstract.cfm?URI=ol-36-19-3918.

[66] Mitsuo Takeda, Hideki Ina, and Seiji Kobayashi. "Fourier-transform method of fringe-pattern analysis for computer-based topography and interferometry". In: *J. Opt. Soc. Am.* 72.1 (Jan. 1982), pp. 156–160. DOI: 10.1364/JOSA.72.000156. URL: http://www.opticsinfobase.org/abstract.cfm?URI=josa-72-1-156.

[67] M Kakehata et al. "Single-shot measurement of carrier-envelope phase changes by spectral interferometry." In: *Optics letters* 26.18 (Sept. 2001), pp. 1436–8. ISSN: 0146-9592. URL: http://www.ncbi.nlm.nih.gov/pubmed/18049630.

[68] Joshua E Rothenberg. "Pulse splitting during self-focusing in normally dispersive media". In: *Opt. Lett.* 17.8 (Apr. 1992), pp. 583–585. DOI: 10.1364/OL.17.000583. URL: http://ol.osa.org/abstract.cfm?URI=ol-17-8-583.

[69] A Couairon et al. "Practitioner's guide to laser pulse propagation models and simulation". In: *The European Physical Journal-Special Topics* 199.1 (2011), pp. 5–76.

[70] "E. D. Filer, C. A. Morrison, G. A. Turner, and N. P. Barnes, in Advanced Solid-State Lasers (Optical Society of America, 1990), pp. 354–370." In: ().

[71] Richard C Powell et al. "Index-of-refraction change in optically pumped solid-state laser materials". In: *Opt. Lett.* 14.21 (Nov. 1989), pp. 1204–1206. DOI: 10.1364/OL.14.001204. URL: http://ol.osa.org/abstract.cfm?URI=ol-14-21-1204.

[72] W F Krupke et al. "Spectroscopic, optical, and thermomechanical properties of neodymium- and chromium-doped gadolinium scandium gallium garnet". In: *J. Opt. Soc. Am. B* 3.1 (Jan. 1986), pp. 102–114. DOI: 10.1364/JOSAB.3.000102. URL: http://josab.osa.org/abstract.cfm?URI=josab-3-1-102.

[73] K D Moll and Alexander L Gaeta. "Role of dispersion in multiple-collapse dynamics." In: *Optics letters* 29.9 (May 2004), pp. 995–7. ISSN: 0146-9592. URL: http://www.ncbi.nlm.nih.gov/pubmed/15143652.

[74] a. Brodeur and S. Chin. "Band-Gap Dependence of the Ultrafast White-Light Continuum". In: *Physical Review Letters* 80.20 (May 1998), pp. 4406–4409. ISSN: 0031-9007. DOI: 10.1103/PhysRevLett.80.4406. URL: http://link.aps.org/doi/10.1103/PhysRevLett.80.4406.

[75] Michaël Hemmer et al. "Self-compression to sub-3-cycle duration of mid-infrared optical pulses in dielectrics". In: *Opt. Express* 21.23 (Nov. 2013), pp. 28095–28102. DOI: 10.1364/OE.21.028095. URL: http://www.opticsexpress.org/abstract.cfm?URI=oe-21-23-28095.

[76] V Pervak et al. "High-dispersive mirrors for femtosecond lasers". In: *Opt. Express* 16.14 (July 2008), pp. 10220–10233. DOI: 10.1364/OE.16.010220. URL: http://www.opticsexpress.org/abstract.cfm?URI=oe-16-14-10220.

[77] Bruno E Schmidt et al. "Frequency domain optical parametric amplification". In: *Nat Commun* 5 (May 2014). URL: http://dx.doi.org/10.1038/ncomms464310.1038/ncomms4643.

[78] D Herrmann et al. "Approaching the full octave: noncollinear optical parametric chirped pulse amplification with two-color pumping". In: *Optics Express* 18.18 (Aug. 2010), pp. 18752–18762. ISSN: 1094-4087. URL: http://www.opticsinfobase.org/abstract.cfm?URI=oe-18-18-18752.

[79] Thomas Brabec and Ferenc Krausz. "Intense few-cycle laser fields: Frontiers of nonlinear optics". In: *Reviews of Modern Physics* 72.2 (2000), p. 545.

[80] P F Moulton. "Spectroscopic and laser characteristics of Ti:Al2O3". In: *J. Opt. Soc. Am. B* 3.1 (Jan. 1986), pp. 125–133. DOI: 10.1364/JOSAB.3.000125. URL: http://josab.osa.org/abstract.cfm?URI=josab-3-1-125.

[81] Donna Strickland and Gerard Mourou. "Compression of amplified chirped optical pulses". In: *Optics communications* 55.6 (1985), pp. 447–449.

[82] C E Cook. "Pulse Compression-Key to More Efficient Radar Transmission". In: *Proceedings of the IRE* 48.3 (Mar. 1960), pp. 310–316. ISSN: 0096-8390. DOI: 10.1109/JRPROC.1960.287599.

[83] Scott A Diddams et al. "Direct Link between Microwave and Optical Frequencies with a 300 THz Femtosecond Laser Comb". In: *Phys. Rev. Lett.* 84.22 (May 2000), pp. 5102–5105. DOI: 10.1103/PhysRevLett.84.5102. URL: http://link.aps.org/doi/10.1103/PhysRevLett.84.5102.

[84] M Hentschel et al. "Attosecond metrology." In: *Nature* 414.6863 (Nov. 2001), pp. 509–13. ISSN: 0028-0836. DOI: 10.1038/35107000. URL: http://www.ncbi.nlm.nih.gov/pubmed/11734845.

[85] Peter Moulton and Evgeni Slobodchikov. "1-GW-Peak-Power, Cr:ZnSe Laser". In: *CLEO:2011 - Laser Applications to Photonic Applications*. Optical Society of America, 2011, PDPA10. DOI: 10.1364/CLEO_AT.2011.PDPA10. URL: http://www.opticsinfobase.org/abstract.cfm?URI=CLEO_AT-2011-PDPA10.

[86] Irina T Sorokina and Evgeni Sorokin. "Femtosecond Cr2+-based Lasers". In: *IEEE JOURNAL OF SELECTED TOPICS IN QUANTUM ELECTRONICS* VOL. 21.1 (2015).

[87] S A Akhmanov et al. "Observation of parametric amplification in the optical range". In: *Jetp Lett* 2 (1965), pp. 191–193.

[88] A Dubietis, G Jonušauskas, and A Piskarskas. "Powerful femtosecond pulse generation by chirped and stretched pulse parametric amplification in BBO crystal". In: *Optics Communications* 88.4 (1992), pp. 437–440.

[89] Jan Rothhardt et al. "Octave-spanning OPCPA system delivering CEP-stable few-cycle pulses and 22 W of average power at 1 MHz repetition rate". In: *Optics express* 20.10 (2012), pp. 10870–10878.

[90] A. Baltuška, T. Fuji, and T. Kobayashi. "Controlling the Carrier-Envelope Phase of Ultrashort Light Pulses with Optical Parametric Amplifiers". In: *Physical Review Letters* 88.13 (Mar. 2002), pp. 4–7. ISSN: 0031-9007. DOI: 10.1103/PhysRevLett.88.133901. URL: http://link.aps.org/doi/10.1103/PhysRevLett.88.133901.

[91] C. Vozzi et al. "Characterization of a high-energy self-phase-stabilized near-infrared parametric source". In: *Journal of the Optical Society of America B* 25.7 (May 2008), B112. ISSN: 0740-3224. DOI: 10.1364/JOSAB.25.00B112. URL: http://www.opticsinfobase.org/abstract.cfm?URI=josab-25-7-B112.

[92] C Vozzi et al. “Millijoule-level phase-stabilized few-optical-cycle infrared parametric source”. In: *Optics letters* 32.20 (2007), pp. 2957–2959.

[93] C Vozzi et al. “High-energy, few-optical-cycle pulses at 1.5 {Á}m with passive carrier-envelope phase stabilization”. In: *Optics express* 14.21 (2006), pp. 10109–10116.

[94] O D Mücke et al. “10-mJ optically synchronized CEP-stable chirped parametric amplifier at 1.5 μm”. In: *Optics and Spectroscopy* 108.3 (2010), pp. 456–462.

[95] O D Mücke et al. “Scalable Yb-MOPA-driven carrier-envelope phase-stable few-cycle parametric amplifier at 1.5 μm”. In: *Opt. Lett.* 34.2 (Jan. 2009), pp. 118–120. DOI: 10.1364/OL.34.000118. URL: http://ol.osa.org/abstract.cfm?URI=ol-34-2-118.

[96] Oliver D Mücke et al. “Self-compression of millijoule 1.5 μm pulses”. In: *Opt. Lett.* 34.16 (Aug. 2009), pp. 2498–2500. DOI: 10.1364/OL.34.002498. URL: http://ol.osa.org/abstract.cfm?URI=ol-34-16-2498.

[97] T Fuji et al. “Parametric amplification of few-cycle carrier-envelope phase-stable pulses at 2.1 microm.” In: *Optics letters* 31.8 (Apr. 2006), pp. 1103–5. ISSN: 0146-9592. URL: http://www.ncbi.nlm.nih.gov/pubmed/16625917.

[98] Xun Gu et al. “Generation of carrier-envelope-phase-stable 2- cycle 740- μ J pulses at 2 . 1- μ m carrier wavelength”. In: 17.1 (2009), pp. 2957–2959. URL: http://www.attoworld.de/Documents/papers/OpticsExpress/OptExpress17_p62_2009.pdf.

[99] J Moses et al. “Highly stable ultrabroadband mid-IR optical parametric chirped-pulse amplifier optimized for superfluorescence suppression.” In: *Optics letters* 34.11 (June 2009), pp. 1639–41. ISSN: 0146-9592. URL: http://www.ncbi.nlm.nih.gov/pubmed/19488133.

[100] Kyung-Han Hong et al. “Multi-mJ, kHz, 2.1 μm optical parametric chirped-pulse amplifier and high-flux soft x-ray high-harmonic generation”. In: *Opt. Lett.* 39.11 (June 2014), pp. 3145–3148. DOI: 10.1364/OL.39.003145. URL: http://ol.osa.org/abstract.cfm?URI=ol-39-11-3145.

[101] Olivier Chalus et al. “Mid-IR short-pulse OPCPA with micro-Joule energy at 100 kHz”. In: 17.5 (2009), pp. 3330–3332.

[102] M Hemmer et al. “18-\<i\>{\textmu}\</i\>J energy, 160-kHz repetition rate, 250-MW peak power mid-IR OPCPA”. In: *Chin. Opt. Lett.* 11.1 (Jan. 2013), p. 13202. URL: http://col.osa.org/abstract.cfm?URI=col-11-1-013202.

[103] *Clark-MXR, Inc.* URL: http://www.cmxr.com/.

[104] *Light Conversion Inc.* URL: http://www.lightcon.com/.

[105] Bruno E Schmidt et al. “CEP stable 1.6 cycle laser pulses at 1.8 μm.” In: *Optics express* 19.7 (Mar. 2011), pp. 6858–64. ISSN: 1094-4087. URL: http://www.ncbi.nlm.nih.gov/pubmed/21451713.

[106] Bruno E Schmidt et al. "Compression of 1.8 μm laser pulses to sub two optical cycles with bulk material". In: *Applied Physics Letters* 96.12 (2010), pp. –. DOI: http://dx.doi.org/10.1063/1.3359458. URL: http://scitation.aip.org/content/aip/journal/apl/96/12/10.1063/1.3359458.

[107] N Ishii et al. "Sub-two-cycle, carrier-envelope phase-stable, intense optical pulses at 1.6 μm from a BiB3O6optical parametric chirped-pulse amplifier". In: *Opt. Lett.* 37.20 (Oct. 2012), pp. 4182–4184. DOI: 10.1364/OL.37.004182. URL: http://ol.osa.org/abstract.cfm?URI=ol-37-20-4182.

[108] A Galvanauskas et al. "High-energy femtosecond pulse amlification in a quasi-phase-matched parametric amplifier". In: *Opt. Lett.* 23.3 (Feb. 1998), pp. 210–212. DOI: 10.1364/OL.23.000210. URL: http://ol.osa.org/abstract.cfm?URI=ol-23-3-210.

[109] Giulio Cerullo, Sandro De Silvestri, and Dipartimento Fisica. "Chapter XX: Ultrafast optical parametric amplifiers". In: ().

[110] V. Petrov et al. "Femtosecond nonlinear frequency conversion based on BiB3O6". In: *Laser & Photonics Reviews* 4.1 (Jan. 2010), pp. 53–98. ISSN: 18638880. DOI: 10.1002/lpor.200810075. URL: http://doi.wiley.com/10.1002/lpor.200810075.

[111] Masood Ghotbi et al. "Efficient 1 kHz femtosecond optical parametric amplification in BiB(3)O(6) pumped at 800 nm." In: *Optics express* 14.22 (Oct. 2006), pp. 10621–6. ISSN: 1094-4087. URL: http://www.ncbi.nlm.nih.gov/pubmed/19529465.

[112] V. Petrov et al. "High-power Femtosecond Optical Parametric Amplification at 1 kHz in BiB(3)O(6) pumped at 800 nm." In: *Optics express* 15.2 (Jan. 2007), pp. 556–63. ISSN: 1094-4087. URL: http://www.ncbi.nlm.nih.gov/pubmed/19532274.

[113] Ivaylo Nikolov et al. "near infrared using BiB 3 O 6 nonlinear crystals pumped at 800 nm". In: 32.22 (2007), pp. 3342–3344.

[114] T R Schibli et al. "Attosecond active synchronization of passively mode-locked lasers by balanced cross correlation". In: *Advanced Solid-State Photonics*. Optical Society of America. 2003, p. 108.

[115] T W Hansch and B Couillaud. "Laser frequency stabilization by polarization spectroscopy of a reflecting reference cavity". In: *Optics communications* 35.3 (1980), pp. 441–444.

[116] Hanieh Fattahi et al. "Efficient, octave-spanning difference-frequency generation using few-cycle pulses in simple collinear geometry". In: 38.20 (2013), pp. 4216–4219.

[117] G M Gale et al. “Sub-20-fs tunable pulses in the visible from an 82-MHz optical parametric oscillator”. In: *Opt. Lett.* 20.14 (July 1995), pp. 1562–1564. DOI: 10.1364/OL.20.001562. URL: http://ol.osa.org/abstract.cfm?URI=ol-20-14-1562.

[118] Giedrius Andriukaitis et al. “90 GW peak power few-cycle mid-infrared pulses from an optical parametric amplifier.” In: *Optics letters* 36.15 (Aug. 2011), pp. 2755–7. ISSN: 1539-4794. URL: http://www.ncbi.nlm.nih.gov/pubmed/21808302.

[119] H W Icenogle, Ben C Platt, and William L Wolfe. “Refractive indexes and temperature coefficients of germanium and silicon”. In: *Appl. Opt.* 15.10 (Oct. 1976), pp. 2348–2351. DOI: 10.1364/AO.15.002348. URL: http://ao.osa.org/abstract.cfm?URI=ao-15-10-2348.

[120] Berge Tatian. “Fitting refractive-index data with the Sellmeier dispersion formula”. In: *Appl. Opt.* 23.24 (Dec. 1984), pp. 4477–4485. DOI: 10.1364/AO.23.004477. URL: http://ao.osa.org/abstract.cfm?URI=ao-23-24-4477.

[121] Philip E Ciddor. “Refractive index of air: new equations for the visible and near infrared”. In: *Appl. Opt.* 35.9 (Mar. 1996), pp. 1566–1573. DOI: 10.1364/AO.35.001566. URL: http://ao.osa.org/abstract.cfm?URI=ao-35-9-1566.

[122] Nobuhiro Umemura, Kentaro Miyata, and Kiyoshi Kato. “New data on the optical properties of BiB3O6”. In: *Optical Materials* 30.4 (2007), pp. 532–534. ISSN: 0925-3467. DOI: http://dx.doi.org/10.1016/j.optmat.2006.12.014. URL: http://www.sciencedirect.com/science/article/pii/S0925346707000249.

[123] I H MALITSON. “Interspecimen Comparison of the Refractive Index of Fused Silica”. In: *J. Opt. Soc. Am.* 55.10 (Oct. 1965), pp. 1205–1208. DOI: 10.1364/JOSA.55.001205. URL: http://www.opticsinfobase.org/abstract.cfm?URI=josa-55-10-1205.

[124] M Joffre. “Linear techniques of phase measurement by femtosecond spectral interferometry for applications in spectroscopy”. In: 12.12 (1995), pp. 2467–2474.

[125] D J Kane and R Trebino. “Characterization of arbitrary femtosecond pulses using frequency-resolved optical gating”. In: *Quantum Electronics, IEEE Journal of* 29.2 (Feb. 1993), pp. 571–579. ISSN: 0018-9197. DOI: 10.1109/3.199311.

[126] P K Bates, O Chalus, and J Biegert. “Ultrashort pulse characterization in the mid-infrared”. In: *Opt. Lett.* 35.9 (May 2010), pp. 1377–1379. DOI: 10.1364/OL.35.001377. URL: http://ol.osa.org/abstract.cfm?URI=ol-35-9-1377.

[127] Selcuk Akturk et al. “The general theory of first-order spatio-temporal distortions of Gaussian pulses and beams”. In: *Opt. Express* 13.21 (Oct. 2005), pp. 8642–8661. DOI: 10.1364/OPEX.13.008642. URL: http://www.opticsexpress.org/abstract.cfm?URI=oe-13-21-8642.

[128] P Béjot et al. “Mechanism of hollow-core-fiber infrared-supercontinuum compression with bulk material”. In: *Phys. Rev. A* 81.6 (June 2010), p. 63828. DOI: 10.1103/PhysRevA.81.063828. URL: http://link.aps.org/doi/10.1103/PhysRevA.81.063828.

[129] Tenio Popmintchev et al. “Phase matching of high harmonic generation in the soft and hard X-ray regions of the spectrum.” In: *Proceedings of the National Academy of Sciences of the United States of America* 106.26 (June 2009), pp. 10516–21. ISSN: 1091-6490. DOI: 10.1073/pnas.0903748106. URL: http://www.pubmedcentral.nih.gov/articlerender.fcgi?artid=2698889\&tool=pmcentrez\&rendertype=abstract.

[130] *C-Laser, private communication.* URL: http://www.claser-sh.com/.

[131] S Miller et al. “Polarization-dependent nonlinear refractive index of BiB3O6”. In: *Optical Materials* 30.10 (2008), pp. 1469–1472. ISSN: 0925-3467. DOI: http://dx.doi.org/10.1016/j.optmat.2007.11.015. URL: http://www.sciencedirect.com/science/article/pii/S092534670700331X.

[132] Anne Harth et al. “Two-color pumped OPCPA system emitting spectra spanning 1.5 octaves from VIS to NIR”. In: *Opt. Express* 20.3 (Jan. 2012), pp. 3076–3081. DOI: 10.1364/OE.20.003076. URL: http://www.opticsexpress.org/abstract.cfm?URI=oe-20-3-3076.

[133] Pierre Tournois. “Acousto-optic programmable dispersive filter for adaptive compensation of group delay time dispersion in laser systems”. In: *Optics Communications* 140.4–6 (1997), pp. 245–249. ISSN: 0030-4018. DOI: http://dx.doi.org/10.1016/S0030-4018(97)00153-3. URL: http://www.sciencedirect.com/science/article/pii/S0030401897001533.

[134] Robert Szipöcs et al. “Chirped multilayer coatings for broadband dispersion control in femtosecond lasers”. In: *Opt. Lett.* 19.3 (Feb. 1994), pp. 201–203. DOI: 10.1364/OL.19.000201. URL: http://ol.osa.org/abstract.cfm?URI=ol-19-3-201.

[135] V Pervak et al. “Double-angle multilayer mirrors with smoothdispersion characteristics”. In: *Opt. Express* 17.10 (May 2009), pp. 7943–7951. DOI: 10.1364/OE.17.007943. URL: http://www.opticsexpress.org/abstract.cfm?URI=oe-17-10-7943.

[136] P. H. Bucksbaum. “The future of attosecond spectroscopy”. In: *Science* 317 (2007), pp. 766–769.

[137] A. H. Zewail. “Femtochemistry: Atomic-scale dynamics of the chemical bond”. In: *Journal of Physical Chemistry A* 104 (2000), pp. 5660–5694.

[138] Eleftherios Goulielmakis et al. “Real-time observation of valence electron motion.” In: *Nature* 466.7307 (Aug. 2010), pp. 739–43. ISSN: 1476-4687. DOI: 10.1038/nature09212. URL: http://www.ncbi.nlm.nih.gov/pubmed/20686571.

[139] S Adachi et al. "1.2 mJ sub-4-fs source at 1 kHz from an ionizing gas." In: *Optics letters* 35.7 (Apr. 2010), pp. 980–2. ISSN: 1539-4794. URL: http://www.ncbi.nlm.nih.gov/pubmed/20364190.

[140] C Manzoni et al. "Coherent synthesis of ultra-broadband optical parametric amplifiers." In: *Optics letters* 37.11 (June 2012), pp. 1880–2. ISSN: 1539-4794. URL: http://www.ncbi.nlm.nih.gov/pubmed/22660060.

[141] Tobias Witting, Felix Frank, and CA Arrell. "Characterization of high-intensity sub-4-fs laser pulses using spatially encoded spectral shearing interferometry". In: *Optics ...* 36.9 (2011), pp. 1680–1682. URL: http://www.opticsinfobase.org/abstract.cfm?URI=ol-36-9-1680.

[142] E Goulielmakis, M Schultze, and M Hofstetter. "Single-cycle nonlinear optics". In: *Science* 320.June (2008), pp. 1614–1617. URL: http://www.sciencemag.org/content/320/5883/1614.short.

[143] Miguel Miranda et al. "Simultaneous compression and characterization of ultrashort laser pulses using chirped mirrors and glass wedges". In: 20.1 (2012), pp. 688–697. URL: http://arxiv.org/abs/1110.2964.

[144] A. Baltuska. "Second-harmonic generation frequency-resolved optical gating in the single-cycle regime". In: *IEEE Journal of Quantum Electronics* 35 (1999), pp. 459–478.

[145] Benjamín Alonso et al. "Spatiotemporal characterization of few-cycle laser pulses." In: *Optics express* 20.16 (July 2012), pp. 17880–93. ISSN: 1094-4087. URL: http://www.ncbi.nlm.nih.gov/pubmed/23038338.

[146] Miguel Miranda et al. "Characterization of broadband few-cycle laser pulses with the d-scan technique". In: 20.17 (2012), pp. 673–677.

[147] Benjamín Alonso et al. "Characterization of sub-two-cycle pulses from a hollow-core fiber compressor in the spatiotemporal and spatiospectral domains". In: *Applied Physics B* 112.1 (Mar. 2013), pp. 105–114. ISSN: 0946-2171. DOI: 10.1007/s00340-013-5406-5. URL: http://link.springer.com/10.1007/s00340-013-5406-5.

[148] V Pervak et al. "Double-angle multilayer mirrors with smooth dispersion characteristics." In: *Optics express* 17.10 (May 2009), pp. 7943–51. ISSN: 1094-4087. URL: http://www.ncbi.nlm.nih.gov/pubmed/19434126.

[149] Akira Suda and Takanori Takeda. "Effects of Nonlinear Chirp on the Self-Phase Modulation of Ultrashort Optical Pulses". In: *Applied Sciences* 2.4 (June 2012), pp. 549–557. ISSN: 2076-3417. DOI: 10.3390/app2020549. URL: http://www.mdpi.com/2076-3417/2/2/549/.

[150] Yves Coello et al. “Group-velocity dispersion measurements of water, seawater, and ocular components using multiphoton intrapulse interference phase scan”. In: *Applied optics* (2007). URL: http://www.opticsinfobase.org/abstract.cfm?id=148222http://www.opticsinfobase.org/abstract.cfm?uri=ao-46-35-8394.

[151] I J Sola et al. “Controlling attosecond electron dynamics by phase-stabilized polarization gating”. In: *Nature Physics* 2.5 (2006), pp. 319–322.

[152] F Ferrari et al. “High-energy isolated attosecond pulses generated by above-saturation few-cycle fields”. In: *Nature Photonics* 4.12 (2010), pp. 875–879.

[153] Ming-Chang Chen et al. “Generation of bright isolated attosecond soft X-ray pulses driven by multicycle midinfrared lasers”. In: *Proc Natl Acad Sci U S A* 111.23 (June 2014), E2361–7. DOI: 10.1073/pnas.1407421111.

[154] H Vincenti and F Quéré. “Attosecond Lighthouses: How To Use Spatiotemporally Coupled Light Fields To Generate Isolated Attosecond Pulses”. In: *Phys. Rev. Lett.* 108.11 (Mar. 2012), p. 113904. DOI: 10.1103/PhysRevLett.108.113904. URL: http://link.aps.org/doi/10.1103/PhysRevLett.108.113904.

[155] Kyung Taec Kim et al. “Photonic streaking of attosecond pulse trains”. In: *Nature Photonics* 7.8 (2013), pp. 651–656.

[156] Bing Shan and Zenghu Chang. “Dramatic extension of the high-order harmonic cutoff by using a long-wavelength driving field”. In: *Physical Review A* 65.1 (2001), p. 11804.

[157] Ch Spielmann et al. “Generation of coherent X-rays in the water window using 5-femtosecond laser pulses”. In: *Science* 278.5338 (1997), pp. 661–664.

[158] Nobuhisa Ishii et al. “Generation of soft x-ray and water window harmonics using a few-cycle, phase-locked, optical parametric chirped-pulse amplifier”. In: *Opt. Lett.* 37.1 (Jan. 2012), pp. 97–99. DOI: 10.1364/OL.37.000097. URL: http://ol.osa.org/abstract.cfm?URI=ol-37-1-97.

[159] A Shiner et al. “Wavelength Scaling of High Harmonic Generation Efficiency”. In: *Phys. Rev. Lett.* 103.7 (Aug. 2009), p. 73902. DOI: 10.1103/PhysRevLett.103.073902. URL: http://link.aps.org/doi/10.1103/PhysRevLett.103.073902.

[160] Dane R Austin and Jens Biegert. “Strong-field approximation for the wavelength scaling of high-harmonic generation”. In: *Phys. Rev. A* 86.2 (Aug. 2012), p. 23813. DOI: 10.1103/PhysRevA.86.023813. URL: http://link.aps.org/doi/10.1103/PhysRevA.86.023813.

[161] J Tate et al. “Scaling of Wave-Packet Dynamics in an Intense Midinfrared Field”. In: *Phys. Rev. Lett.* 98.1 (Jan. 2007), p. 13901. DOI: 10.1103/PhysRevLett.98.013901. URL: http://link.aps.org/doi/10.1103/PhysRevLett.98.013901.

[162] M V Frolov et al. "Analytic Description of the High-Energy Plateau in Harmonic Generation by Atoms: Can the Harmonic Power Increase with Increasing Laser Wavelengths?" In: *Phys. Rev. Lett.* 102.24 (June 2009), p. 243901. DOI: 10.1103/PhysRevLett.102.243901. URL: http://link.aps.org/doi/10.1103/PhysRevLett.102.243901.

[163] M.-C. Chen et al. "Bright, Coherent, Ultrafast Soft X-Ray Harmonics Spanning the Water Window from a Tabletop Light Source". In: *Phys. Rev. Lett.* 105.17 (Oct. 2010), p. 173901. DOI: 10.1103/PhysRevLett.105.173901. URL: http://link.aps.org/doi/10.1103/PhysRevLett.105.173901.

[164] Nobuhisa Ishii et al. "Carrier-envelope phase-dependent high harmonic generation in the water window using few-cycle infrared pulses". In: *Nat Commun* 5 (2014), p. 3331. DOI: 10.1038/ncomms4331.

[165] C A Haworth et al. "Half-cycle cutoffs in harmonic spectra and robust carrier-envelope phase retrieval". In: *Nat Phys* 3.1 (2007), pp. 52–57. URL: http://dx.doi.org/10.1038/nphys463.

[166] Giuseppe Sansone et al. "Isolated single-cycle attosecond pulses". In: *Science* 314.5798 (2006), pp. 443–446.

[167] Michael Hofstetter et al. "Attosecond dispersion control by extreme ultraviolet multilayer mirrors". In: *Opt. Express* 19.3 (Jan. 2011), pp. 1767–1776. DOI: 10.1364/OE.19.001767. URL: http://www.opticsexpress.org/abstract.cfm?URI=oe-19-3-1767.

[168] Alexander Guggenmos et al. "Aperiodic CrSc multilayer mirrors for attosecond water window pulses". In: *Opt. Express* 21.19 (Sept. 2013), pp. 21728–21740. DOI: 10.1364/OE.21.021728. URL: http://www.opticsexpress.org/abstract.cfm?URI=oe-21-19-21728.

[169] Michael Geissler et al. "Light propagation in field-ionizing media: extreme nonlinear optics". In: *Physical review letters* 83.15 (1999), p. 2930.

[170] Maxim V Ammosov, Nikolai B Delone, and Vladimir P Krainov. "Tunnel ionization of complex atoms and atomic ions in electromagnetic field". In: *1986 Quebec Symposium*. International Society for Optics and Photonics. 1986, pp. 138–141.

[171] Misha Yu Ivanov, Thomas Brabec, and Neal Burnett. "Coulomb corrections and polarization effects in high-intensity high-harmonic emission". In: *Physical Review A* 54.1 (1996), p. 742.

[172] Ariel Gordon and Franz X Kärtner. "Quantitative modeling of single atom high harmonic generation". In: *Physical review letters* 95.22 (2005), p. 223901.

[173] X M Tong and C D Lin. "Empirical formula for static field ionization rates of atoms and molecules by lasers in the barrier-suppression regime". In: *Journal of Physics B: Atomic, Molecular and Optical Physics* 38.15 (2005), p. 2593.

[174] Anh-Thu Le et al. "Quantitative rescattering theory for high-order harmonic generation from molecules". In: *Physical Review A* 80.1 (2009), p. 13401.

[175] Philippe Balcou et al. “Generalized phase-matching conditions for high harmonics: The role of field-gradient forces”. In: *Phys. Rev. A* 55.4 (Apr. 1997), pp. 3204–3210. DOI: 10.1103/PhysRevA.55.3204. URL: http://link.aps.org/doi/10.1103/PhysRevA.55.3204.

Acknowledgements

First, I would like to thank my advisors for giving me this opportunity, support and help during this thesis. This work was full of great challenges, delays and problems, but I feel that we came out successful in the end. So thanks Jens and Helder for making this possible, and for setting ambitious goals for this thesis.

The post-docs I've worked with deserve a big thanks - first and foremost Phillip K. Bates, from which I learnt countless things as I was starting my PhD. Not only has he taught me much of what I know about OPAs, but he is also an excellent teacher for pretty much everything else. I'm sorry Phil that you had to endure all my stupid questions. Great help came also from Dane R. Austin, one of the most competent people I have had the pleasure to work with and learn from. From the physics discussions to the Matlab wizardry, he was an inspiration to learn from. Big thanks also to Olivier Chalus for the help and for lifting everyone's mood around him. Thanks Judith Dura for all the help and instruction, and thanks Michael Hemmer for all the nice chats about lasers and the best ways to build them (I have never met anyone so enthusiastic about this).

A special thanks to my colleague Miguel Miranda for all the help and being a friend, but also for having invented the d-scan technique, which made part of my thesis so much easier. I would still probably be scratching my head if not for this. Another special thanks to my colleagues Stephan Teichmann and Seth Cousin for all the effort and patience during the last part of our theses where we mostly worked on the same project (that tiny 1.5 year 'sprint'). It really took the 3 of us working around the clock, testing hypothesis after hypothesis, fixing problem after problem to make it happen - and I'm really glad we managed to make it work! Looking back it was actually a greater victory than we took it for at the time. Many thanks to my colleagues Alexandre Thai and Matthias Baudisch, which worked hard with me (and even without me) during the supercontinuum 'sprint'. They, along with Dane and many others were instrumental for the supercontinuum work to happen.

I would also like to thank all my other colleagues at AUO in Barcelona and FemtoLab in Porto for making my day-to-day life better. So in no special order thanks Alex Grün, Benjamin Wolter, Michael Pullen, Michele Schlafani, Barbara Sabater, Daniel Peacham, Noslen Suarez, Alexander Britz, Claus Lidner, Svën Kunzel, Kostas & Steffen, Miguel Canhota, Ana Silva, Cledson Santana Lopes, Benjamin Alonso and Warein Holgado.

I would also like to thank all my friends at ICFO and IFIMUP for the support and

fun times we have had over the years - you made all the difference. Much of this thesis had not been possible without the people not directly involved in it.

Um enorme obrigado goes to my family, for always being there for me, helping me in good and bad times and for giving me support. And don't worry, the lasers I work with are totally safe and harmless!

Last but not the least, thanks to Jana, for all her love and support during these years!

Publications

Articles

1. **F. Silva**, D. R. Austin, A. Thai, M. Baudisch, M. Hemmer, D. Faccio, A. Couairon, and J. Biegert, *Multi-octave supercontinuum generation from mid-infrared filamentation in a bulk crystal*, Nat. Commun., vol. 3, p. 807, 2012.

   Highlighted in Nature Photonics: O. Graydon, *Supercontinua: Broader than ever*, Nat. Phot., vol. 6, no. 7, p. 413, Jul. 2012.

2. **F. Silva**, S. Teichmann, S. L. Cousin, M. Hemmer, and J. Biegert, *Spatio-temporal isolation of attosecond soft X-ray pulses in the water window*, Nat. Commun., 6:6611, Mar. 2015

3. **F. Silva**, P. K. Bates, A. Esteban-Martin, M. Ebrahim-Zadeh, and J. Biegert, *High-average-power, carrier-envelope phase-stable, few-cycle pulses at 2.1 μm from a collinear BiB_3O_6 optical parametric amplifier*, Opt. Lett., vol. 37, no. 5, pp. 933-935, 2012.

4. **F. Silva**, M. Miranda, B. Alonso, J. Rauschenberger, V. Pervak, and H. Crespo, *Simultaneous compression, characterization and phase stabilization of GW-level 1.4 cycle VIS-NIR femtosecond pulses using a single dispersion-scan setup*, Opt. Express, vol. 22, no. 9, pp. 10181-10191, 2014.

5. S. M. Teichmann, **F. Silva**, S. L Cousin, and J. Biegert, *Importance of Intensity-to-Phase Coupling for Water-Window High-Order-Harmonic Generation with Few-Cycle Pulses*, Phys. Rev. A 91 (6). APS: 63817.

6. B. Alonso, M. Miranda, **F. Silva**, V. Pervak, J. Rauschenberger, J. San Roman, I. J. Sola, and H. Crespo, *Characterization of sub-two-cycle pulses from a hollow-core fiber compressor in the spatiotemporal and spatiospectral domains*, Appl. Phys. B, vol. 112, no. 1, pp. 105-114, Mar. 2013.

7. S. L. Cousin, **F. Silva**, S. Teichmann, M. Hemmer, B. Buades, and J. Biegert, *High-flux table-top soft x-ray source driven by sub-2-cycle, CEP stable, 1.85-μm 1-kHz pulses for carbon K-edge spectroscopy*, Opt. Lett., vol. 39, no. 18, pp. 5383-5386, 2014.

8. M. Miranda, C. L. Arnold, T. Fordell, **F. Silva**, R. Weigand, A. L. Huillier, and H. Crespo, *Characterization of broadband few-cycle laser pulses with the d-scan technique*, vol. 20, no. 17, pp. 673-677, 2012.

9. A. Ricci, **F. Silva**, A. Jullien, S. L. Cousin, D. R. Austin, J. Biegert, and R. Lopez-Martens, *Generation of high-fidelity few-cycle pulses at 2.1 μm via cross-polarized wave generation*, Opt. Express, vol. 21, no. 8, pp. 9711-9721, Apr. 2013.

Conference Contributions

1. **F. Silva**, P. K. Bates, J. Biegert, A. Esteban-Martin, M. Ebrahim-Zadeh, A. Gruen, and S. L. Cousin, *Few-cycle CEP-stable source at 2.1 μm based on collinear OPA in BiB_3O_6*, in CLEO:2011 - Laser Applications to Photonic Applications, 2011, p. QTuF7.

2. **F. Silva**, D. R. Austin, A. Couairon, P. K. Bates, and J. Biegert, *3-octave high-energy supercontinuum from visible to mid-IR*, in CLEO:2011 - Laser Applications to Photonic Applications, 2011, p. CThBB3.

3. **F. Silva**, P. K. Bates, A. Esteban-Martin, M. Ebrahim-Zadeh, A. Gruen, S. Cousin, and J. Biegert, *Scalable collinear BiB_3O_6 OPA for few-cycle CEP stable pulses at 2.1 μm*, in CLEO/Europe and EQEC 2011 Conference Digest, 2011, p. EF36.

4. **F. Silva**, D. R. Austin, A. Couairon, P. K. Bates, and J. Biegert, *3-octave high-energy supercontinuum from a 2 μm source*, in Lasers and Electro-Optics Europe (CLEO EUROPE/EQEC), 2011 Conference on and 12th European Quantum Electronics Conference, 2011, p. 1.

5. **F. Silva**, P. K. Bates, A. Esteban-Martin, M. Ebrahim-Zadeh, and J. Biegert, *High Average-power, Self-CEP Stable few-cycle Pulses at 2.1 μm through Collinear OPA in BiB_3O_6*, in Research in Optical Sciences, 2012, p. HT1C.6.

6. **F. Silva**, M. Miranda, B. Alonso, J. Rauschenberger, P. Vladimir, and H. Crespo, *Simultaneous compression, measurement and phase stabilization of >50 GW, 3.2 fs pulses using a single dispersion-scan setup*, in Ultrafast Optics 2013.

7. **F. Silva**, M. Miranda, and H. Crespo, *Broadband third-harmonic generation in multilayer graphene and its application to pulse measurement by THG dispersion-scan*, in Ultrafast Optics 2013.

8. **F. Silva**, M. Miranda, S. M. Teichmann, M. Baudisch, M. Massicotte, F. Koppens, J. Biegert, and H. Crespo, *Pulse measurement from near to mid-IR using third harmonic generation dispersion scan in multilayer graphene*, in Lasers and Electro-Optics Europe (CLEO EUROPE/IQEC), 2013 Conference on and International Quantum Electronics Conference, 2013, p. 1.

9. **F. Silva**, M. Miranda, S. M. Teichmann, M. Baudish, M. Massicotte, F. Koppens, J. Biegert, and H. Crespo, *Near to mid-IR ultra-broadband third harmonic generation in multilayer graphene: few-cycle pulse measurement using THG dispersion-scan*, in CLEO: Science and Innovations, 2013, p. CW1H-5.

10. **F. Silva**, M. Miranda, and H. Crespo, *Measuring few-cycle laser pulses: A comparative study between dispersion-scan and FROG*, in Lasers and Electro-Optics Europe (CLEO EUROPE/IQEC), 2013 Conference on and International Quantum Electronics Conference, 2013, p. 1.

11. **F. Silva**, S. M. Teichmann, S. L. Cousin, M. Hemmer, and J. Biegert, *Half-cycle Cutoffs up to the Oxygen K-edge: Signatures of Isolated Attosecond Pulses Across the Water Window*, in CLEO: QELS Fundamental Science, 2014, p. FTu3B-4.

12. **F. Silva**, M. Miranda, and H. Crespo, *Broadband deep-ultraviolet third-harmonic generation in multilayer graphene and its application to few-cycle pulse measurement by THG d-scan*, in Graphene 2014.

13. S. M. Teichmann, **F. Silva**, S. L. Cousin, and J. Biegert, *Signatures of isolated attosecond pulses spanning the water window in high harmonic half-cycle cutoffs*, in Research in Optical Sciences, 2014, p. HW3C.8.

14. M. Hemmer, A. Thai, M. Baudisch, **F. Silva**, D. R. Austin, H. Ishizuki, T. Taira, A. Couairon, D. Faccio, and J. Biegert, *High Average Power Few-cycle Pulses in the Mid-IR, Self-compression and Continuum Generation*, in CLEO: 2013, 2013, p. CM2L.3.

15. M. Miranda, P. Rudawski, C. Guo, **F. Silva**, C. L. Arnold, T. Binhammer, H. Crespo, and A. L'Huillier, *Ultrashort laser pulse characterization from dispersion scans: a comparison with SPIDER*, Cleo 2013, p. JTh2A.31, 2013.

16. H. Crespo, **F. Silva**, and R. Weigand, *Broadband deep-ultraviolet femtosecond pulse generation by third-order nonlinear optical processes in thin media*, in Lasers and Electro-Optics Europe (CLEO EUROPE/IQEC), 2013 Conference on and International Quantum Electronics Conference, 2013, p. 1.

17. Dane R. Austin, **F. Silva**, A. Thai, M. Baudisch, M. Hemmer, D. Faccio, A. Couairon, and J. Biegert, *Multi-octave supercontinuum generation from mid-infrared filamentation in a bulk crystal*, EPJ Web Conf., vol. 41, p. 10010, 2013.

18. A. Ricci, **F. Silva**, A. Jullien, S. Cousin, N. Forget, D. Austin, J. Biegert, and R. Lopez-Martens, *Generation of high-fidelity few-cycle pulses at 2 μm via XPW*, in Conference on Lasers and Electro-Optics 2012, 2012, p. CM1B.8.

19. M. Baudisch, **F. Silva**, D. Austin, A. Thai, M. Hemmer, A. Couairon, and J. Biegert, *Multi-octave supercontinuum from bulk filamentation of a mid-IR pulse*, in Conference on Lasers and Electro-Optics 2012, 2012, p. QM4E.7.

20. R. L.-M. A. Ricci, **F. Silva**, A. Jullien, S. Cousin, N. Forget, D. Austin, J. Biegert, *XPW Generation of high-fidelity few-cycle pulses at 2 μm*, in Int. Conference on Ultra-High Intensity Lasers, 2012.

21. B. Alonso, M. Miranda, **F. Silva**, V. Pervak, J. Rauschenberger, J. S. Roman, I. J. Sola, and H. Crespo, *Characterization of sub-two-cycle pulses from a hollow-core fiber compressor in the spatiotemporal and spatio-spectral domains*, in 2013 Conference on Lasers and Electro-Optics - International Quantum Electronics Conference, 2013, p. CFIE32.

22. M. Baudisch, **F. Silva**, D. Austin, A. Thai, M. Hemmer, A. Couairon, J. Biegert, *High-energy, 3.3-octave spanning supercontinuum in bulk driven at mid-IR*, in Deutsche Physikalische Gesellschaft Fruhjahrstagung, 2012.